國 立 交 通 大 學

電信工程研究所

博 士 論 文

調頻連續波感測器射頻前端設計與系統整合驗證

Frequency-Modulated Continuous-Wave Sensor Design and System Integration

研 究 生：張 繼 禾　　(Chi-Ho Chang)

指導教授：莊晴光博士 (Dr. Ching-Kuang C. Tzuang)

中華民國九十八年九月

調頻連續波感測器射頻前端設計與系統整合驗證

Frequency-Modulated Continuous-Wave Sensor Design and System Integration

研 究 生：張繼禾　　　Student：Chi-Ho Chang

指導教授：莊晴光 博士 Advisor：Dr. Ching-Kuang C. Tzuang

國 立 交 通 大 學
電 信 工 程 研 究 所
博 士 論 文

A Dissertation
Submitted to Institute of Communication Engineering
College of Electrical and Computer Engineering
National Chiao Tung University
in Partial Fulfillment of the Requirements
for the Degree of Doctor of Philosophy
in
Communication Engineering
Hsinchu, Taiwan

中 華 民 國 九 十 八 年 九 月

推　薦　函

一、　事由：貴校電信研究所博士班研究生　張繼禾　提出論文以參加國立交

通大學博士班論文口試。

二、　說明：貴校電信研究所博士班研究生　張繼禾　已完成本校電信研究所

規定之學科課程及論文研究之訓練。

有關學科部分，張君已修滿十八學分之規定（請查閱學籍資料）並通

過資格考試。

有關論文部分，張君已完成其論文初稿，相關之論文亦分別發表或即

將發表於國際期刊（請查閱附件）並滿足論文計點之要求。

總而言之，張君已具備國立交通大學電信研究所應有之教育及訓練水

準，因此特推薦

張君參加國立交通大學電信工程學系博士班論文口試。

臺灣大學電信工程所教授　　莊　晴　光

調頻連續波感測器射頻前端設計與系統整合驗證

研究生：張繼禾　　　　　　　　　　　指導教授：莊晴光 博士

國立交通大學 電信工程研究所 博士班

摘　　要

本文主要介紹以 CMOS 技術設計且用於交通運輸管理的 X 頻段調頻連續波（FMCW）偵測器系統。文內所提的偵測器系統採用兩組天線分別進行訊號的發射和接收。而且這完整的射頻（RF）收發器實現了應用標準的 0.18 微米一層聚合物六層金屬(1P6M)互補金屬氧化物半導體（CMOS）技術來完成且其晶片面積大小僅 1.68×1.6 毫米平方。

在這篇論文中，以所謂合成近橫向電磁模之互補傳導線帶的傳輸線（CCS TL）用於整個射頻晶片的設計。的主要特點是互補傳導線帶的傳輸線(CCS TL)可減少 CMOS 射頻收發機晶片中相鄰兩元件間的電磁耦合，此結構亦能夠將各種射頻信號處理元件稠密的整合到單一晶片上。因此互補傳導線帶的傳輸線(CCS TL) 在 10.5GHz 工作頻率中提供了晶片上從接收路徑傳輸路徑 55.0 dB 隔離度。

此外這兩個平面洩漏波陣列天線的增益設計在 18dB。實驗結果顯示兩陣列天線間的隔離度在間距為 5.0 毫米與工作頻率為 10.5 GHz 時高於 42.0

dB。這平面天線實現了 $csc^2\theta$ 型式天線場型和也可在短距離偵測中輔助中頻濾波器作為靈敏度時間控制（STC）功能。此調頻連續波傳感器的雛型系統是應用於多車道的距離測量之交通管理系統（TMS）。

本文最佳貢獻整合 0.18 微米互補金屬氧化物半導體(CMOS)收發器和陣列天線成為調頻連續波之射頻前端。另一個創新的工作，使用了平面洩漏波陣列天線形成 $csc^2\theta$ 型式的天線輻射場型，然後配合三角波產生電路，中頻放大器，數位信號處理器，以及一些電子儀表來證明近似均一訊號雜音比的概念。最終由測量結果得知，實地測試結果與系統模擬是一致的。

未來本論文最重要的工作，即是將現有雷達系統微型化，即是將原有的射頻系統、中頻類比電路與數位訊號處理電路等皆以 CMOS 積體電路的技術進行縮裝與整合，即整合 RFIC、AIC 與 DIC 等積體電路成為系統晶片。

Frequency-Modulated Continuous-Wave Sensor Design and System Integration

Student：**Chi-Ho Chang**　　　　Advisor：**Dr. Ching-Kuang C. Tzuang**

Institute of Communication Engineering

National Chiao Tung University

ABSTRACT

The paper presents an X-band CMOS-based frequency-modulation continuous-wave (FMCW) sensor system for the transportation management. The proposed sensor system adopts two antennas to transmit and receive signal separately. The completed radio frequency (RF) transceiver is realized by using standard 0.18 μm one-poly six-metal (1P6M) complementary metal–oxide semiconductor (CMOS) technology with a chip area of 1.68 mm × 1.6 mm.

The so-called synthetic quasi-TEM complementary conducting-strip transmission line (CCS-TL) is also employed throughout the entire RF chip design. The main features of the CCS TL are the reduction of electromagnetic coupling of adjacent components in the RF CMOS transceiver chip and it able to densely integrate various RF signal-processing components into a single chip. Therefore, the CCS TL provides the on-chip isolation of 55.0dB from the receiving path to the transmitting path at 10.5GHz.

Additionally, two planar leaky-mode antenna arrays with a gain of 18 dB are designed. Experiments indicate the isolation between two antenna arrays with a spacing of 5.0 mm is higher than 42.0 dB at 10.5 GHz. The planar antenna was achieved the csc^2 type antenna pattern and also took as the

sensitivity time control (STC) function of IF filter for short range detection. The prototype of the FMCW sensor system is applied to the range measurement of multiple lanes for the Transportation Management System (TMS).

The best contribution of the paper is integrated a 0.18 um CMOS transceiver and antenna arrays into a FMCW RF-frond. Another originality of the work that used the planar leaky-wave antenna array to shape a $csc^2\theta$-type radiation pattern, then assisted a triangular-wave circuit, an IF amplifier, a digital signal processor, and lot of instruments to prove the nearly uniform SNR concept. Finally, the measured results from field tests agree well with the system simulation results.

The future work of the dissertation is miniaturized of the radar system. The works use the CMOS integrated circuit technology to miniaturize and integrate the original radio frequency system, intermediate frequency analog circuits and the digital signal processing circuit and so on. They namely of the system on chip (SOC) for the radar system is integrated by radio frequency integrated circuits (RFIC), analog integrated circuits (AIC), and digital integrated circuits (DIC).

誌　　　　謝

　　我來自於國防部中山科學研究院，從事於小型都卜勒及調頻連續波感測器的設計應用，雖然在大學與碩士階段都是主修控制工程，但因所在職位工作需求的關鍵技術與亟需突破的研發瓶頸，皆在於射頻微波的設計與電子電路的縮裝等兩項學門。

　　因此在這篇誌謝詞的開始，首先要感謝我的學位指導教授莊晴光博士與師母楊靜蘭女士給我一個機會來學習微波這個課程，並在博三的下學期有機會協助莊老師參與交通部運輸研究所的微波偵測器研發專案，將所研究的論文與中科院的工作相結合。

　　因為這篇論文即是說明此計畫第一期的研發歷程與結果，其包含天線設計、CMOS 收發機內各元件設計與整合、中頻電路與數位訊號處理器研發、微波偵測器機構設計與全系統整合、FMCW 微波偵測器全系統靜態與動態測試驗證。

　　在此感謝臺灣大學電信所的同學—安錫與孟儒在天線設計上的協助，王紳、思賢、啟洋、致嘉與昆宏在 CMOS 收發機內各元件設計上的貢獻，順子與瑞琦在 CMOS 收發機的整合與晶片量測的協助。也感謝中科院的長官招嘉成主任、余嗣英副主任、杜德雲組長及林煥堯組長給予我這個機會到交大學習新知，尤其是林煥堯博士將我帶入微波設計與系統整合的工作

環境。更感謝中科院的同仁—楊培基博士、梁恩齊先生、邱榮閔先生與王睿深先生在數位訊號處理器研發與全系統整合驗證上的盡心幫忙，向心如先生與林祺琅先生在天線機構上設計協助，梁恩齊先生、許順峰先生與江鴻地先生在微波偵測器全系統動態驗證上的支援與協助。

其中最感念的是鄭慶學長，雖然他已過世，但是他在我這三年最失落的時間內，不斷給我的鼓勵與安慰，使我不致於放棄這學習的希望。最後要向我的家人說抱歉，因為選擇此論文題目涵蓋較廣，需回應審查者的問題較多，導致審查次數較多且審查時間較長，使自己無法陪同家人們在這段時間盡情遊玩與開心談天，因此要深深感謝我的家人。

TABLE OF CONTENTS

LIST OF FIGURES

LIST OF TABLES

CHAPTER 1

Introduction

1.1 History of the RF frond-end development of FMCW sensor

Radar is a system that uses electromagnetic waves to determine the range, altitude, direction, or speed of both moving and fixed objects such as aircraft, ships, motor vehicles, weather formations, and ground. The term *RADAR* was created the first initials in 1941 as an acronym for **Ra**dio **D**etection **a**nd **R**anging. The term has since entered the English language as a standard word, *radar*, misplacing the capitalization. Radar was originally called RDF (Radio Direction Finder) in the United Kingdom [1].

The history of radar began in the 1900s when engineers designed reflection devices. Around the 1930s, radar stations were being utilized. When radar was in its earliest stages of development, it is generally accepted that radar systems fell into two basic categories. Thus, operational radar was either a continuous wave (CW) system that had inherently been very good velocity (Doppler shift) measuring capability, or a pulsed radar system that had good range measuring and resolution capability [2]. Doppler radars may be coherent pulsed, continuous wave, or frequency modulated. A CW doppler radar is a special case that only supplies a velocity output. Early doppler radars were CW, and it quickly led to the development of Frequency-modulated continuous wave (FMCW) radar, which sweeps the transmitter frequency to determine the range. FMCW radar was highly developed for the time of World War II for the use by US Navy aircraft. Antenna designs for the CW and FMCW started out as separate transmit and receive antennas before the advent of low-cost microwave designs. In the

late 1960s traffic radars began being produced, which used a single antenna. This was constructed possible using circular polarization, and a multi-port waveguide section operating at X band. The late 1970s, this changed to linear polarization and the use of ferrite circulators at both X and K bands.

The microwave FMCW technique is better than other approaches such as infrared, ultrasound, video image and so on, because of its ease of implementation, inexpensiveness, wide range of applications, long-distance detection, and relative resilience against environmental effects. It applied the infrared technique or the video image processing to detecting the vehicles, the quality of measurement is easily degraded by the rain, the fog, the snow, the storm and so on. The ultrasound technique is usually used in the parking distance control, such as reversing radar. If it takes the inductive loops and magnetometer technique to detect vehicles, then the road excavation will be carried out and follow-up maintenance is not easy to do.

1.2 Development of the RF frond-end for FMCW sensor

Interest in frequency-modulation continuous-wave (FMCW) sensor has steadily risen in recent decades for diverse applications in commercial and consumer electronics. Such applications include automotive radar at 77GHz [3]-[10], liquid tank altimeters at 9.5–10GHz, 5.8GHz, and 24 GHz [11]-[12], global maritime distress and safety systems at 9.2–9.5GHz [13] and, most recently, the Transportation Management System (TMS) to monitor instantaneous main road vehicle transportation at the X-band [14]. The two most popular methods for making FMCW sensor transceivers at microwaves and millimeter-waves are hybrid microwave integrated circuit (MIC) [6], [15] and the GaAs monolithic microwave integrated circuit (MMIC) chipset [3], [5],

[9],[10],[16], [17], [18], [19], according to studies on FMCW radio frequency (RF) front-end designs.

The study reports, to the best of the authors' knowledge, the first X-Band TMS CMOS sensor with a uniformly distributed SNR (signal-to-noise ratio) for monitoring multiple-lane traffic. The RF signal processing at the front end has the following two features: 1) a CMOS multifunction chip to process most RF signals, and 2) a leaky-mode array to shape a csc^2 type antenna radiation pattern [20]-[22], thus establishing uniform SNR across the illuminated zone covering multiple lanes. Restated, the structure builds an equivalent sensitivity time control (STC) [23]-[27] that adds attenuation in the receiver as a function of time, to reduce the near-field interferences in the receiving path and to equalize the amplitude of echoes independent of range.

Base on traffic application apply the circuit/system simulation software Agilent[TM] ADS (advance design system) to construct the building block of the FMCW radar system was shown in Fig. 1. And it presents the block diagram of the complete integrated X-band radar with dual planar antenna arrays at the transmitter output and the receiver input, a fully integrated monolithic transceiver that has all building blocks that are required in RF signal processing, and a baseband digital signal processing unit for simultaneously measuring the range of a moving vehicle for the fast evaluation of radar performance.

The future works will use the CMOS integrated circuit technology to miniaturize and integrate above radio frequency circuits, analog circuits and digital circuit and so on. The next generation of the radar system integrates with radio frequency integrated circuits, analog integrated circuits, and digital integrated circuits into a single chip, and it is the so-call system on chip (SOC).
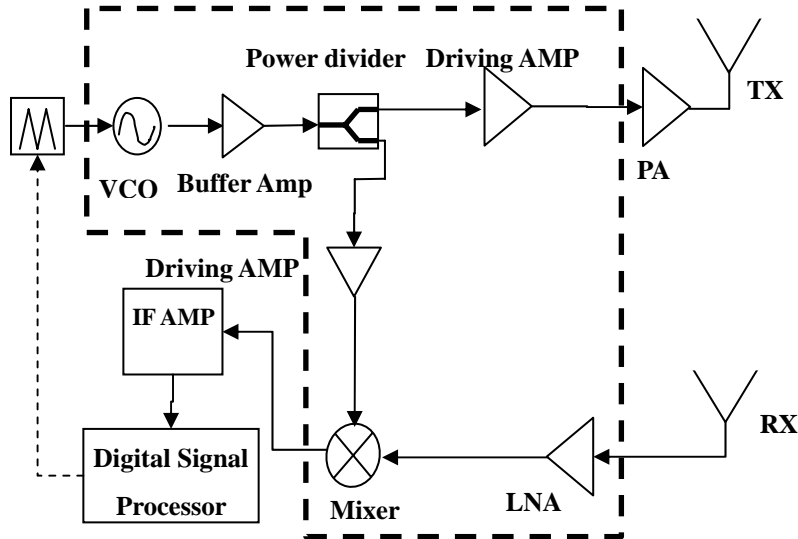
Fig.1.1 Block diagram of the proposed X-band FMCW sensor system, comprising two external antenna arrays, a single-chip CMOS transceiver (enclosed by the dashed line) and an external digital signal processing unit and necessary electronics. A power amplifier (PA) is added to increase the output power level.

Figure 1.1 shows the building blocks of the X-band FMCW sensor, which are as follows: dual planar antenna arrays at the transmitter output and the receiver input; a 0.18μm 1P6M CMOS fully integrated monolithic transceiver, which performs most of the required RF signal processing as shown inside the dashed lines, and a baseband digital signal processing unit for instantaneous and simultaneous assessment of range measurements. It is worth noting that using two antennas rather than only one eliminates the circulator, which is generally expensive and does not provide sufficient isolation between the transmitter and the receiver.

The rest of the paper is organized as follows. Chapter 2 summarizes the principles of range measurement based on the FMCW sensor. Chapter 3 introduces the CMOS implementations for X-band FMCW transceiver, and then the print circuit board (PCB) integration of leaky-mode antenna arrays is

reported in chapter 4. The accessory circuits include that the external IF circuit and digital signal processing unit are also illustrated in chapter 5. Chapter 6 describes the field tests of range measurement for detecting vehicle occupancy in multiple lanes after the signal-to-noise ratio (SNR) of the proposed sensor system is theoretically and experimentally confirmed. Conclusions are finally drawn in chapter 7.
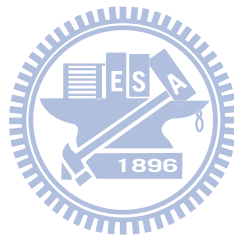
CHAPTER 2

Principles and Theories

There are three major theoretical foundations in the thesis; it is such three items as the principle of frequency-modulated continuous wave, the introduction of radar equation and the concept of the cosecant-squared antenna, respectively. These theoretical foundations not only construct the system block of all paper but also provide a basis for the measurements.

2.1 Principle of the frequency-modulated continuous wave

There are two ways of target detection in the radar; first, measurement of the distance or height of targets, the second is the speed measurement of the target (relative speed). The two ways have its theory and application, the chapter will present the way to measure target of the radar from the superficial to the deep.

Basic concept of range measurement of radar can prove by Fig.2.1. The R represents the distance of measurement, T_p is the round-trip time, c show the speed of light (close to 3.0×10^8 m/s). The value of R can be derived by equation (2-1).

$$R = \frac{c \times T_p}{2} \tag{2-1}$$

It is a basic principle of all radar that the measured distance was determined by the round-trip time of the light wave from the radar to the target, but its key point was a produced technology of the narrow-pulse and high-energy source.
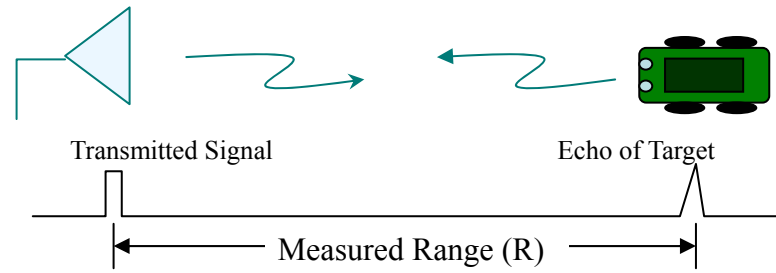
Fig. 2.1 System block of range measurement by the radar.

The moving-target speed measurement of the radar system was calculated by the Doppler frequency shift. The relative speed of the moving-target in the free space was shown by Fig. 2.1; the first step must analyze the included angles of the Cartesian coordinate system, and then the relative speed was transferred to the Doppler frequency in order to measure velocity. The formula of the Doppler frequency shift is revealed in (2-2),

$$f_d \approx 2 \times f_T \frac{v}{c} \times \cos(\gamma) = 2 \times f_T \frac{v}{c} \times \cos(\gamma_V) \times \cos(\gamma_H) \qquad (2\text{-}2)$$

v is the relative speed of the target, γ represent the angle of three-dimensional space between the target's forward velocity and the line of sight from the target to the radar, f_d depict the Doppler frequency, and f_T present the carrier frequency by the transmitter of the radar system.
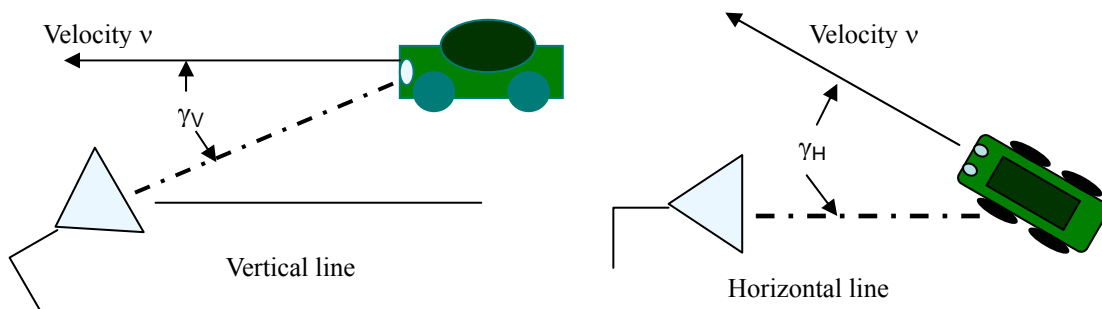
Fig. 2.2 System block of speed measurement by the radar

7

There are difference applications of radar between the frequency-modulated continuous wave (FMCW) system and the continuous wave (CW) system. It makes a brief explanation with the continuous wave system first, by Fig. 2.3 notice of invitation continuous wave system frequently can make speed measurement only, but can't do range measurement.
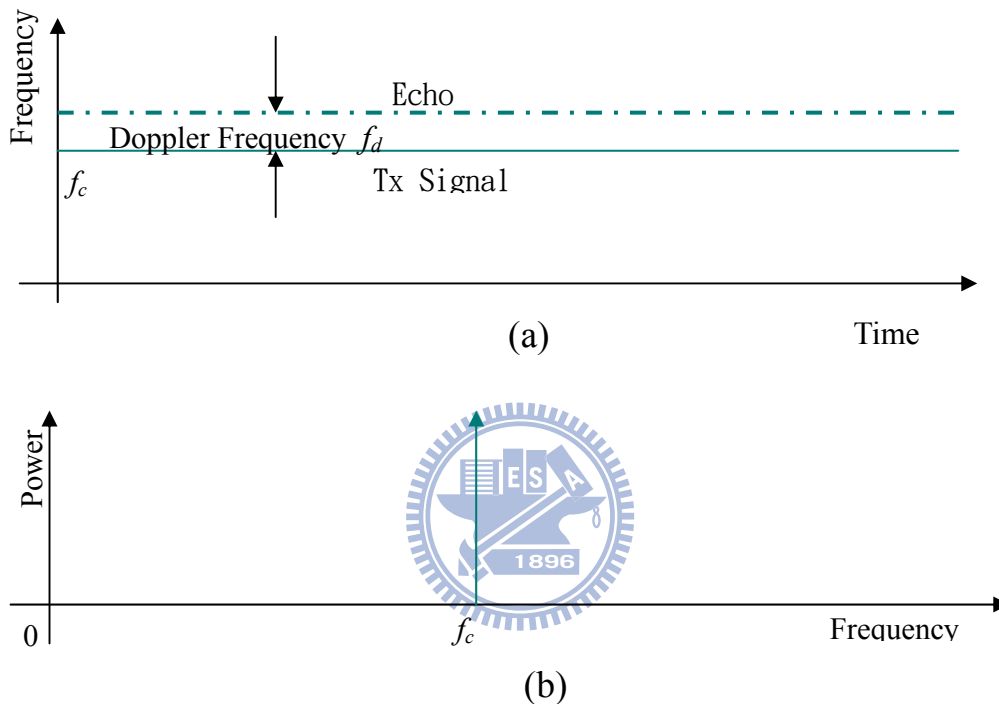
Fig.2.3 (a) The time response and (b) the spectrum of continuous wave system

Secondly, the range measurement was calculated by the beat frequency of the modulated-frequency continuous wave, and at the same time can estimate the relative speed by the Doppler frequency. However, the signal source of frequency-modulated continuous wave is a linear function such as the triangular wave or saw-tooth wave. We make the signal source of the frequency-modulated continuous wave with the sine wave, and then Fig. 2.4 illustrate the beat frequency is not unique. If the response of time domain transfers to the frequency domain, then the spectrum of the beat frequency is spread too widely

resulted in the target signal is hard to solve.

The linear frequency-modulated continuous wave is chosen that can calculate accurate range information, however, can solve the accurate range information, namely its beat frequency is very even and unique and its spectrum displays a very clear unique frequency. The function of the frequency versus time of the frequency-modulated continuous wave can be displayed by Fig. 2.5. The linear frequency- modulated continuous wave (FMCW) system is defined by physics meaning from Fig. 2.5. It can verify the correct information of the range measurement, but the formula and lemma must be proving the linearity at mathematics theory. And then prove the linear relation with the beat frequency f_b and the measured range R, can be directly derived by [28] as next page.
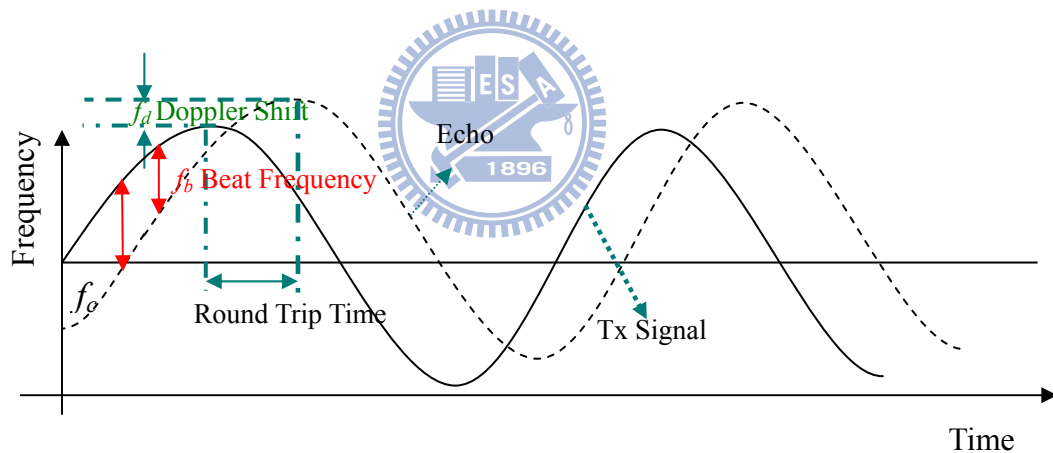
Fig.2.4 The frequency against the time plot of FMCW with the sine wave
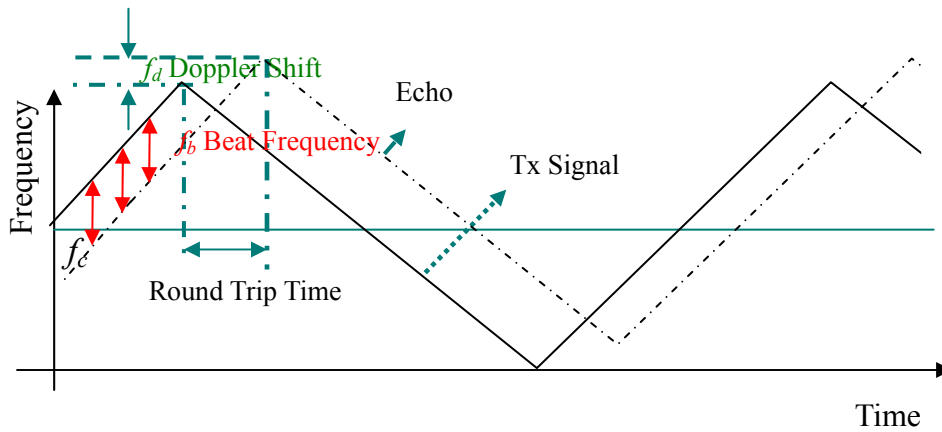
Fig.2.5 The frequency against time plot of FMCW with the linear function wave

Why adopt it to the linear-modulated FMCW (LFMCW) radar that measuring the distance and speed of target? Because the traditional cosine-wave modulated system, intermediate frequency (IF) of the demodulation signal is nonlinear relative with the distance from radar to target, so it must prove the IF of demodulation signal is linear relative with the distance in LFMCW.

In most active sensors, the frequency is modulated in a linear manner with time:

$$f(t) = A_b t$$

Substituting into the standard equation for FM, we obtain the following result:

$$v_{fm}(t) = A_c \cos[w_{c1} t + A_b \int_{-\infty}^{t} t \, dt] = A_c \cos[w_{c1} + \frac{A_b}{2} t^2]$$

The transmit signal will be shifted from that of the received signal because of the round trip time τ.
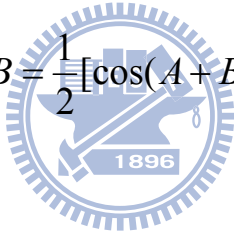
$$v_{fm}(t-\tau) = A_c \cdot \cos[w_{c2}(t-\tau) + \frac{A_b}{2}(t-\tau)^2]\,.$$

In the LFMCW system, the frequency is varying with time and can get beat frequency: $w_b = w_{c2}-w_{c1}$.

And a portion of the transmitted signal is mixed with the returned echo, and calculating the product:

$$v_{if} = v_{fm}(t-\tau) \cdot v_{fm}(t)$$
$$= A_c^2 \cos[w_{c1}t + \frac{A_b}{2}t^2] \cdot \cos[w_{c2}(t-\tau) + \frac{A_b}{2}(t-\tau)^2]$$

Equating using the trigonometric identities for the product of two sines, since

$$\cos A \cos B = \frac{1}{2}[\cos(A+B) + \cos(A-B)]$$

and $w_b = w_{c2}-w_{c1}$, we get

$$v_{if}(t) = \frac{1}{2}[\cos\{(w_{c1} + w_{c2} - A_b\tau)t + A_b t^2 + (\frac{A_b}{2}\tau^2 - w_{c2}\tau)\}$$
$$+ \cos\{(-w_b + A_b\tau)t + (w_{c2}\tau - \frac{A_b}{2}\tau^2)\}]$$

The first cos term describes a linearly increasing FM signal (chirp) at about twice the carrier frequency, this term is generally filtered out, and the second cos term describes a beat signal at a fixed frequency. $(w_b = 2\pi f_b)$

$$f_{if} = f_b = \frac{A_b}{2\pi}\tau, \quad (Let\ v_{if}'(t) = 0,\ to\ derive\ w_b\ ) \qquad (2\text{-}3)$$

By (2-3) the signal frequency (beat frequency) is directly proportional to the

delay time τ, and hence is directly proportional to the round trip time to the target.

We apply triangle-wave modulated signal to the linear FMCW system, base on the previous formula of linear FMCW and the delay time proportional to the beat frequency, use the point-slope form of basic mathematical to simplify the formula of linear FMCW (See Fig.2.6).
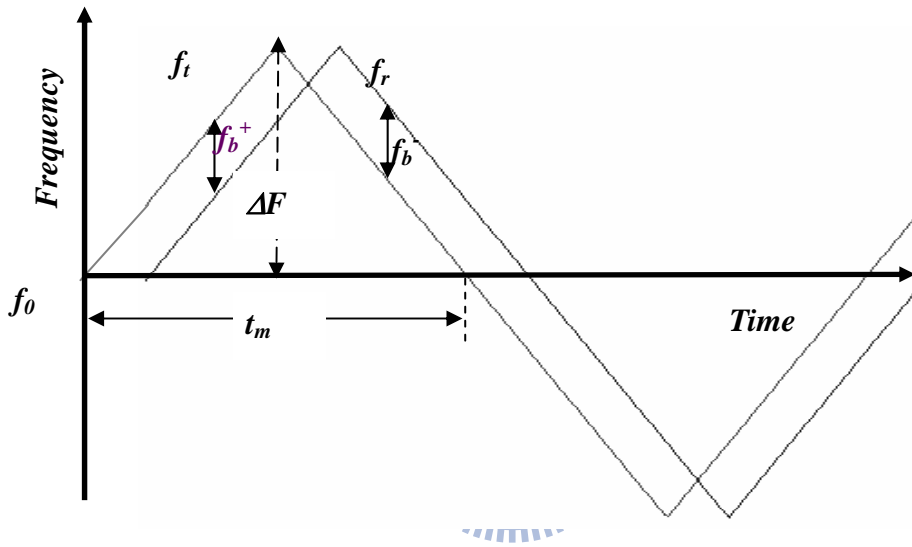
Fig.2.6 Range measurement graphic of the linear frequency modulation system

All parameters of Fig. 2.6 are defined as follows: f_t is the signal of the transmitter, f_r is the signal of the receiver, t_m present the periodic of signal, f_0 represent the initial frequency (offset frequency). f_b is the frequency difference (beat frequency), f_b^+ is the beat frequency of the up sweep modulation, f_b^- is the beat frequency of the down sweep modulation. f_d reveal the Doppler frequency, f_c illustrate the carrier frequency, ΔF shows the bandwidth of the system, R represents the range of measurement, C is the velocity of light. We base on the above plot of FMCW formula, the formula derivation is separated into a stationary target and moving target cases. When the target is stationary: $(f_d = 0)$ and we get

$$f_t = f_0 + \frac{2 \times \Delta F \times t}{t_m}, \quad f_r = f_0 + \frac{2 \times \Delta F \times (t - 2 \times \frac{R}{C})}{t_m},$$

the delay time τ of the receiver signal is $2 \times R/C$, then we can derive the beat frequency f_b, that is

$$f_b = f_t - f_r = \frac{4 \times \Delta F \times R}{t_m \times C}, \quad f_b^+ = f_b^- = f_b,$$

Finally, it transfers the beat frequency to the distance, we get

$$R = \frac{C \times t_m \times f_b}{4 \times \Delta F} = \frac{C \times f_b}{4 \times \Delta F \times f_m}, \quad f_m = \frac{1}{t_m} \qquad (2\text{-}4)$$

When the target is moving: $(f_d \neq 0)$, we also get

$$f_t = f_0 + \frac{2 \times \Delta F \times t}{t_m}, \quad f_r = f_0 + f_d \pm \frac{2 \times \Delta F \times (t - 2 \times \frac{R}{C})}{t_m},$$

The Doppler shift of moving target is carried in the receiver signal in this case. The direction of target relative to the FMCW radar may be opposite or followed, then we note that the sign of the delay term with "±" operator. Next, we derive the beat frequency f_b^+(up sweep modulation) is

$$f_b^+ = f_t - f_r = \frac{4 \times \Delta F \times R}{t_m \times C} - f_d,$$

and also derive the beat frequency f_b^-(down sweep modulation) is

$$f_b^- = f_r - f_t = \frac{4 \times \Delta F \times R}{t_m \times C} + f_d,$$

$$f_b^+ + f_b^- = \frac{8 \times \Delta F \times R}{t_m \times C},$$

Next, it transfers the beat frequency to the distance, we get

$$R = \frac{C \times t_m \times (f_b^+ + f_b^-)}{8 \times \Delta F} = \frac{C \times (f_b^+ + f_b^-)}{8 \times \Delta F \times f_m}, \quad f_m = \frac{1}{t_m} \qquad (2\text{-}5)$$

Finally, we use the fundamental theory of the Doppler frequency shift to derive the velocity of the moving target. That is

$$f_d = f_b^- - f_b^+ = \frac{2 \times v \times \cos\theta \times f_c}{C},$$

and

$$v = \frac{(f_b^- - f_b^+) \times C}{2 \times f_c \times \cos\theta} \qquad (2\text{-}6)$$

Moreover, by following the derivations documented in chapter 12.4 of [29], the ideal range resolution of the FMCW sensor can be estimated as follows.

$$R_0 = \frac{C}{2 \cdot \Delta F} \qquad (2\text{-}7)$$

Equations (2-4), (2-5) and (2-7) show the principles of FMCW sensors for range measurements. Furthermore, the signals in the transmitting and receiving paths are assumed to be independent of each other in the sensor. These derivations do not consider the coupling effects between the transmitting and receiving paths. However, such leakages could significantly reduce the

sensitivity of the FMCW sensor [29].

Equation (2-3) is represented by $R_0 = \dfrac{c}{2 \cdot \Delta F}$. If the range resolution (R_0) of the system is set to 1 meter, then RF bandwidth (*BW*) of 150MHz is derived by Eq. (2-3). On the other hand, the *BW* is changed from 150MHz to 50MHz, and then R_0 is converted from 1 meter to 3 meters. An example of from physics is considered to illustrate. Consider two vehicles of width 1 m, separated by a gap of 1m. When R_0 is 3 m, the FMCW system cannot easily distinguish one vehicle from another, and will often identify two vehicles as a large vehicle. When R_0 is 1 m, the FMCW system can easily distinguish one vehicle from another. Hence the bandwidth of the modulated signals is wider, and the range resolution is better.
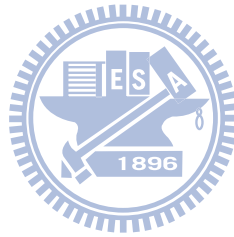
2.2 Introduction of the radar equation

The basic relation between the characteristics of the radar, target, and the received signal is known as the radar equation [30]. The geometry of scattering from an isolated radar target is displayed in the Fig. 2.7, with the parameters involved in the radar equation.
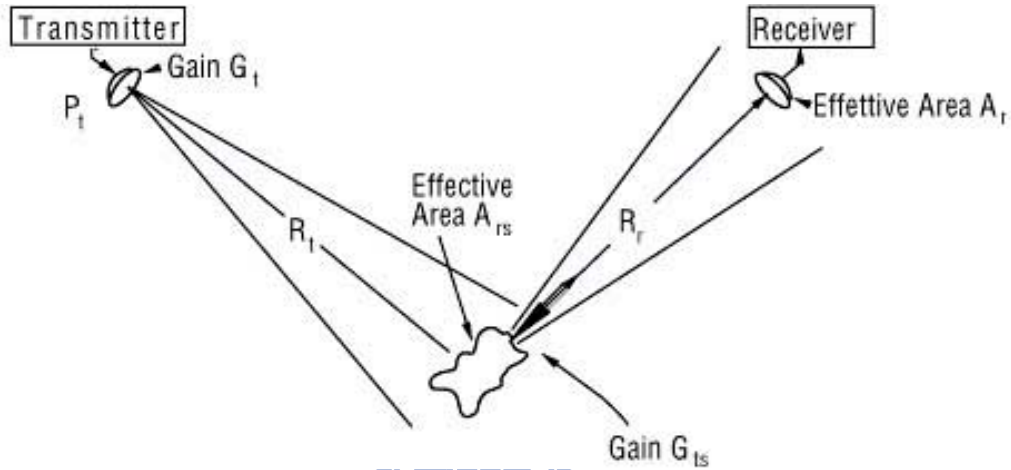
Fig.2.7 The radar detection block from transmitter to receiver

When a power P_t is transmitted by an antenna with gain G_t, the power per unit solid angle in the direction of the scatter is $P_t G_t$, where the value of G_t in that direction is used. At the scatter,

$$S_s = (P_t G_t)(\frac{1}{4\pi R^2})$$ (2-8)

where S_s is the power density at the scatter. The spreading loss $1/(4\pi R^2)$ is the reduction in power density associated with spreading of the power over a sphere of radius R surrounding the antenna. To obtain the total power intercepted by the scatter, the power density must be multiplied by the effective receiving area of the scatter.

$$P_{rs} = S_s A_{rs}$$ (2-9)

Note that the effective area of A_{rs} than the actual size of the scattering of incident light intercepted, but the effective area, that is, it is in the region all the powers of the incident light will be removed if it was assumed that all the remaining power of the beam through the continuing intermittent.

The actual value of A_{rs} depends on the effectiveness of the scatter as a receiving antenna. Some of the power received by the scatter is absorbed in losses in the scatter, unless it is a perfect conductor or a perfect isolator; the rest is reradiated in various directions. The fraction absorbed is f_a, so the fraction reradiated is $1 - f_a$, and the total reradiated power is

$$P_{ts} = P_{rs}(1 - f_a) \qquad (2\text{-}10)$$

The conduction and displacement currents that flow in the scatter result in radiation that has a pattern. Note that the effective receiving area of the scatter is a function of its orientation relative to the incoming beam, so that A_{rs} in the equation above is understood to apply only for the direction of the incoming beam. The radiation pattern may not be the same as the pattern of A_{rs}, and the gain in the direction of the receiver is the relevant value in the radiation pattern. Thus,

$$S_t = P_{ts} G_{ts} \frac{1}{4\pi R_t^2} \qquad (2\text{-}11)$$

where P_{ts} is the total reradiated power, G_{ts} is the gain of the scatter in the direction of the receiver, and $1/(4\pi R_t^2)$ is the spreading factor for the radiation. Note that a major difference between a communication link and radar scattering is that the communication link has only one spreading factor, whereas the radar has two. Thus, if $R_r = R_t$, the total distance is $2R_t$; for a communication link with

this distance, the spreading factor is only:

$$1/4(\frac{1}{4\pi R_t^2})$$

whereas for the radar it is $(\frac{1}{4\pi})^2(\frac{1}{R_t})^4$

Hence, the spreading loss for radar is much greater than for a communication link with the same total path length. The power entering the receiver is

$$P = SA \qquad (2\text{-}12)$$

where the area A_r is the effective aperture of the receiving antenna, not its actual area. Not only is this a function of direction, but it is also a function of the load impedance the receiver provides to the antenna; for example, P_r would have to be zero if the load were a short circuit or an open circuit.

The factors in (2-8) through (2-12) may be combined to obtain

$$P_r = (P_t G_t)\left(\frac{1}{4\pi R_t^2}\right)A_{rs}(1-f_a)G_{ts}\left(\frac{1}{4\pi R_t^2}\right)A_r$$

$$P_r = \left(\frac{P_t G_t A_r}{(4\pi)^2 R_t^2 R_r^2}\right)[A_{rs}(1-f_a)G_{ts}] \qquad (2\text{-}13)$$
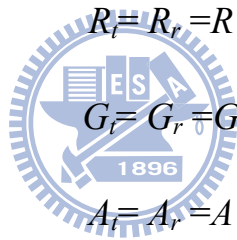
The factors associated with the scatter are combined in the square brackets. These factors are difficult to measure individually, and their relative contributions are uninteresting to one wishing to know the size of the received radar signal. Hence they are normally combined into one factor, the radar scattering cross section:

$$\sigma = A_{rs}(1-f_a)G_{ts} \qquad (2\text{-}14)$$

The cross-section s is a function of the directions of the incident wave and the wave toward the receiver, as well as that of the scatter shape and dielectric properties. The final form of the radar equation is obtained by rewriting (2-13) using the definition of (2-14):

$$P_r = \frac{P_t G_t A_r \sigma}{(4\pi)^2 R_t^2 R_r^2}$$

(2-15)

The most common situation is that for which receiving and transmitting locations are the same, so that the transmitter and receiver distances are the same. Almost as common is the use of the same antenna for transmitting and receiving, so the gains and effective apertures are the same, that is:

$$R_t = R_r = R$$
$$G_t = G_r = G$$
$$A_t = A_r = A$$

Since the effective area of an antenna is related to its gain by:

$$A = \frac{\lambda^2 G}{4\pi}$$

(2-16)

We may rewrite the radar equation (2-15) as

$$P_r = \frac{P_t G^2 \lambda^2 \sigma}{(4\pi)^3 R^4} = \frac{P_t A^2 \sigma}{4\pi \lambda^2 R^4}$$

(2-17)

where two forms are given, one in terms of the antenna gain and the other in terms of the antenna area. Equations (2-15) and (2-17) are general forms for both point and area targets. That is, the scattering cross-section s is not defined

in terms of any characteristic of a target type, but rather is the scattering cross-section of a particular target. The form given in (2-17) is for the so-called monostatic radar, and that in (2-15) is for bistatic radar, although it also applies for monostatic radar when the conditions for R, G, A given above are satisfied.

In the paper present that the power of the electromagnetic waves that propagate between the sensor and the single vehicle is estimated from the radar equation (2-17). And then the radar equation will be applied to the SNR measurement, the measured result can prove that the structure of the presented FMCW sensor has good performance for TMS.
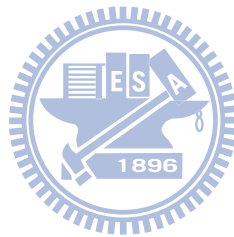
2.3. Concept of the cosecant-squared antenna

An important property of the cosecant-squared (csc^2) antenna is that the target power received from a target at constant altitude, h, remains independent of target range [28]. The cosecant-squared (csc^2) antenna pattern of the traditional airborne radar extends the beam coverage of fan-beam antenna where the appended coverage is desired, as shown Fig. 2.8.
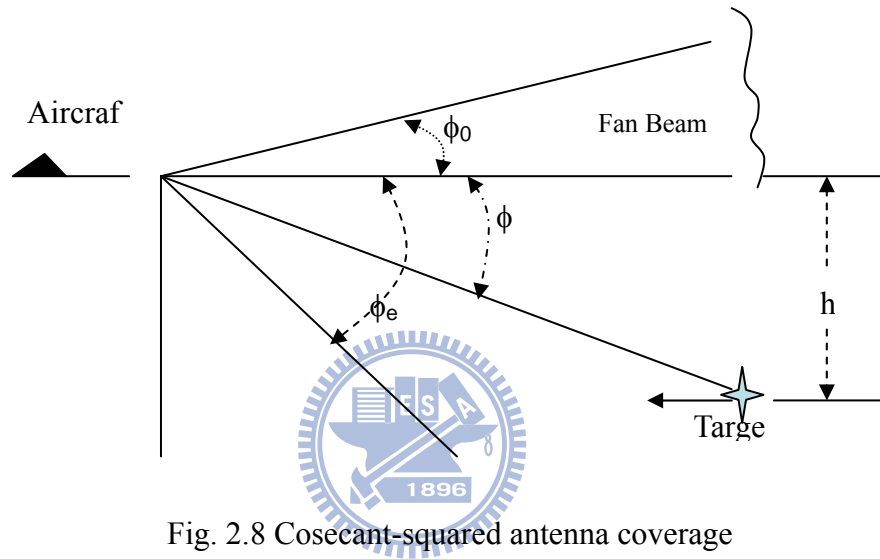
Fig. 2.8 Cosecant-squared antenna coverage

The extended coverage is required up to the vertical line passing through the antenna was presented by [28]. In the past, this is impossible with a single antenna to realize csc^2 pattern. The csc^2 pattern may be generated by a distorted parabolic antenna dish or by proper location of multiple feed horns in a true parabolic antenna.

The gain pattern of a cosecant-squared antenna is given by

$$G(\phi) = G(\phi_0) \frac{csc^2 \phi}{csc^2 \phi_0} \quad \phi_0 < \phi < \phi_1 \qquad (2-18)$$

where $G(\phi)$ is the gain at angle ϕ, ϕ_0, and ϕ_1 are the limits of the cosecant-squared beam. In the previous section, the radar equation was derived

and signal-to-noise ratio is given by

$$\frac{S}{N} = \frac{P_{TX} G_T G_R \lambda^2 \sigma}{(4\pi)^3 R^4 F k T B_n L} = (\frac{R_0}{R})^4 \qquad (2\text{-}19)$$

the terms of this equation, which depend on the transmitted power P_{TX}, the gains of transmitted antenna G_T and received antenna G_R, wavelength of carrier frequency λ, radar cross section factor σ, distance between radar and target R, noise figure F, the Boltzmann's constant k (1.38×10^{-23}), noise bandwidth B_n (Hz), the Kelvin temperature T, and system loss L.

Let G_T is equal to G_R, Using (2-18) and (2-19) and designating the collection of constant terms by K,

$$(\frac{S}{N})_r = K \frac{\csc^4 \phi}{R^4} \qquad (2\text{-}20)$$

where the subscript r refers to target return signal-to-noise ratio. From Fig. 2.8, since $\sin\phi = h/R$, we get $\csc\phi = R/h$ where R is the range of the target from the radar. Upon substitution in (2-20)

$$(\frac{S}{N})_r = \frac{K_1}{h^4}, \ K_1 \text{ is constant value} \qquad (2\text{-}21)$$

which remains constant for constant altitude targets.

Ultimately, the characteristics of the presented antenna array with a $\csc^2\theta$ pattern can compensate for the space loss of $1/R^4$ that can perform suitably the range measurement of multiple-lane for TMS application.

2.4. System Simulation of FMCW Radar

Then, the previous theoretical result is used and all parameters in the simulation environment (Fig. 2.9) defined. The Advanced Design System (ADS2006) Agilent[TM] is used to perform the simulation and the behavior model is adopted to construct the FMCW radar system. The behavior models of all the blocks of the above system structure were obtained using each circuit parameter and measurements made in individual IC probe tests. Therefore, the real circuits were not cascaded to the system block and the behavior models applied to construct.
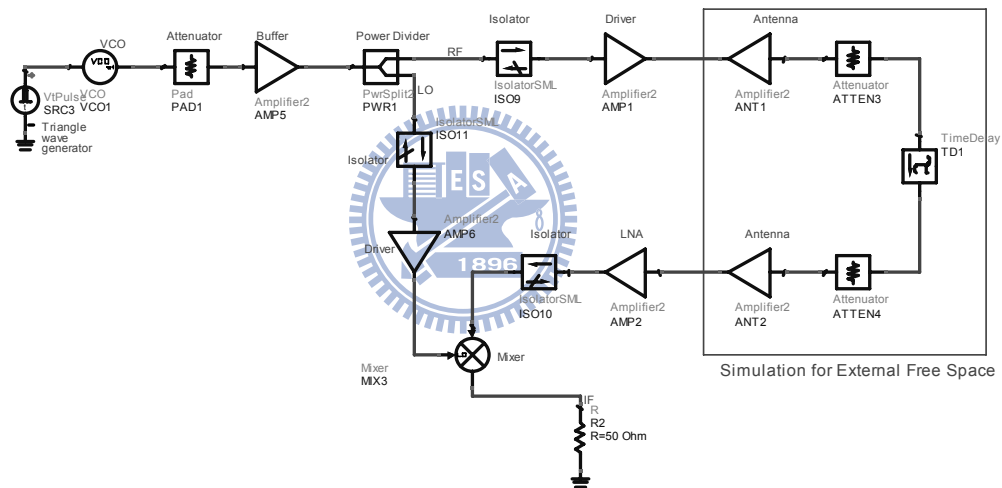
Fig. 2.9 FMCW radar system simulated environment

The most important components of the external path in the system simulation were two antennas, a delay line and the attenuators. Gain and return loss information regarding two antennas were obtained by measurement to set antenna blocks; the path loss was derived from the Friis formula, the delay time set based on the phase-delay of the modulated signal, and the RCS of the target was supposed to unity. The modulated signal was a 110 KHz triangular wave and the FM bandwidth was 50 MHz (Fig. 2.10). After the delay and the path loss

were adjusted, the beat frequencies can be determined and the ranges from the sensor to the target can be also estimated. As presented in Fig. 2.11, an example of beat frequency was derived at a distance of 9 m.
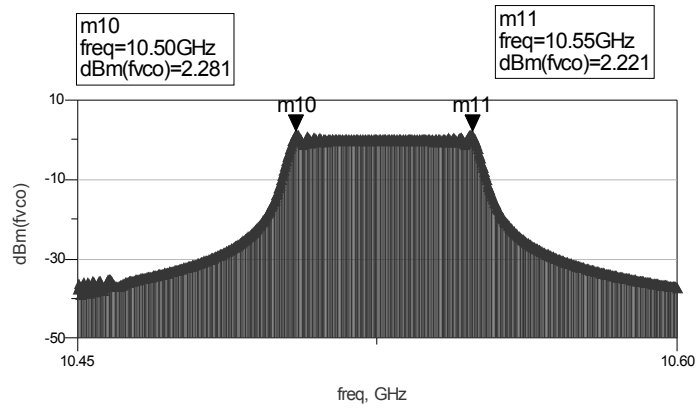
Fig. 2.10 The calculated bandwidth of LFM system is 50 MHz.
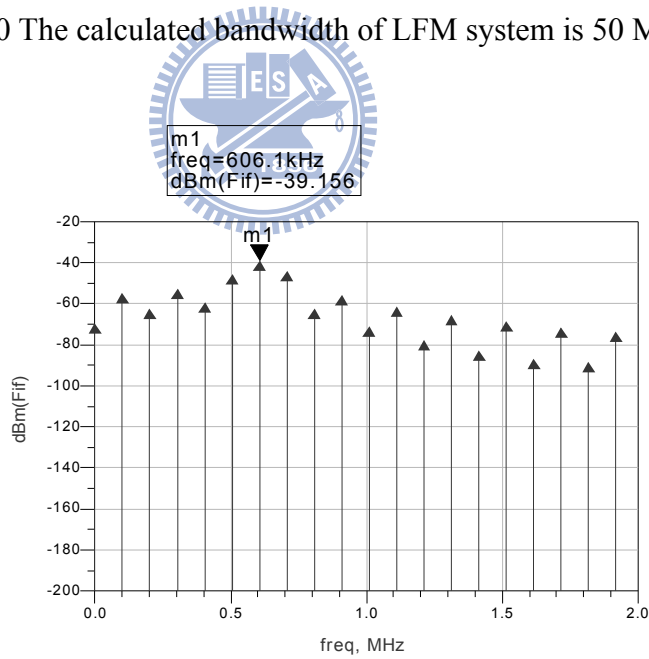
Fig. 2.11 The calculated range was set to 9m, and then the derived beat frequency was about 600 KHz.

CHAPTER 3

Design and Realization of the RF Transceiver

There are two versions of the RF CMOS transceiver in the paper. When the previous version updated to new version, the functions of VCO and more performances of other parts had been improved. And then above two structures of the RF CMOS transceiver have verified by the system simulation.

3.1 First Version CMOS FMCW Chip Design

Figure 3.1 shows the CMOS FMCW RF front-end in the region enclosed by the dashed line. The CMOS single chip transceiver receives an external triangular modulating signal provided by the analog signal-processing unit and feeds the triangular waveform to the on-chip voltage-controlled oscillator (VCO), followed by a buffer amplifier and attenuator. The transmitted signal is then split into two paths. The upper path encounters an isolator followed by a driving amplifier. The lower path encounters an isolator followed by an amplifier driving the local oscillator (LO) input port of the mixer.
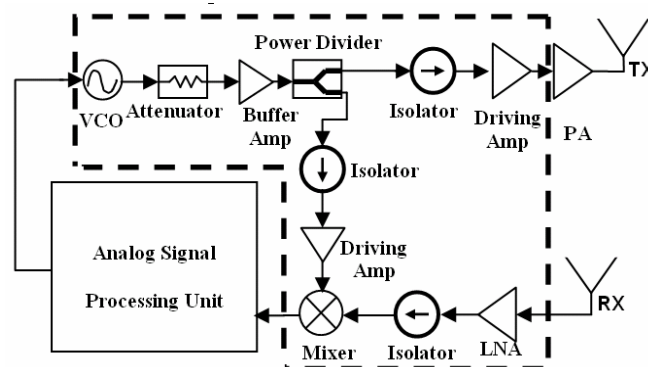
Fig.3.1 The X-band FMCW sensor system block diagram consists of two external antenna arrays, a single chip CMOS transceiver (enclosed by the dashed line), and an external analog signal-processing unit.

Since the power amplifier (PA) needs more consuming power and produces the higher noise level, so the design excluded a PA from the whole RFIC. And the external PA can flexibly adjust the system output power. The RF input port of the mixer receives the signal from the isolator followed by the low-noise amplifier (LNA), which receives the reflected signal from objects. The output of the mixer is fed into the analog signal-processing unit that demodulates received signals.

The CMOS FMCW RF (radio frequency) front-end is depicted in the region enclosed by the dashed line as shown Fig.3.1. The CMOS single chip transceiver receives an external triangular-modulating signal provided by the analog signal processing unit and feed the triangular waveform to the on-chip VCO (voltage-controlled oscillator), followed by a buffer amplifier and an attenuator. Then the transmitted signal is split into two paths. The upper path encounters an isolator followed by a driving amplifier. The lower path encounters an isolator followed by an amplifier driving the LO (local oscillator) input port of the mixer. The mixer's RF input port receives the signal from the isolator followed by the LNA (low-noise amplifier), which receives the reflected signal from objects. The mixer's output is fed to the analog signal processing unit for demodulating the received signals. The measurement setup of the probe test described in this section includes a Cascade[TM] M150 probe station, an Agilent[TM] 8510C vector network analyzer, an Agilent[TM] 8565E spectrum analyzer, an Agilent[TM] 54622A digital oscilloscope, and other accessory cables and tools. Each measured chip was copied from the sub-circuit of the CMOS transceiver in Fig. 3.1 and the measurements were made of sub-circuits of the complete circuit that incorporated I/O pads, which were for probe-testing.

The core technology employed in the CMOS transceiver design is critical to first-pass success of the FMCW sensor. Figure 3.2 shows a photograph of the single chip RF transceiver with each RF building block marked on the chip photo. Chip size is 2.4×1.3 mm, approximately $8.4\times10^{-2}\lambda_0$ by $4.55\times10^{-2}\lambda_0$ at the 10.5-GHz operating frequency. The so-called synthetic quasi-TEM complementary conducting-strip transmission line (CCS-TL) [31], [32] was employed throughout the entire RF chip design.
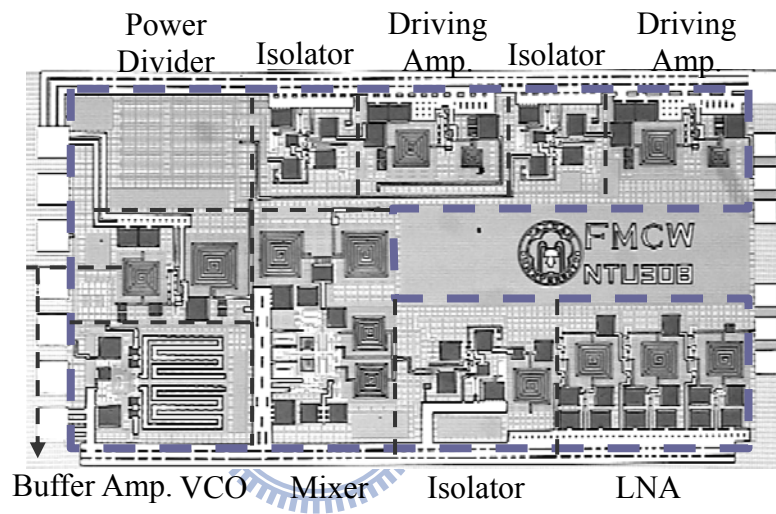
Fig.3.2 Chip photo of the CMOS FMCW transceiver

The CCS-TL can be identified by closely observing the chip photograph, in which one sees grids distributed throughout the chip. In this chip design, the signal trace is either located on the M6 (top) layer or M5 layer. The meshed ground plane is on the M1 (bottom) layer. The signal portion and perforated ground plane constitute a complementary pair with four arms reaching out for signal interconnections. The main features of the CCS TL are as follows. 1) The CCS TL flexibly synthesizes (non-unique solutions) the characteristic impedance and the slow-wave factor of a quasi-TEM line when a standard IC foundry process is used [32]. 2) The CCS TL is insensitive to variations in propagation characteristics by the transmission line for a compact microwave

circuit design [32]. 3) The reduction of electromagnetic coupling of adjacent components in the RF CMOS transceiver chip is significant. The CCS TL must be able to densely integrate various RF signal-processing components (Figs. 3.1 and 3.2) into a single chip. When adjacent coupling or crosstalk exist between the transmitting path and receiving path, demodulated signals show interfering signals that resemble an echo from a nearby object. Figure 3.3(a) shows a chip photograph of two closely coupled inductors using CCS TLs [33]. These inductors were placed only 90 μm apart. Figure 3.3(b) shows measured comparative studies of adjacent inductor coupling for inductors made of CCS TLs and inductors integrated directly onto a CMOS substrate.

(a)   (b)
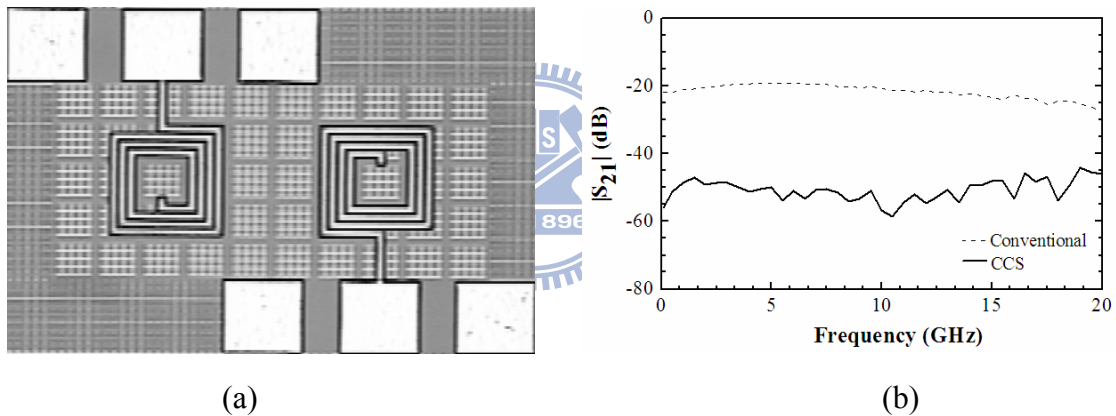
Fig. 3.3 (a) The chip photo for measuring cross-coupling of two inductors located 90 μm apart using CCS TLs, and (b) measured transmission coefficient of the adjacent inductors on the CMOS substrate.

Measured results show an approximate 30 dB improvement in coupling reduction at 1 and 20 GHz. Thus, potential CMOS substrate coupling is alleviated by using the synthetic CCS TL. All building blocks and inter-stage connections are utilized by the CCS-TL to achieve the highest attainable isolation required by the FMCW sensor [34]. Notably, the Wilkinson power divider at the upper left corner of the chip photograph (Fig. 3.2), consisting of two 70.7 Ω CCS TLs with a shunt 100 Ω resistor at two output ports, occupies

only 400 μm by 280 μm, occupying $1.372 \times 10^{-4} \lambda_0^2$ in chip area. Measured transmission loss was 6.5 dB, which is very close to the theoretical value of 6.3 dB obtained by the electromagnetic (EM) simulation software of $HFSS^{TM}$. The measured input (output) reflection coefficient was −16 (−20) dB, which is also very close to theoretical prediction of −15.3 (−22) dB. In [34] the details of how the active building blocks were designed and tested individually in the test chips.

A brief description of the design and test of the CMOS isolator, which is important for providing isolation in the signal path, is given here. The study adopts the circuit topology developed by Podell and Ali [35] and applies it to the 0.18 μm CMOS technology. Figure 3.4 (a) shows the schematics of the CMOS isolator, which is a parallel combination of a common base (M2) and source follower (M1) stage. The capacitor, C1, is used for compensating the insertion loss. The input and output DC blocking capacitors, C2 and C3, are also integrated into the CMOS isolator design. The simple architecture result in the electronic isolator only occupies 300×320 μm of chip area. Figure 3.4(b) shows measurement results of the CMOS isolator. Measurement data implies that the best response of inverse isolation <−25 dB is at 1–20 GHz. Hence, the isolator is added to the transmitter and receiver paths to isolate the VCO from reflecting the signal caused by the impedance mismatch on signal paths.

(a)   (b)
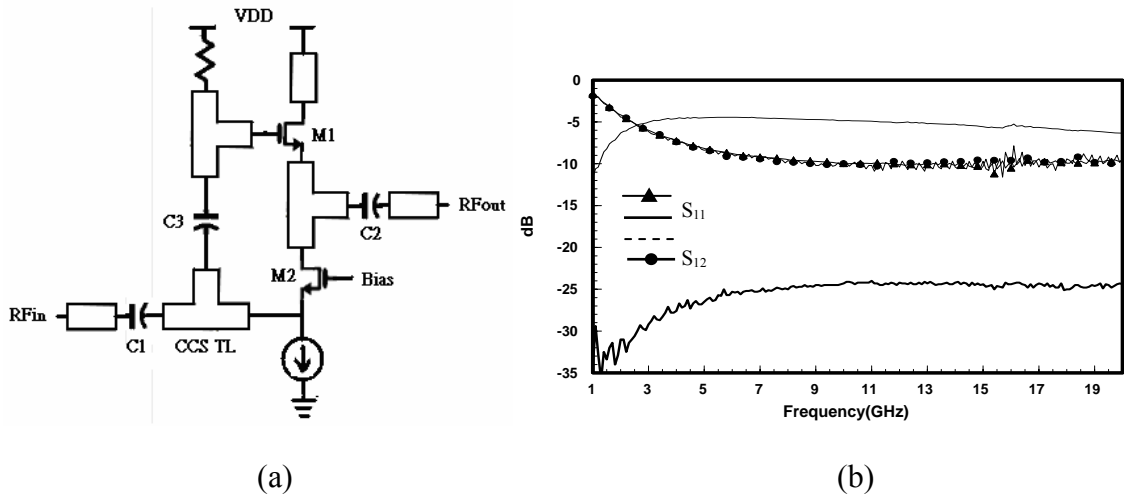
Fig. 3.4 (a) Schematics of the CMOS isolator, and (b) measured S-parameters of the 0.18μm CMOS isolator

Off-chip package measurement was conducted to evaluate transmitter performance. The continuous-wave (CW) power measured at the output of the external power amplifier was −4.65 dBm, whereas −12.5 dBm was obtained under FMCW modulation with a 50-MHz bandwidth. Figures 3.5 (a) and (b) show the single tone CW output spectrum centered at 10.5 GHz, and the frequency-modulated output spectrum, respectively, illustrating good signal quality ready FMCW sensor assessment.
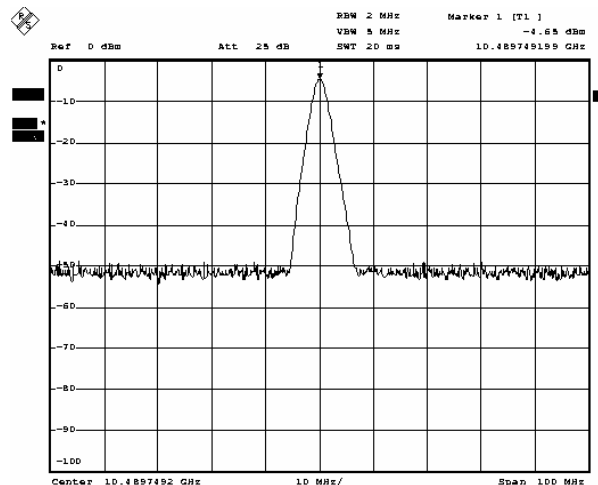
(a)
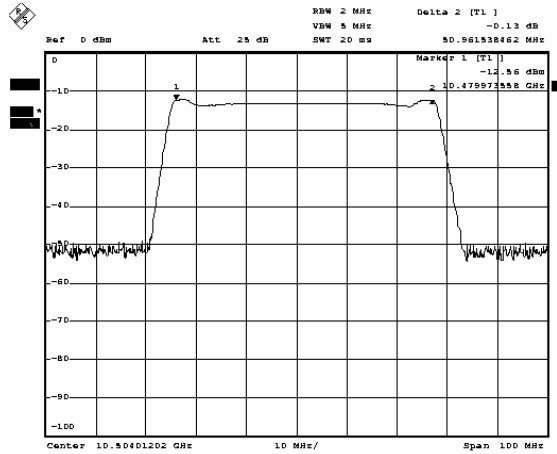
(b)

Fig. 3.5(a) The FMCW transceiver at continuous-wave (CW) mode; (b) output spectrum of the FMCW transceiver with frequency modulation at 50.0 MHz

Table 3.1 Performance of Prototype in Fig. 3.2

f=10.5 GHz		
Buffer Amp	Gain	-2.5 dB
	Return-loss	10.0 dB
	Reverse isolation	8.1 dB
Driving Amp	Gain	2.2 dB
	Return-loss	-7.0 dB
LNA	Noise figure	6.0 dB
Mixer	Isolation (RF-to-IF)	38.4 dB
	Isolation (LO-to-IF)	27.3 dB
	Conversion gain	3.5 dB
Isolator	Gain	-5.0 dB
	Return-loss	10.1 dB
	Isolation	25.2 dB
Power Divider	Insertion loss	6.5 dB
	Return-loss at input port	16.0 dB
	Return-loss at output port	20.2 dB
Attenuator	Attenuation	3.1 dB

3.2 New Version CMOS FMCW Chip Design

Figure 3.6 shows the building blocks of the X-band FMCW sensor, which are as follows: dual planar antenna arrays at the transmitter output and the receiver input; a 0.18μm 1P6M CMOS fully integrated monolithic transceiver, which performs most of the required RF signal processing, and is shown inside the dashed lines, and a baseband digital signal processing unit for the instantaneous and simultaneous assessment of range measurements. Notably, the use of two antennas rather than only one eliminates the need for a circulator, which is generally expensive and does not provide sufficient isolation between the transmitter and the receiver.

The frequency of the FMCW sensor was set to 10.5GHz to comply with regulations pertaining to transportation management systems for monitoring instantaneous transportation of highway vehicles [14]. The transceiver of the sensor, as enclosed by the dashed line in the Fig. 1.1, was fully implemented by 0.18μm 1P6M CMOS technology. All the components, including voltage controlled oscillator, amplifiers, mixer, power divider, were realized and combined using an innovated guiding structure, called the complementary-conducting-strip transmission line (CCS TL) on the standard silicon substrate. Figure 3.6 shows a photograph of the single-chip CMOS transceiver, containing all necessary RF building blocks of the FMCW sensor system. The chip size, including the necessary contacting pads, was 1.68mm×1.6mm, corresponding to $5.9 \times 10^{-2} \lambda_0$ by $5.6 \times 10^{-2} \lambda_0$ at 10.5GHz. The pad of the transmitting path in Fig. 3.6 that connects with the TX antenna arrays is enclosed by black lines and labeled "TX"; the other pad of the receiving path in Fig. 3.6 that connects with the RX antenna arrays is also enclosed by black lines and labeled "RX".

The guiding technology adopted in the design of CMOS FMCW transceiver is essential to the first-pass success of the sensor system. The CCS TL was adopted throughout the RF chip design, [31]-[32]. The proposed chip locates the signal trace on the top metal layer, and the meshed ground plane on the bottom metal layer [36]. The CCS TL significantly reduces the electromagnetic coupling of the adjacent components on the CMOS substrate, where various RF transceiver building blocks must be compact and placed in close proximity to save chip area [34],[36]. Hence, all building blocks and their inter-stage connections are realized by the CCS TLs in order to maximize the attainable isolation required by the FMCW sensor. The good isolation achieved in the CMOS RF transceiver diminishes the degree of difficulty of the IF filter design or DSP control method, thus canceling the leakage from the transmitting port to the receiving port [37].
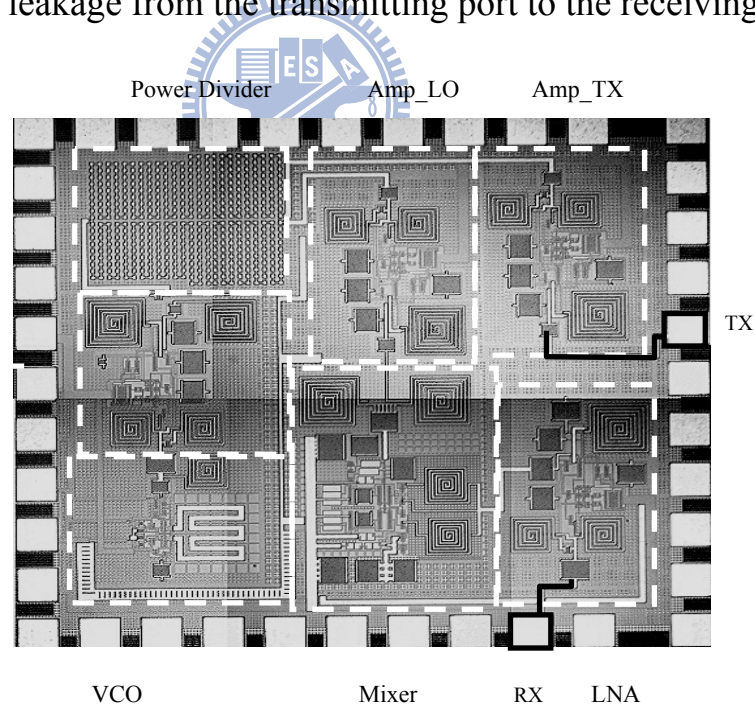
Fig.3.6 The 0.18μm CMOS FMCW transceiver. The chip comprises a VCO, a buffer amplifier, a power divider, a low-noise amplifier and two driving amplifiers.

The triangular wave, which is controlled by the external digital signal processing unit, is fed to the on-chip voltage-controlled oscillator, as indicated in

Fig. 1.1. The transmitted signal is then split into two paths using an integrated two-way equal-split power divider, which is fully realized by the CCS TL. Figure 3.6 shows the two-way Wilkinson power divider, which is located on the upper left corner of the chip, and which comprises two 70.7Ω CCS TLs and an isolation resistor of 100Ω shunting two output ports. The size of the power divider is only 400μm×280μm, corresponding to $1.372×10^{-4}λ_0^2$ at 10.5GHz. The driving amplifier (Amp_TX in Fig.3.6) is fed by the upper output of the power divider through a CCS TL with a length of 320μm, thus completing the transmitter path of the CMOS transceiver. The lower output port is connected to another driving amplifier (Amp_LO in Fig.3.6) by a CCS TL of 670μm. The two driving amplifiers are identical in the present CMOS transceiver. Figure 3.7 shows the measured results of a composite network comprising two driving amplifiers and a CCS TL power divider. The network had transmission coefficients of −2.0dB and 0dB for the TX-path and the LO-path, respectively. The measured input reflection coefficient at 10.5GHz was about −16.6dB in the 50Ω system. The measured isolation between the TX-port and the LO-port at 8−12GHz was higher than 40dB, revealing that the network combining the CMOS Wilkinson power divider and driving amplifier had very low electromagnetic coupling. The design of the voltage control oscillator is based on the typical differential cross-coupled VCO, which is well documented [38]. The *p*-type differential cross-coupled pair is considered as a negative differential resistor, and the core resonator is realized by two quarter-wavelength CCS TLs (Fig. 7 of [39]). To simplify the thesis and because of the special purpose to which is applied, the measurement of speed is omitted. The measured chip is copied from the sub-circuit of the CMOS transceiver in Fig. 3.6 which comprising two driving amplifiers and a CCS TL power divider. The measured

frequencies are from 8 to 12GHz and the measured scatter parameters of the on-chip are shown in Fig. 3.7. The measurements were made of sub-circuits of the complete circuit that incorporated I/O pads, which were for probe-testing.
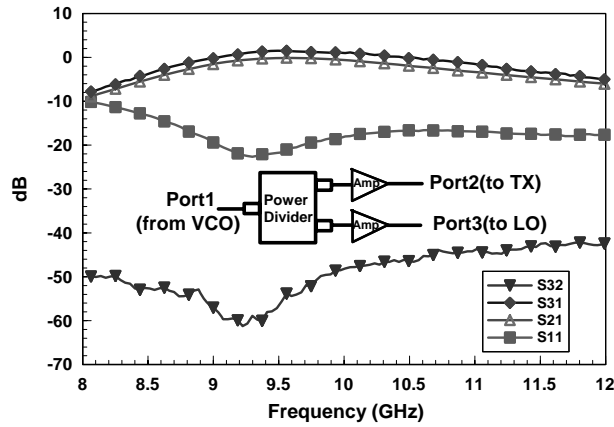
Fig. 3.7 Measured scatter parameters of the on-chip TL-based power divider with two driving amplifiers in the 50Ω system.

The MOS capacitor is applied as a varactor for the frequency control of the VCO shown in Fig. 3.8(a). According to the on-chip measurements, the output power of the VCO was −18dBm, and its corresponding phase noise was −83.2dBc with an offset frequency of 100.0 KHz from the carrier at 10.5GHz. Figure 3.8(b) illustrates the frequency tuning at 9.3GHz–11.0GHz. The fundamental linearity that enclosed by the dashed line in Fig. 3.8(b) was about 0.06%. However, the VCO linearity cannot immediately be applied to estimate the performance of the FMCW system. The real linearity of VCO corresponds to the definition of linearity of FMCW system, since the range resolution correlates directly with the modulated bandwidth. Therefore, a new method is adopted to calculate the linearity of VCO. Additionally, the proposed VCO is experimentally characterized with the input triangular wave. Figure 3.8(c) shows the frequency modulation bandwidth against the amplitude of the triangular wave at 10.38GHz. That is, the frequency of 10.38GHz is relative to the initial

peak value of the triangular wave. Increasing the amplitude of the control voltage from 12.0mV to 150.0mV increased in the bandwidth of the output frequency-modulated signal from 50.0MHz to 550.0MHz. The VCO linearity under a modulation bandwidth of 500MHz was estimated as 3.0 % by following the computation in Fig. 6 [39]. The curve shown in Fig. 3.8(c), based on (2-4) in chapter 2, is directly linked to the control-scheme for the range measurement using the proposed CMOS sensor in the chapter.

(a)

(b)

(c)
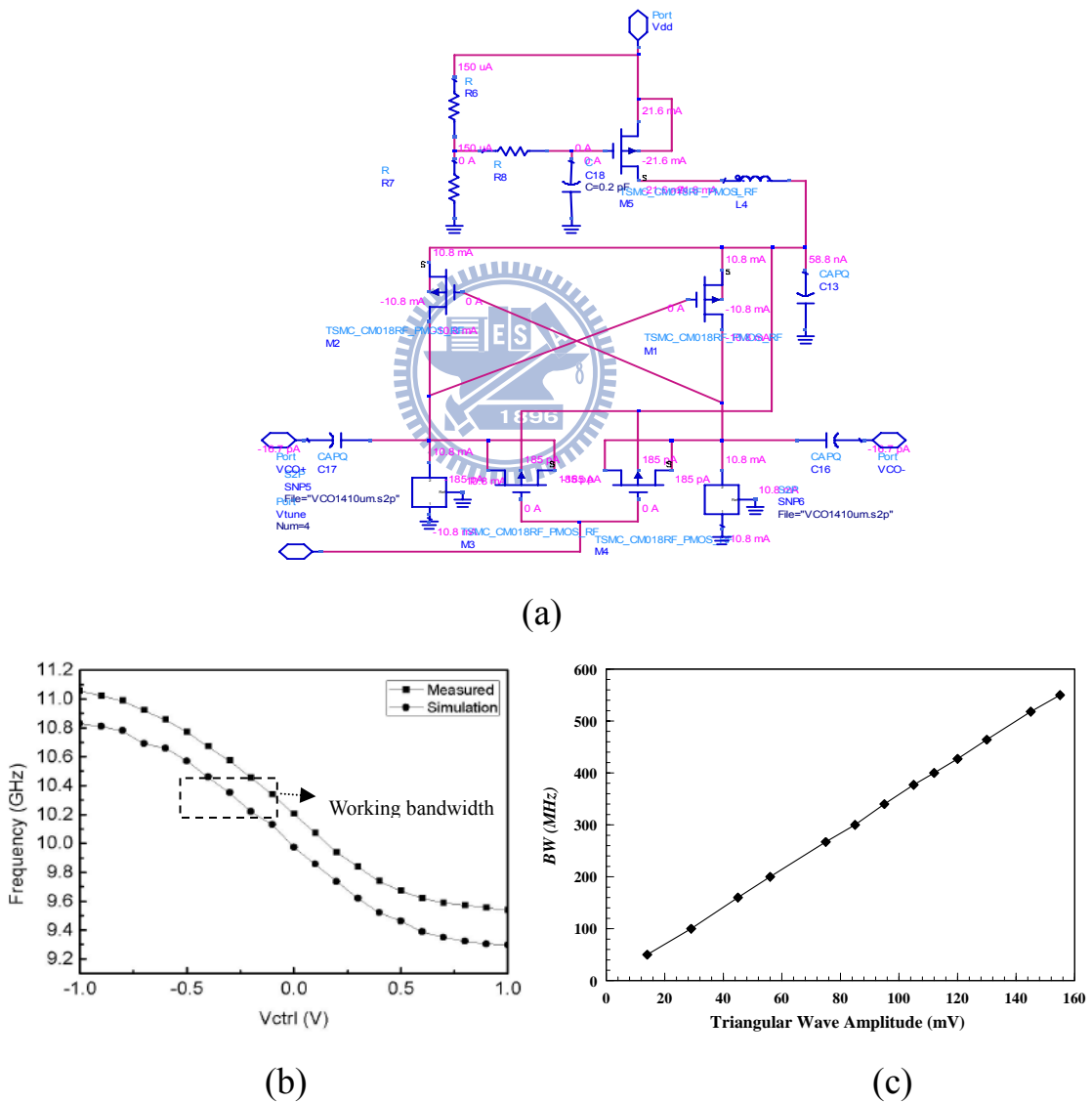
Fig. 3.8 (a) Schematic of the VCO by the MOS capacitor, (b) Frequency tuning characteristics, and (c) measured modulated bandwidth against the input amplitude, of the triangular wave for the on-chip VCO in CMOS transceiver.

The receiver path comprises a mixer and an LNA. The mixer was a MICROMIXER, as described by B. Gilbert [40]. The single-ended RF input was matched and converted differentially to the core of the mixer. The output of the IF was located on the left-hand side of the CMOS transceiver, followed by the external digital signal processing unit for the signal analyses. The measured LO-port reflection coefficient, RF-port reflection coefficient and conversion gain of the mixer were −12dB, −17dB and −6 dB, respectively. The isolations between the adjacent ports of the mixer were characterized by the on-wafer measurements. Furthermore, the isolations between the transmitting path and receiving path in the proposed transceiver were also experimentally studied [33], [36]. The on-chip VCO was activated and controlled by the triangular wave during the experiments. An Agilent[TM] 8565E spectrum analyzer was adopted to observe the signal at output and input ports of the transmitting and receiving paths, respectively. Figures 3.9(a) and (b) display two measured spectrums. The power spectrum of the receiving path was 55dB less than that of the transmitting path at 10.5GHz. These measured results confirm that the proposed system obtained high leakage suppressions by using the CCS TL guiding structure throughout the entire chip design. Since the original power spectrum of receiving path in Fig. 3.9(b) was sunk in the noise floor by the general parameters setting of the spectrum analyzer, the slight power of receiving path wasn't discovered until the resolution bandwidth (RBW) of the spectrum analyzer was properly adjusted. To ensure consistency of measurement, to RBW of the spectrum analyzer is set to the same value in the measurement of transmitting power. When the RBW of the spectrum analyzer was reduced, the bandwidth of the first-stage filter of the RF input port was also degraded. Therefore, the power spectrum of Fig. 3.9(a) exhibits slight distortion with the

narrow RBW. It therefore explains the two power peaks in the spectrum of Fig. 3.9(a). Table 3.1 summarizes the performance of the prototype shown in Fig. 3.6. The prototype combines all RF functions for FMCW sensor, and has an external medium power amplifier to increase the output power to 0dBm. Measurement results of the chip indicate two properties that are helpful for developing the FMCW sensor: there are the VCO linearity of 3% of the modulated bandwidth against the triangular wave amplitude from 10.3GHz to 10.8GHz, and the on-chip isolation of 55.0dB at 10.5GHz.
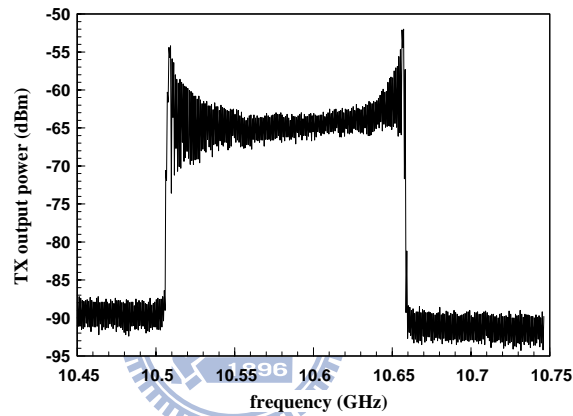
(a)
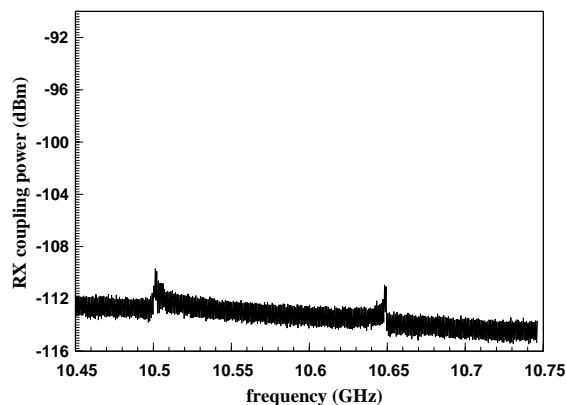
(b)

Fig. 3.9 Measured spectra of the CMOS FMCW transceiver: (a) spectrum at output of transmitting path, (b) spectrum at input of receiving path.

Table 3.2 Performance of Prototype in Fig. 3.6

f	10.5 GHz		
Supply Power	3.0 V / 64 mA		
Output Power	-18.2 dBm		
Noise Figure	10 dB		
Building Block	VCO	P_{out}	−18 dBm
		Phase-noise	83.2 dBc
		Linearity	3 %
	Buffer Amp	Gain	0 dB
	Driving Amp	Gain	9.25 dB
	Power Divider	Insertion loss	6.5 dB
		Isolation	40.0 dB
	LNA	Gain	6.2 dB
		Noise Figure	5.3dB
	Mixer	Isolation (RF-to-IF)	38.4 dB
		Isolation (LO-to-IF)	27.3 dB
		Conversion gain	−6.0 dB

Eventually, the future improvement of CMOS RF ICs is a temperature compensation circuit design, can overcome the frequency drift and promote a stable VCO circuit. At the same time, we will enhance the speed measurement accuracy of the field test.

3.3 Package of CMOS FMCW Chip

All pads size on RFIC were 100 μm×100 μm. Set the size of pads on PCB were 200 μm×200 μm, and the distance from RFIC pad to PCB pad was 500 μm. The diameter of bond wire was 0.7mil (0.01778 μm); the specification was defined by IST. The simulation setup of wire bonding was designed by Ansoft^TM HFSS. In the chip package, there were two types of via hole, one via holes were next on the chip (Fig. 3.10 (a)), and the other were bored of being in the bottom of the chip (Fig. 3.10 (b)).
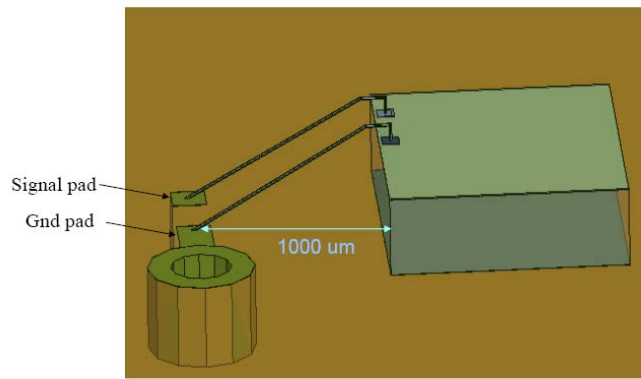
(a)
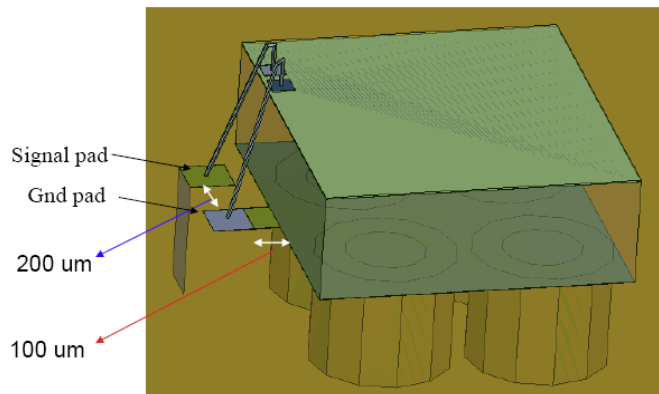
(b)

Fig. 3.10(a) via holes was next on the chip in the chip package, and (b) via holes was in the bottom of the chip.

While via holes were in the bottom of the chip package with a better frequency response that was shown in Fig. 3.11 (b), but then more easily lead to mount chip failure by its uneven surface. On the other hand, Figure 3.11 (a) illustrated the via-holes were next to the chip on a package more easily mount the circuit board, but its relatively poor frequency response.
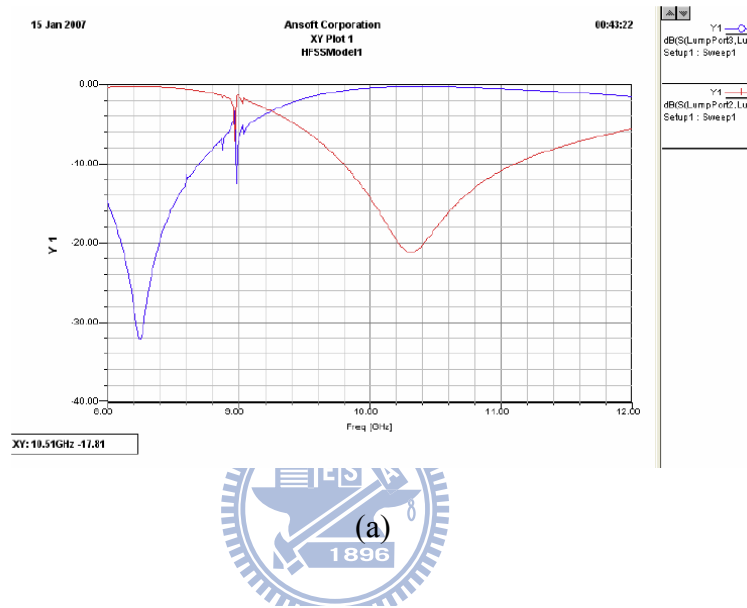
(a)
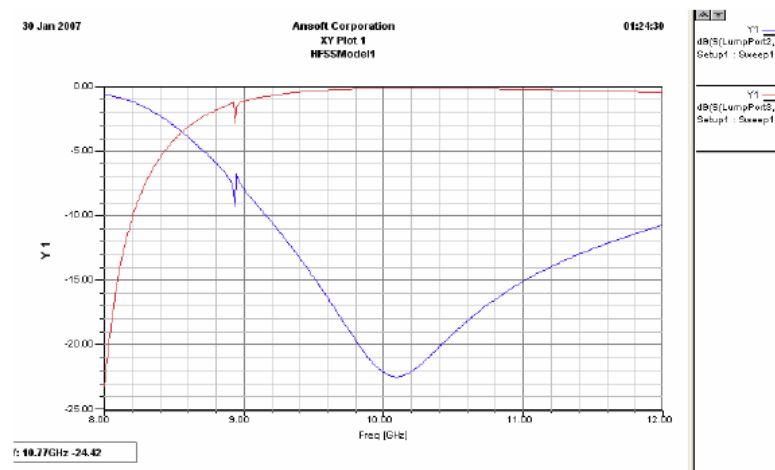
(b)

Fig. 3.11(a) the response of via holes was next on the chip, and (b) the response of via holes was in the bottom of the chip.

Figure 3.12 was shown that matched concept of a CMOS transceiver (RFIC)

package. The first stage of the matched network design was made a L-section to match the output impedance of wire-bonding to 50Ω, and the second stage of the matched network design another L-section to match the input impedance of the external driving amplifier to 50Ω.
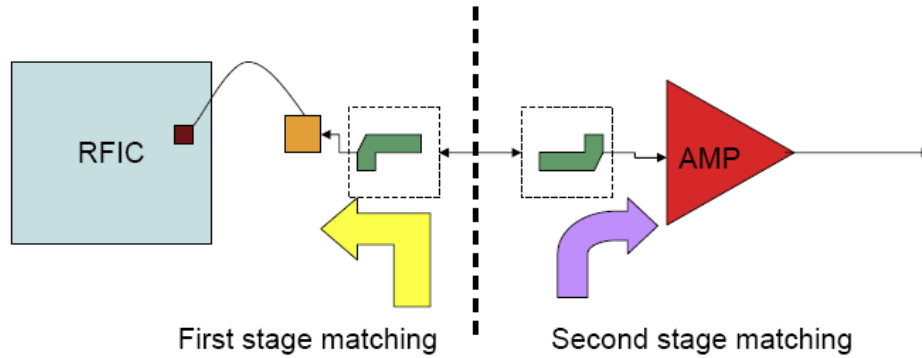
Fig. 3.12 The matched concept of a CMOS transceiver (RFIC) package for the transmitter port matching.

In the first stage, the return loss of the transmission port of the RFIC was measured from the probing test by cascade[TM] M150 and the S-parameters of the bond wire were obtained from the linear simulation by Ansoft[TM] HFSS. The L-section matched network design for the output impedance of wire-bonding was made by Agilent[TM] ADS2006, and then the network would be matched to 50Ω. Figure 3.13 displayed the structure and result of the simulation. It was combined with the L-section matched network and SP files (S-parameters) of the bond wire and TX output of RFIC. The purpose of this simulation was built the physical layout for the L-section matched network and matched the impedance of a signal path to 50Ω. Therefore, the smith chart would be applied to the matched network design, the lengths and widths of the L-section were adjusted to leading the curve of S_{11} (the return loss of the path) to 50Ω at the operating frequency (10.525GHz). In the second stage, the S-parameters of the external driving amplifier were obtained from the Hittite[TM] datasheet. The L-section

matched network design for the input impedance of the external driving amplifier was also made by Agilent[TM] ADS2006. Figure 3.14 displayed the structure and result of the simulation.
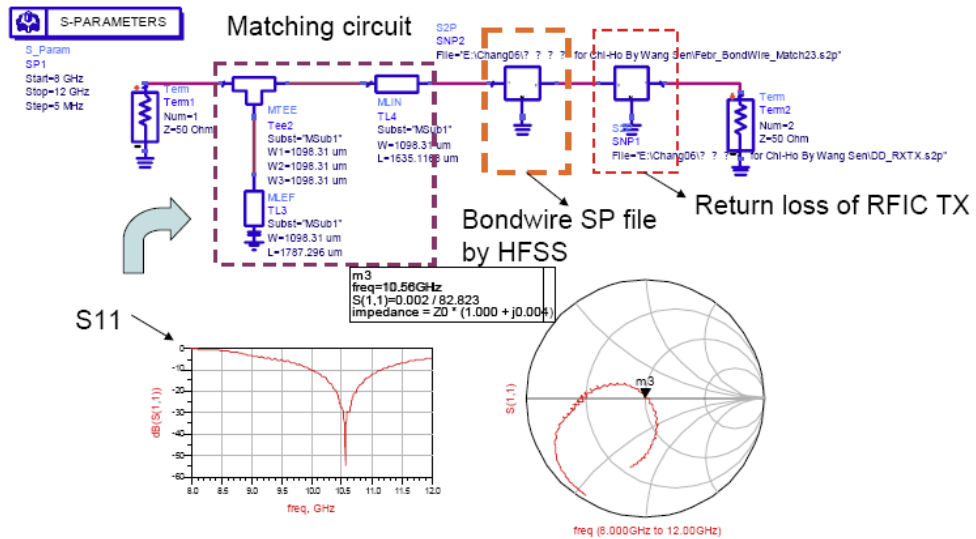
Fig.3.13 The structure and result of the output impedance matching were illustrated for the wire-bonding.
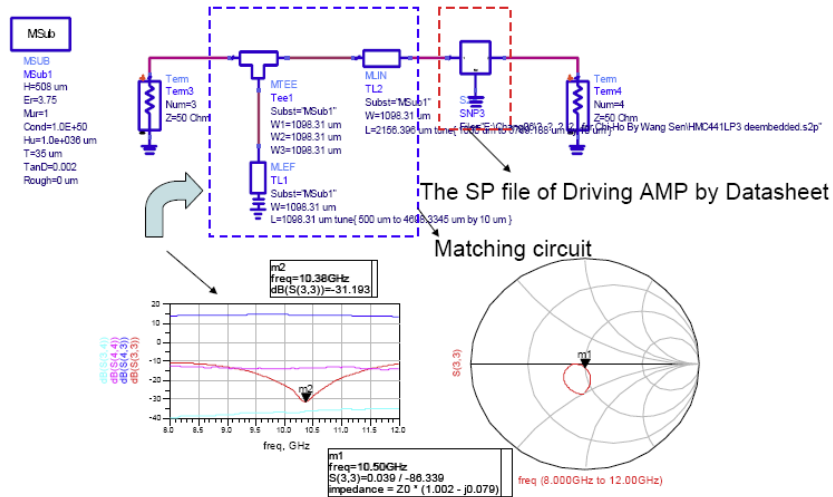
Fig.3.14 The structure and result of the input impedance matching were illustrated for the external driving amplifier.

If the mismatched impedance was still existed between the output of the wire-bonding and the input of the external driving amplifier, then the π-pad

design would be used to compensate the mismatched impedance. First the prototype model was made from ideal components of Agilent™ ADS2006, the schematic and the response of π-pad design was illustrated in Fig. 3.15.
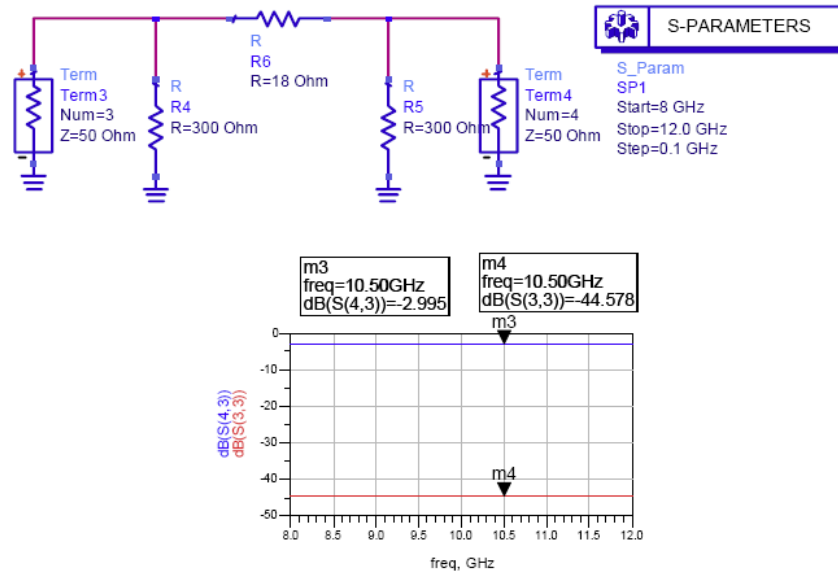
Fig. 3.15 The schematic and response displayed of the ideal π-pad design.

Nevertheless, the physical transmission line would be considered in the π-pad design. The layout of transmission lines designed according to the size of physical resistors of π-pad and the operating frequency. The layout, schematic, and response of π-pad design were shown in Fig.3.16, but the response result was poor in operating frequency. The resistance values of π-pad would be recalculated with pad effect. After re-calculation, the resistance of 18Ω was changed to 30Ω and 300Ω was changed to 540Ω, then the better response result was obtained and displayed in Fig. 3.17.
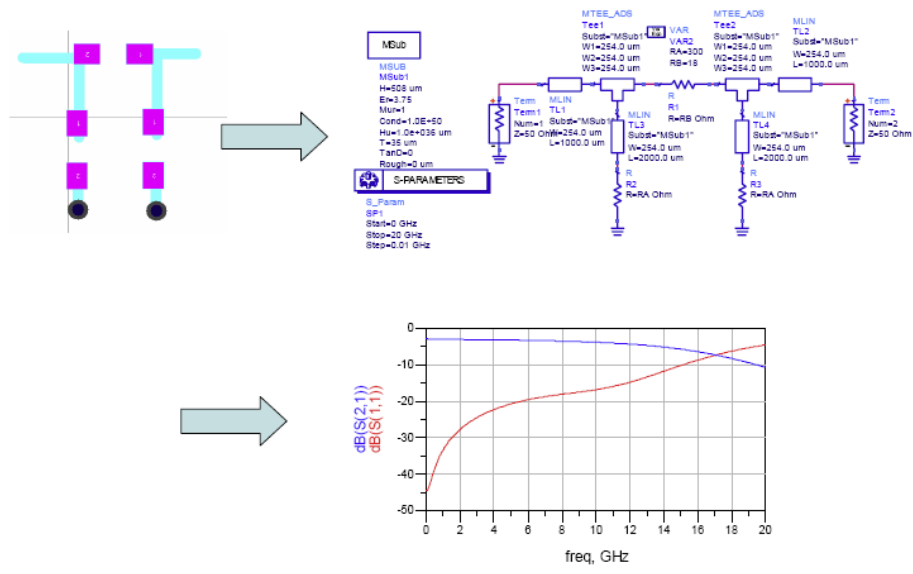
Fig.3.16 The layout, schematic, and response of π-pad design with pad effect of the transmission line.
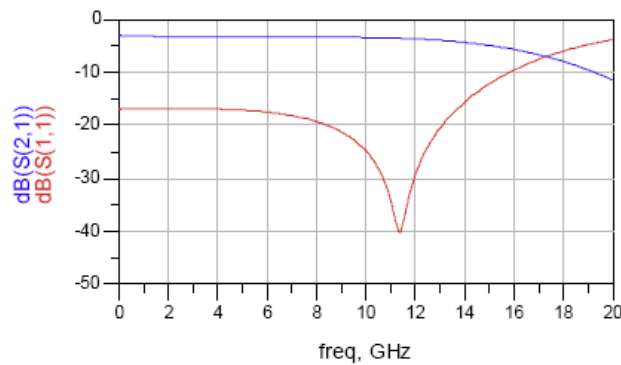
Fig. 3.17 Better response results after recalculated the resistors of π-pad design.

After the matching process, the package job would be started, the pin assignment of RFIC should be defined (Fig. 3.18), then the RF pads would be matched to the proper impedance that was like the above matching process and DC pads could be connected directly with the ESD circuits. Figure 3.19 demonstrated the physical layout pads definition of the CMOS transceiver (RFIC).
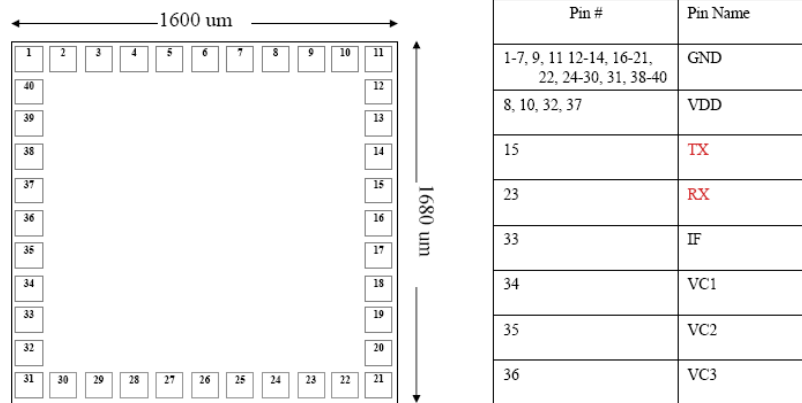
Fig. 3.18 Pin assignment defined for the CMOS transceiver (RFIC).
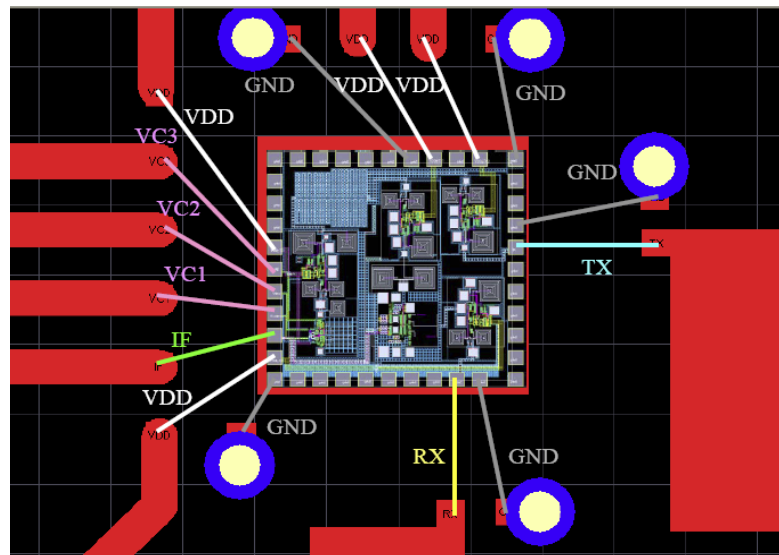
Fig 3.19 Physical layout defined for the CMOS transceiver (RFIC).

Additionally, the CMOS RF transceiver IC was wire-bonded (golden wires of 0.7 mils in diameter) directly on the RO4003[TM] substrate separately for evaluation purpose. As shown in Fig. 3.20 the CMOS chip was silver glued on the substrate before bonding and before the glow top epoxy process was performed. The wire inductance were compensated for by the additional matching circuits on the board to ensure the RF signal integrity or was used as part of the RF choke for DC bias. The matching circuit was made from well-known transmission line L-matching circuits with a single stub. A

46

parallel-coupled filter was added on the board between the L-matching circuit and the antenna arrays.
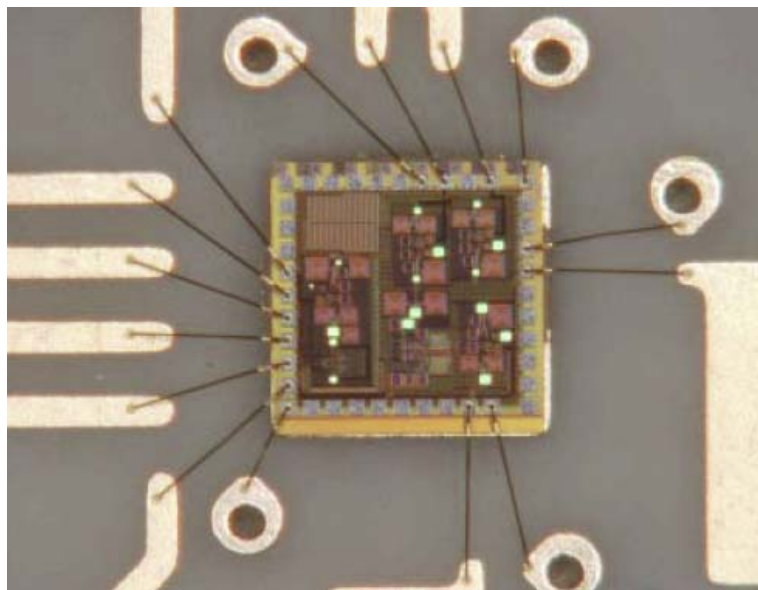
Fig. 3.20 Photograph of FMCW CMOS die attached to board with aluminum bonding wires.

CHAPTER 4

Dual Leaky-wave Antenna Arrays Structure Design with High Isolation and High Gain

The traditional $\csc^2\theta$ type antennas were designed by technology of the aperture or the reflector antenna [20], [41] and applied both airborne and surveillance radar for military utilization. However, those operations of military possess the greater power consumption, large scaling volume, more complicated structure, and farther distance measurement. Especially, the characteristics of $\csc^2\theta$ type antennas were the special pattern compensates for the space loss of $1/R^4$ that can perform suitably the range measurement of multiple-lane for TMS application. Furthermore, the short range detection and low power depletion were required for this application, and then the FMCW detected method was considered to achieve the new system.

4.1 The Design Method of the Leaky-wave Antenna Arrays

The $\csc^2\theta$ pattern was our special design that increases the length of the antenna, which the characteristics of the $\csc^2\theta$ pattern became increasingly apparent. The characteristic curve was showing a range between the two dashed-lines in Fig. 4 of [42]. The theory of a $\csc^2\theta$ pattern of leaky-wave antenna has already been derived and proved in [42]. For the article how to use one element of the leaky-wave antenna to design a $\csc^2\theta$ pattern for the method illustrated, the variable length of the antenna metal (Fig. 4.1) adjust gradually to prove that the $\csc^2\theta$ pattern of the design concept by the numerical solution. The return loss of one element of the leaky-wave antenna at the operating frequency

was shown in Fig. 4.2.

Fig. 4.1 Tuning the metal length of one element of the leaky-wave antenna array.
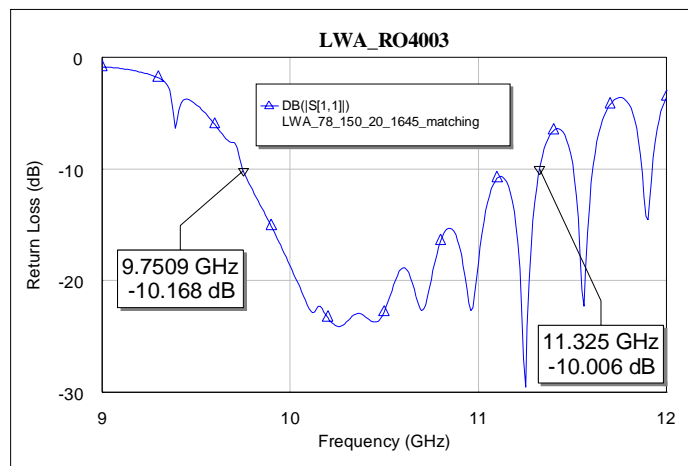
Fig.4.2 Return loss of one element of the leaky-wave antenna.

4.2 The Integration and Realization of Leaky-wave Antenna Arrays

First design a pair differential port to feed one element of the leaky-wave antenna array. Figure 4.3 shown the structure (balun) of a differential input of one element of antenna array and achieved a phase difference of 180° between those ports. Secondly, the differential feeding network has been realized and then the equal power divider is designed to combine each element of the leaky-wave antenna array (Fig. 4.4). After feeding design, the full wave simulation of the whole feeding network of the leaky wave array was executed by IE3D^{TM}, and Fig. 4.5 shows the structure for the feeding network with an 8-element array.
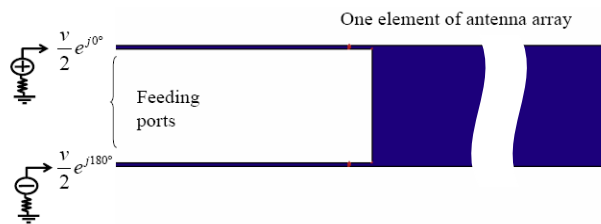
Fig. 4.3 Feeding ports of one element of the leaky-wave antenna array
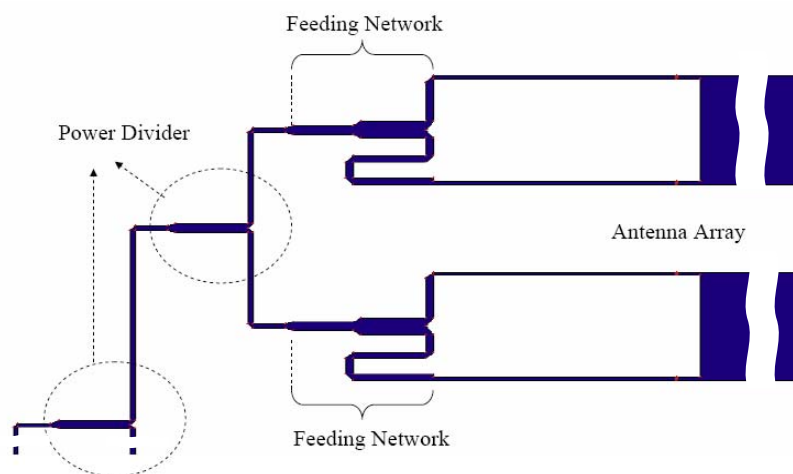
Fig. 4.4 Feeding network and power divider of the leaky-wave antenna array
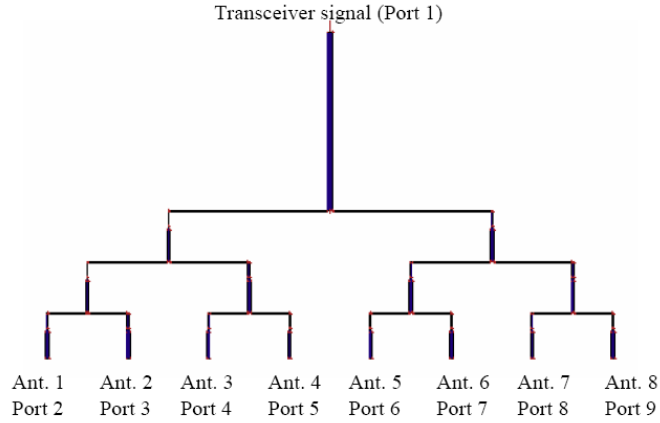
Fig. 4.5 Whole feeding network of the 8-element leaky-wave antenna array

The proposed antenna was designed to operate in the first high-order leaky mode (EH_1) of a microstrip excited differentially at the X-band [43], [44]. And the derivation and explanation of the leaky-wave antenna theories are found in [43]-[48]. The basic structure of a leaky-wave antenna comprises a feeding network and a substance of antenna. Additionally, the leaky-wave antenna design is used as the differential feeding structure to excite the leaky mode. As shown in Fig. 4.6, this antenna array may consist of a set of equal power dividers of a feeding network [43]. And eight matching baluns for the differential input of each element of antenna [44], [46], and microstrip leaky-wave antennas of length (L) 150.0mm, width (W) 7.80mm, spacing (S) 6.40mm, and thickness (h) 0.508 mm in the designed array. The designed antennas are fabricated on RO4003^{TM} substrates that have a relative dielectric constant (ε_r) of 3.5. The baluns were realized by a microstrip circuit with a phase difference of 180° between two differential ports and the equal power dividers were designed to combine all elements of the leaky-wave antenna array. Figure 4.7 shows the results of simulation of the feeding network with an 8-element array.
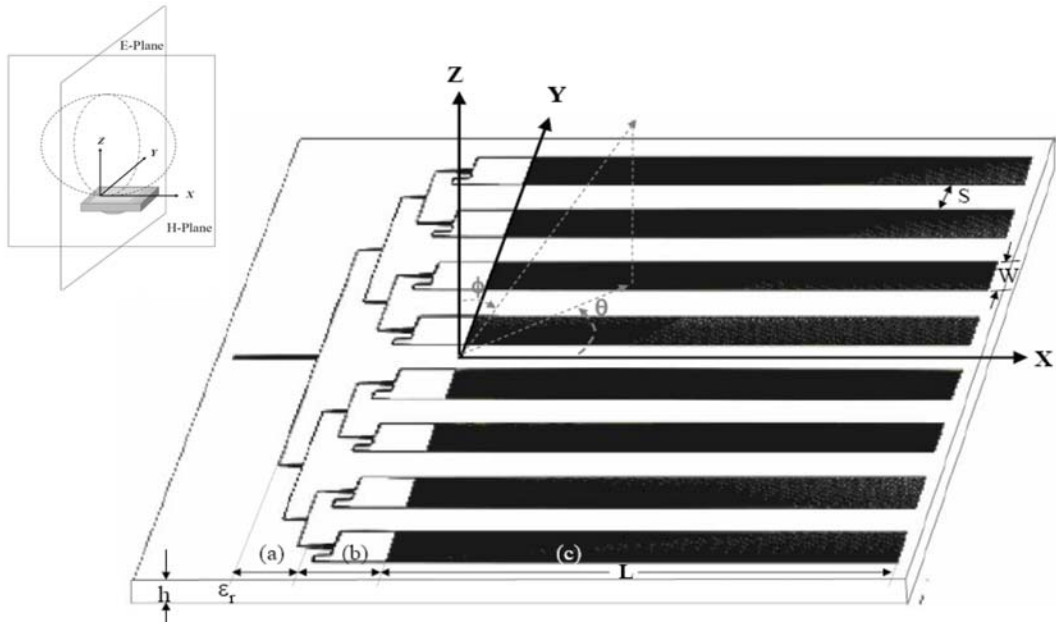
Fig. 4.6 The Leaky-wave antenna array, including (a) a set of equally power dividers of feeding network, (b) 8 matching baluns for the differential input of each element of antenna, and (c) Microstrip leaky-wave antennas with length of L, width of W, and spacing of S on the top side of the substrate.
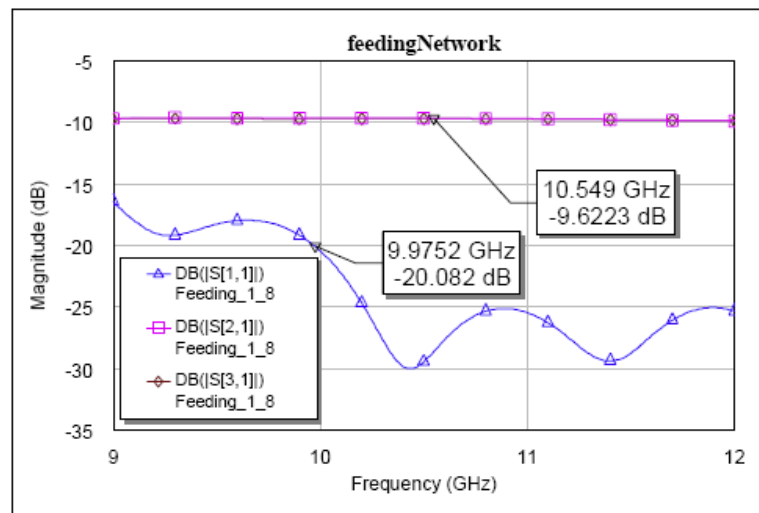
Fig. 4.7 Performance of the feeding network for the 8-element array

According to depending on the relationship between the propagation constants of the guided mode, the higher-order modes of the microstrip line can be divided into the following four frequency regions [46]:

1) $\beta > \beta_S$, $\alpha = 0$, bound mode region;

2) $\beta_S > \beta > k_0$, small α, surface wave leakage region;

3) $k_0 > \beta$, small α, surface wave and space wave leakage region;

4) $k_0 > \beta$, large α, cutoff region.

with β is the phase constant and α is the attenuation constant of higher-order mode of the microstrip line, β_S is the propagation constant of the surface wave mode of the surrounding structure, and k_0 is the wave number in the air. The original concept of this proposed antenna array is from the design of [43]. Moreover, the dispersion characteristics of the leaky-wave antenna between the operating frequencies derive an inequality as $\beta < k_o$, with small α. β is the phase constant and α is the attenuation constant of the microstrip line higher-order mode, and k_o is the wavenumber in the air. In [46], the inequality represented the higher-order modes of microstrip line can be entered the surface wave and space wave leakage region.

A simple procedure of the leaky-mode antenna array was designed according to using one of two approaches, namely, E-plane and H-plane techniques. In an E-plane antenna array, the number of antenna elements controls beam width of the E-plane pattern, and coarsely tunes gain. Table 4.1 shows the beam width and gain of an E-plan antenna. In an H-plane antenna array, the length of each antenna element regulates the beam width of the H-plane pattern, and fine tunes gain. Table 4.2 shows the beam width and gain of an H-plan antenna.

Table 4.1: E-Plane Beam-width and Gain vs. the Number of Antenna Elements

No. of antenna elements	2	4	8
Beanwidth of E plane (°)	60	26	12
Gain (dB)	12	15	18

Table 4.2: H-Plane Beam-width and Gain vs. the Length of one Element

Length of one element (mm)	50	100	150	200	300
Bandwidth of H plane (°)	30	22	20	19	19
Gain (dB)	7.5	10.8	11.8	12.0	12.1

Preceding paragraphs have already pointed out the E-plane and H-plane in our design, so the relationship was redefined between the E and H planes for the leaky-wave antenna was shown as Fig. 4.6 by the coordinate of Fig. 4.8.
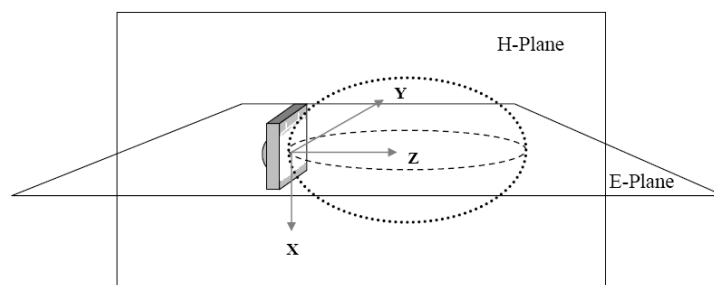
Fig. 4.8 The relationship between the E and H planes for the leaky-wave antenna

To satisfy system requirements, the number of antenna elements was set to 8 and antenna length was set to 15 cm based on data (Tables 4.1 and 4.2). To validate the array design, full-wave electromagnetic simulations were performed using the commercial software Zeland^{TM} IE3D. The optimal design of one element of the leaky-wave antenna followed the data of Table 4.2. Simulation results indicate that the efficiency and antenna gain of the antenna array at 10.5GHz were 80% and 18.4dB, respectively.

4.3 The Measurement Result of Leaky-wave Antenna Arrays

The antenna pattern measurement of the leaky-wave antenna array was performed in the far-field antenna laboratory (is belonged to prof. Yu-De Lin) of department of Communication Engineering, National Chio-Tung University. The test frequencies of the antenna arrays pattern measurement are 9.7GHz,

10.4GHz, 10.5GHz, 10.6GHz, and 11.0GHz. The antenna pattern measurement includes E-plane Co-polarization measurement, E-plane Cross-polarization measurement, and H-plane Co-polarization measurement. The leaky-wave antenna array was realized by the printed circuit boards (PCB) process. Figure 4.9 displayed the photograph of the leaky-wave antenna array.

Fig. 4.9 The photo of the leaky-wave antenna array

The co-polarization represented that the observed signature when the transmitted and received polarizations are the same. The setup of the E-plane co-polarization measurement was shown in Fig. 4.10. The right side of Fig. 4.10 was a measured antenna array and the left side of Fig. 4.10 was a standard horn. The standard horn was a transmitted antenna and the leaky-wave antenna array was received antenna. The polarizations of two antennas are the same. The antenna pattern measurement was shown in Fig.4.11.
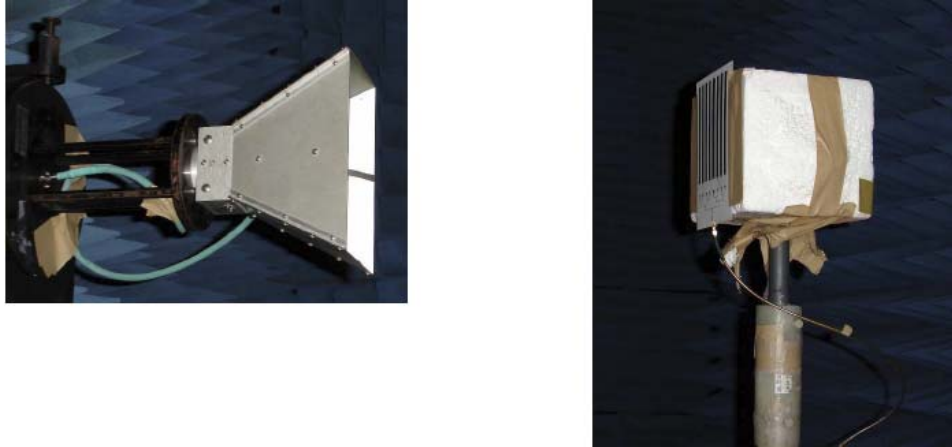
Fig. 4.10 Setup of pattern measurement for E-plane co-polarization
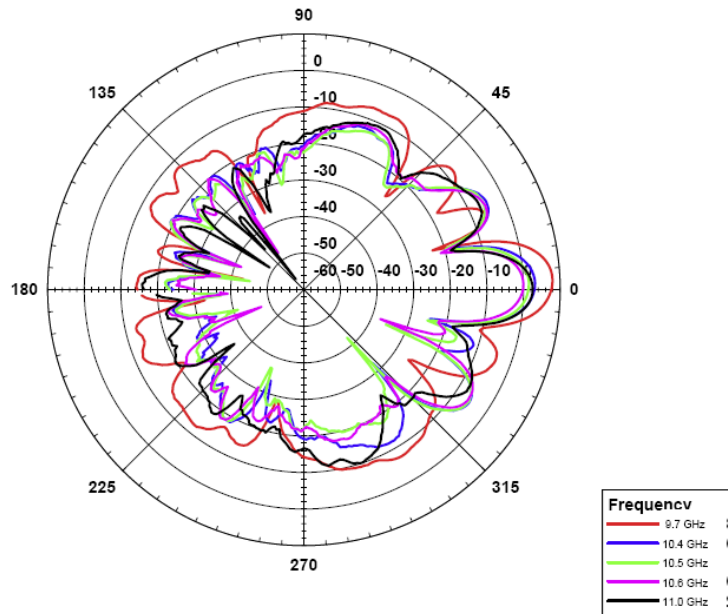
Fig. 4.11 The pattern of E-plane co-polarization of the leaky-wave antenna array

The cross-polarization represented that the observed signature when the transmitted and received polarizations are orthogonal. The setup of the E-plane cross-polarization measurement was shown in Fig. 4.12. The antenna pattern measurement of the E-plane cross-polarization was shown in Fig.4.13. The E-plane pattern was also an azimuth direction pattern.
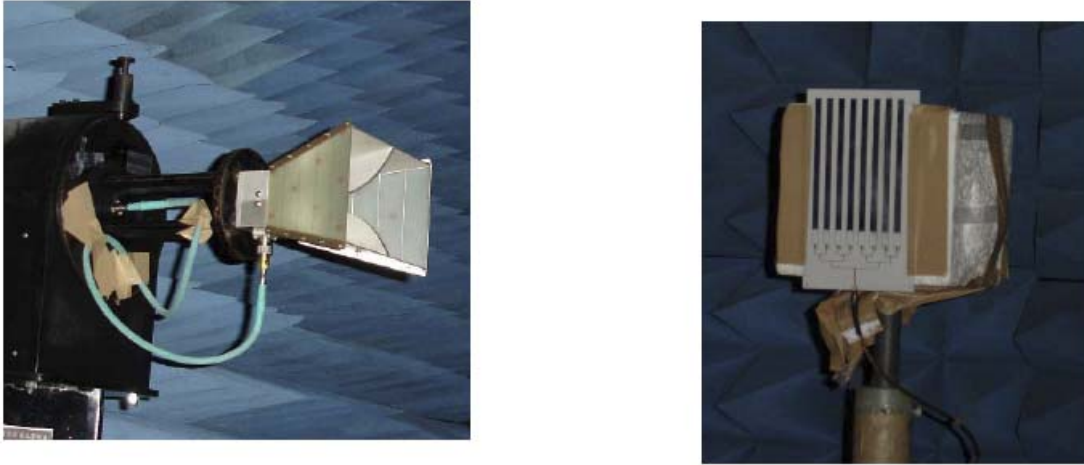
Fig. 4.12 Setup of pattern measurement for E-plane cross-polarization
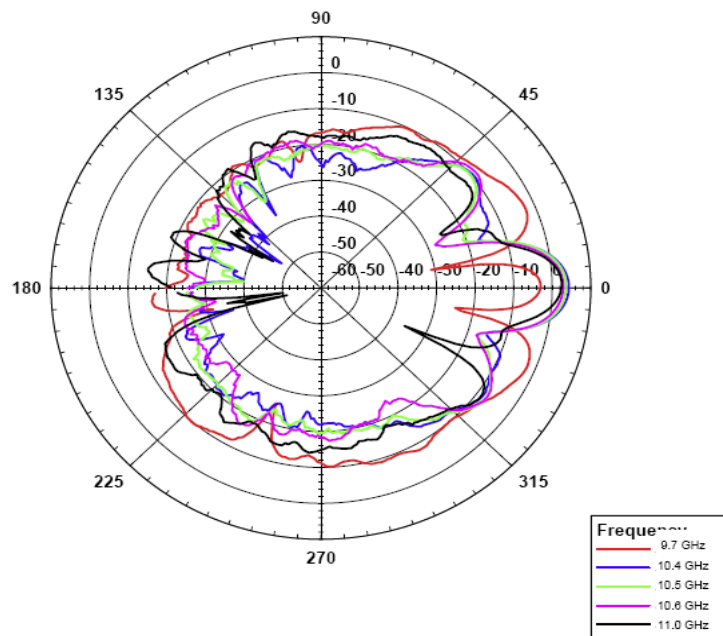
Fig. 4.13 The pattern of E-plane cross-polarization of the leaky-wave antenna array

The setup of the H-plane co-polarization measurement was shown in Fig. 4.14. The H-plane pattern was also an elevation direction pattern. The antenna pattern measurement of the H-plane co-polarization was shown in Fig. 4.15.
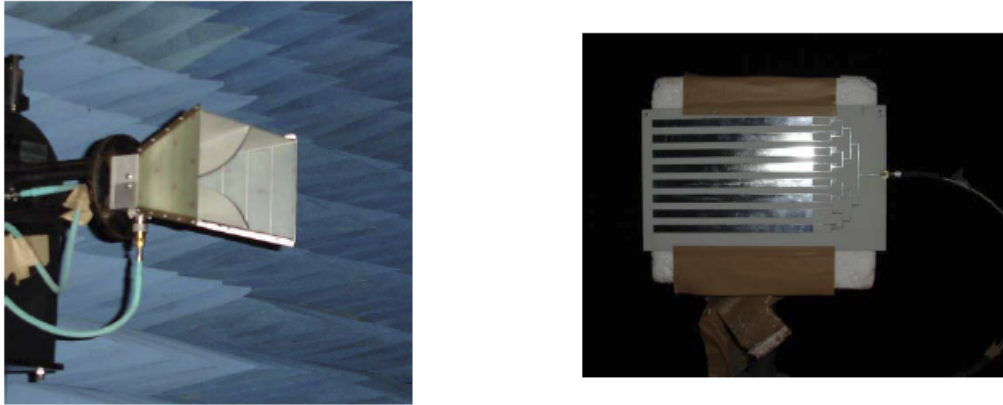
Fig. 4.14 Setup of pattern measurement for H-plane co-polarization
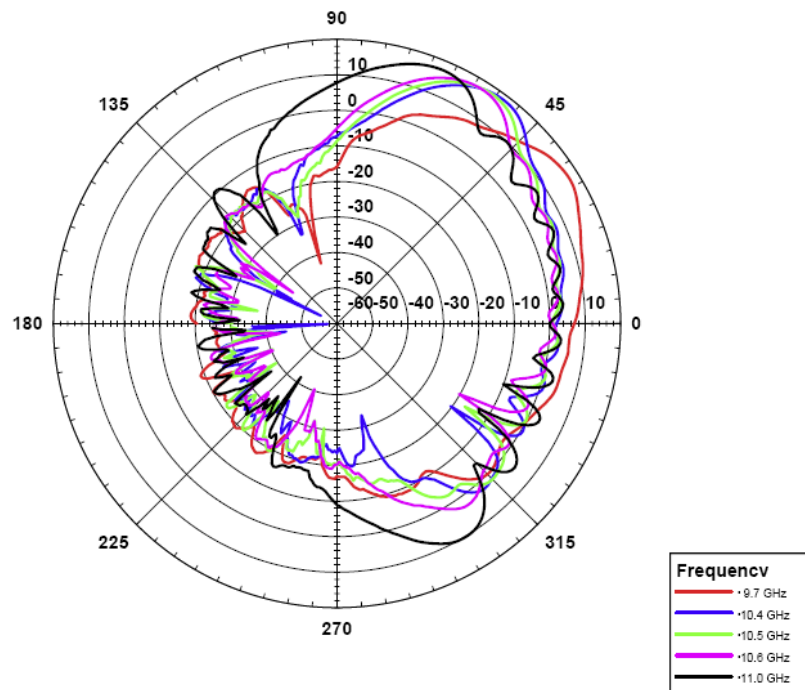
Fig. 4.15 The pattern of H-plane co-polarization of the leaky-wave antenna array

Since the pattern energy of H-plane cross-polarization of the leaky-wave antenna array was very low, which resulted in the measurement was omitted. After the antenna pattern measurement, other important measurements are return loss and coupling efficiency measurement for the 8 stubs leaky-wave antenna array.

There are two leaky-wave antenna arrays in the measurement. The antenna arrays were labeled as A and B. The isolation measurement was adjusted the spacing of the two individual leaky-wave antenna arrays from the most left metal stripe of the antenna array B to the most right metal stripe of the antenna A (Fig. 4.16).
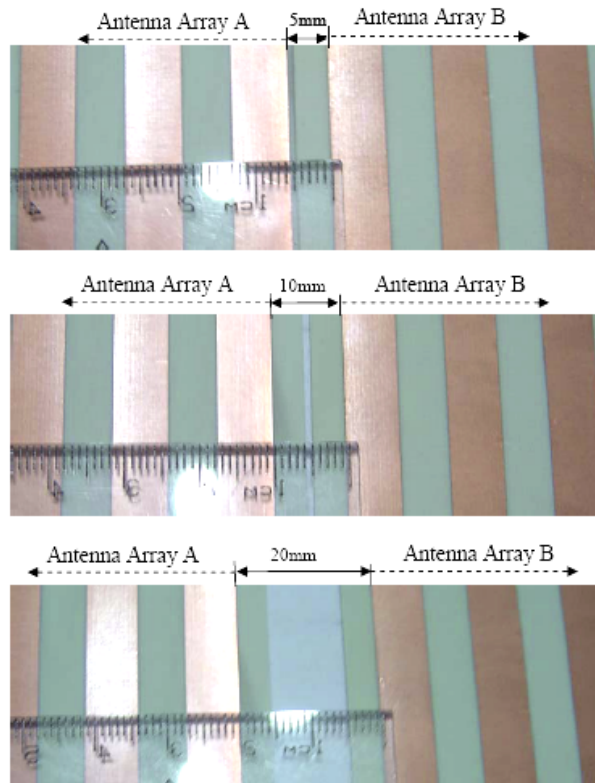
Fig. 4.16 The isolation measurement was adjusted the spacing of the two individual leaky-wave antenna arrays.

Fig.4.17 and Fig.4.18 represented the return loss measurement (from 1GHz to 20 GHz) for Antenna A and B. Since our system used the two antennas to isolate the coupling influence, we tuned the space between two antennas and measured the insertion loss (S21) for two antennas. Figs. 4.19-4.23 represented the coupling measurement for antenna arrays A & B Spacing from 0cm to 8cm. The instrument of the return loss and coupling measurement is Agilent 8510C, before the measured procedure we execute the full ports calibration.

freq=9.740GHz
dB(S(1,1))=-27.543

freq=10.31GHz
dB(S(1,1))=-23.020

freq=10.50GHz
dB(S(1,1))=-16.179
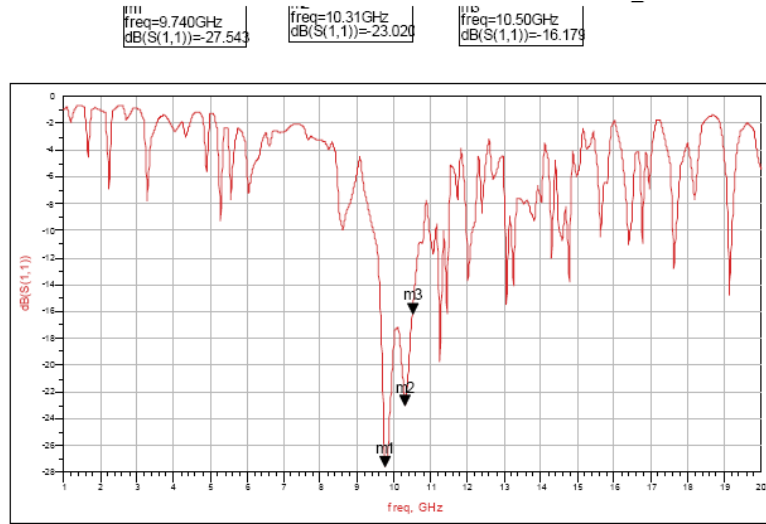
Fig.4.17 Return loss measurement for the antenna array A

m1
freq=9.749GHz
dB(S(2,2))=-25.456

m2
freq=10.22GHz
dB(S(2,2))=-18.819

m3
freq=10.50GHz
dB(S(2,2))=-13.697
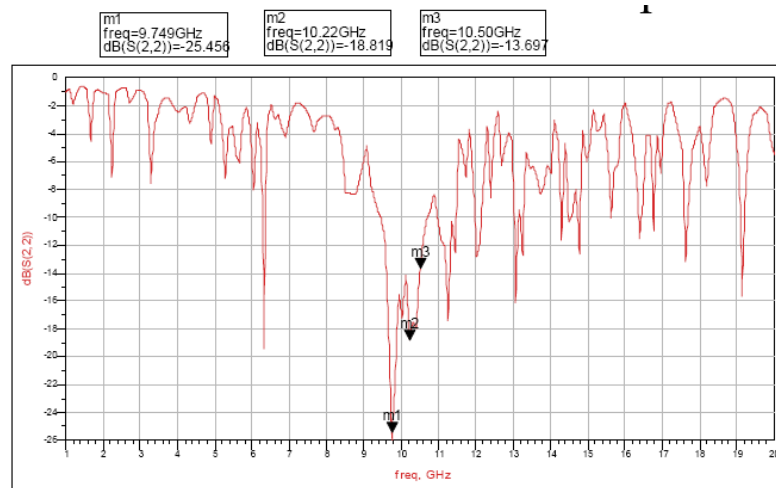
Fig.4.18 Return loss measurement for the antenna array B
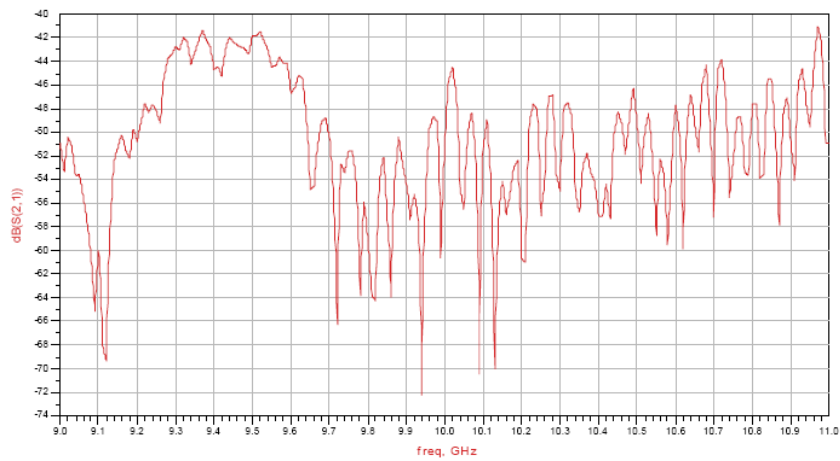
Fig.4.19 Coupling measurement for antenna arrays A & B Spacing 0 cm
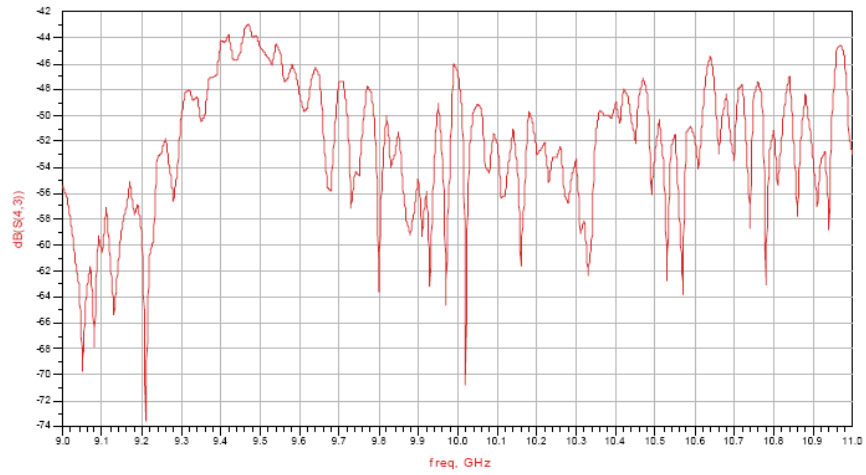
Fig.4.20 Coupling measurement for antenna arrays A & B Spacing 2 cm
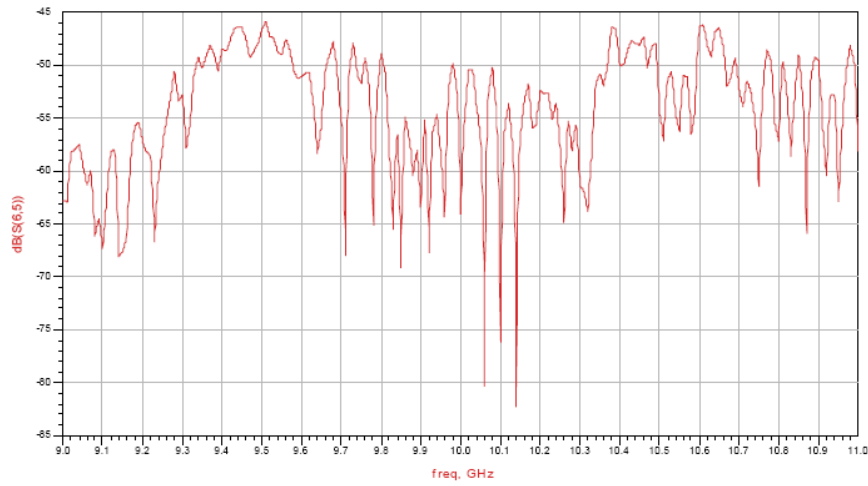
Fig.4.21 Coupling measurement for antenna arrays A & B Spacing 4 cm
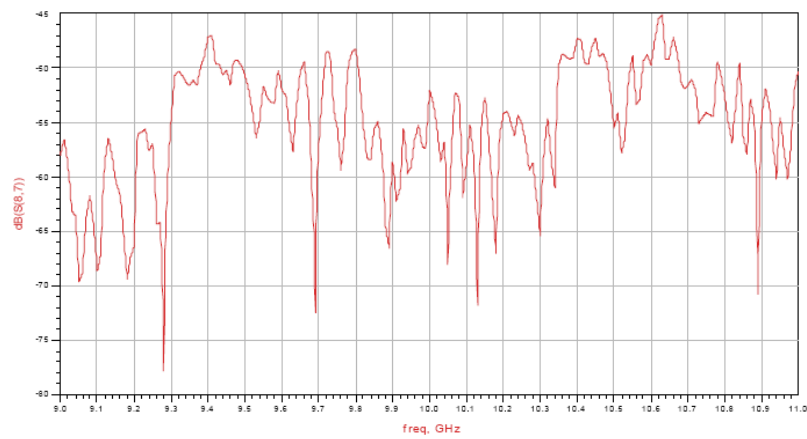
Fig.4.22 Coupling measurement for antenna arrays A & B Spacing 6 cm
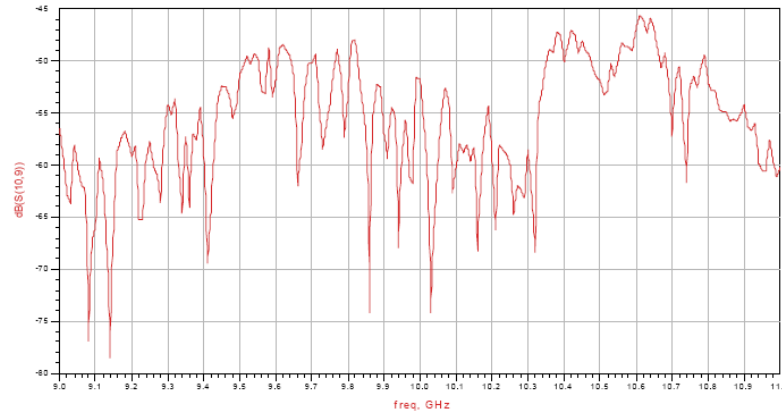
Fig.4.23 Coupling measurement for antenna arrays A & B Spacing 8 cm

It summarized the above measurements that the conclusions were derived the following description: the space of two antennas which increase over 4 cm, the insertion loss (S21) will be dropped to –48dB. And then the insertion loss (S21) of the space of two antennas is also represented the coupling effect of two antennas. Hence, the space of the leaky-wave antenna array is wider than one wavelength, and then the coupling effect can be neglected.

More significantly, the electromagnetic coupling of the two antenna arrays must be measured before combining the entire sensor system. Figure 4.24 plots the measured isolation of the two antenna arrays separated by only 5.0mm, revealing a coupling of less than 42dB. Table 4.3 shows the measured coupling versus the spacing between two antenna arrays, revealing that the coupling is insensitive to the spacing. Significantly, an attainable isolation value for a good circulator in the X-band is around 35dB, which is approximately 10dB below that obtained by the proposed two-antenna array approach. Figures 4.25 and 4.26 show the measured cut-plane on the main beam at 56° from the E-plane (*yz* plane) and the H-plane (*xz* plane) radiation patterns of the leaky-wave antenna array at 10.5GHz. The measurements in Fig. 4.24 demonstrate that the half power is about 15 dB and is bounded between -6.5° and +6.5°. Hence, the 3dB

beam-width of the antenna array was 13° in the E-plane, and that of the main-beam with a gain of 18.5dB was 56° from the broad side of the array in the H-plane. The first lobes of the E-plane radiation pattern were equal to 3.2 dB, because of the original design of the leaky-wave antenna. Since the path lengths of the differential feeding structure of the leaky-wave antenna were not equal, the side-lobes were not symmetrical. Nevertheless, the main direction of the beam is still 0° in the E-plane. In the paper, it applied the elevation pattern (H-plane) to achieve the range measurement. The azimuth resolution (E-plane) haven't discussed in the dissertation. The radiation angle of the elevation pattern has no relation with range resolution. However, the radiation angle effects directly the echo power distribution and the signal-to-noise rate (SNR) of range measurement.

The FMCW front-end, which includes the CMOS transceiver and antenna arrays, was designed and experimentally characterized. The next section presents a practical example of obtaining the vehicle occupancy in TMS to indicate the capability of the proposed FMCW sensor system.
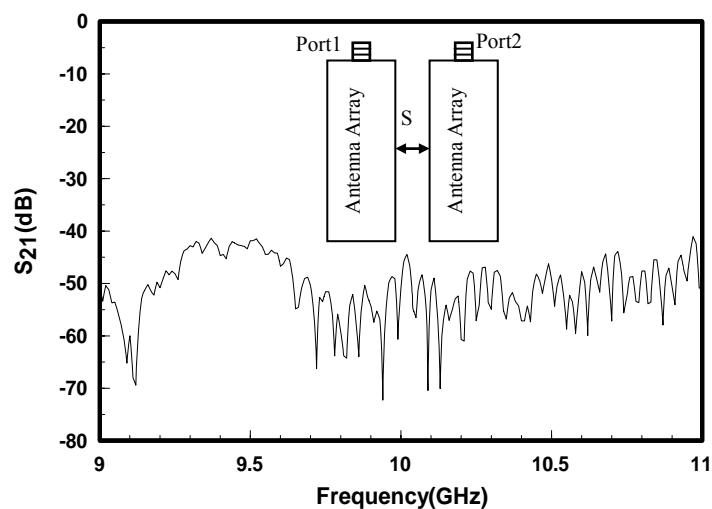
Fig. 4.24 Electromagnetic coupling of the two antenna arrays with a spacing of 5.0mm.

TABLE 4.3 Coupling of Two Antenna Arrays in Different Spacing

S(cm)	0.5	2.0	4.0	6.0	8.0
S_{21} (dB) @ 10.5GHz	–42	–43	–46	–45.5	–45.7
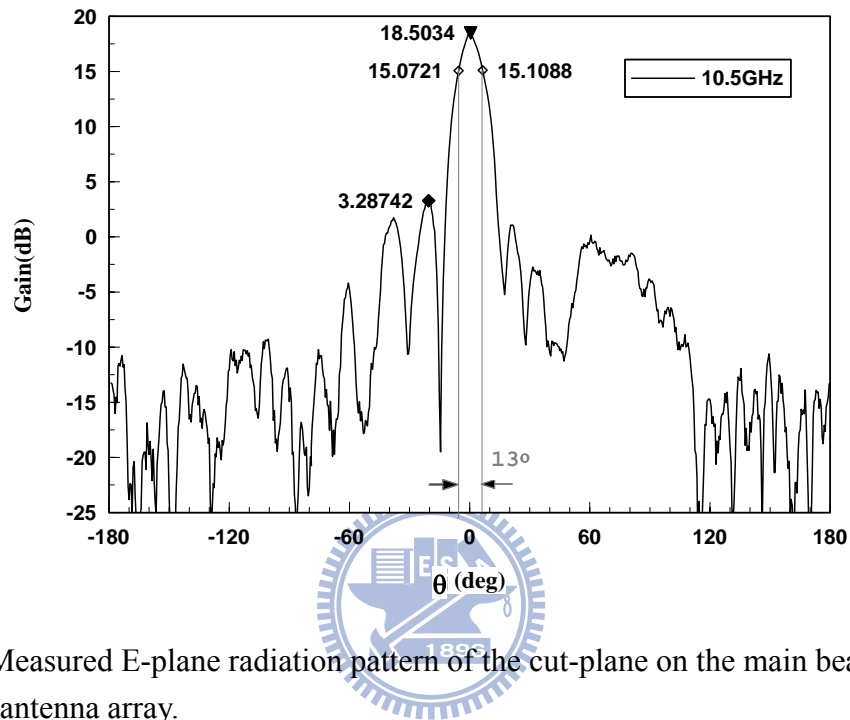
Fig. 4.25 Measured E-plane radiation pattern of the cut-plane on the main beam at 56° of the 8-element antenna array.
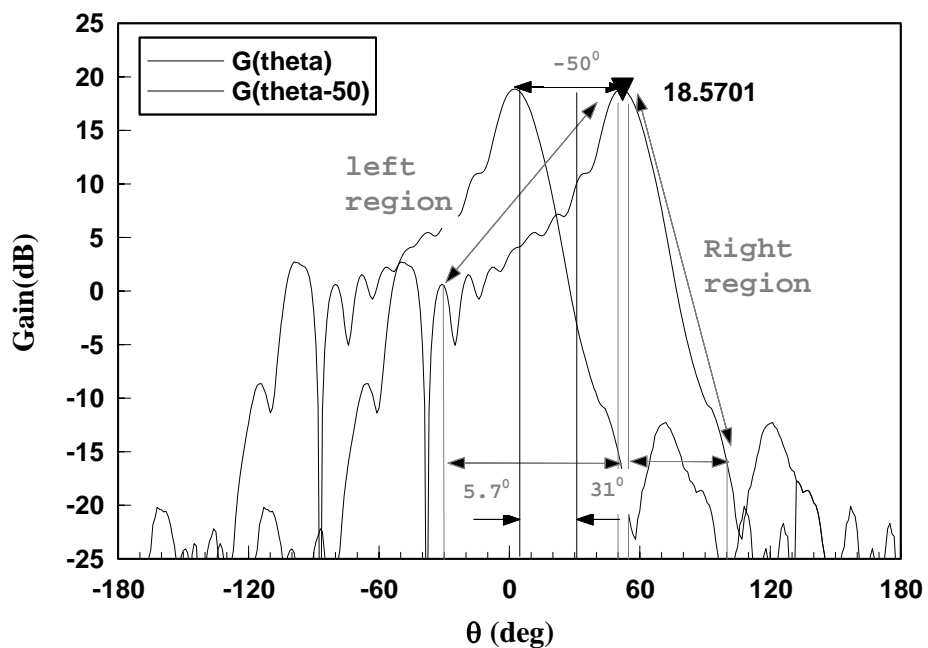
Fig. 4.26 Measured H-plane radiation pattern of the eight-element antenna array.

The csc^{2}θ-type antenna pattern in system applications, originated with the surveillance radar with a fan-shaped beam. The azimuth (E-plane) beam angle is small, and the elevation (H-plane) beam angle is large [20]. The main lobe pattern of the H-Plane of the leaky-wave antenna is always at an oblique angle. The oblique angle is then increased as the length of the antenna array. When the oblique angle was adjusted to a suitable value, the conditional cosecant-squared antenna pattern was realized. The characteristic curve of the cosecant-squared antenna pattern ranges between the two dashed-lines in Fig. 4 of another investigation [42]. The theory of the csc^{2}θ pattern of a leaky-wave antenna has also been derived and proved elsewhere [42]. In the investigation, one element of the leaky-wave antenna is used to design a csc^{2}θ pattern associated with the proposed method that the length of the antenna metal must be varied gradually to prove the design concept with reference to the numerical solution. When the lengths of the metallic antenna are larger than 80.0mm, the csc^{2}θ patterns are obtained (Fig. 4.27).
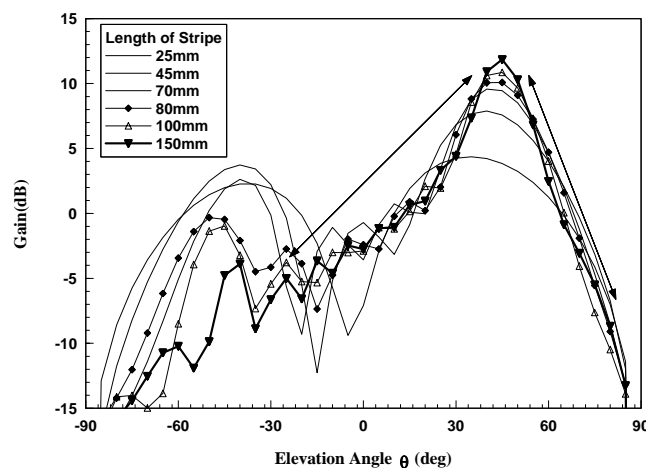
Fig. 4.27 Patterns of elevation angles vary with the stripe length of antenna from 25.0 to 150.0mm.

Figure 4.27 illustrated that when the strip line of the antenna array is longer, the property of the csc^{2}θ pattern is more significant. If the strip line of

the antenna array is shorter, then the radiated energy cannot be immediately leaked to the space and the most of the energy was reflected the other end of the antenna array, that is, when the strip line of the antenna array is less than 80.0mm, resulting in the energy peak appears in the left side of Fig. 4.27.

We made a comparison with one antenna system in NCTU, our two antennas system had higher isolation (-45dB) than the mono-static system (-35dB of a circulator) and can add the external amplifier flexibly. Another important reason is the circulator designed by the CMOS technology did not provide enough isolation between the transmitting and receiving paths. In the paper, the power spectrum of the receiving path was 55dB less than that of the transmitting path at 10.5GHz. These measured results confirm that the proposed system obtained high leakage suppressions by using the CCS TL guiding structure throughout the entire chip design. However, two antennas system need more space to put the antennas. The radiation angle of the elevation pattern has no relation with the range resolution. But the radiation angle affects directly the echo power distribution and the signal-to-noise rate (SNR) of range measurement.

4.4 Integrating the Antenna Arrays and the CMOS Transceiver into a Mechanical Fixture

The mechanical fixture of first version FMCW sensor will be designed for integrating with the antenna arrays and CMOS transceiver. The fixture was used for an experiment of the range measurement. The structure of this fixture includes a hollow box with the CMOS transceiver and accessory circuits are placed into and the antenna arrays are put on, a rotated holder with the hollow box is held and rotated, and the base of a fixture. The mechanical drawing was illustrated in Fig. 4.28 the fixture photograph was demonstrated in Fig. 4.29, and the hardware integration of the FMCW sensor system was also shown in Fig. 4.30.
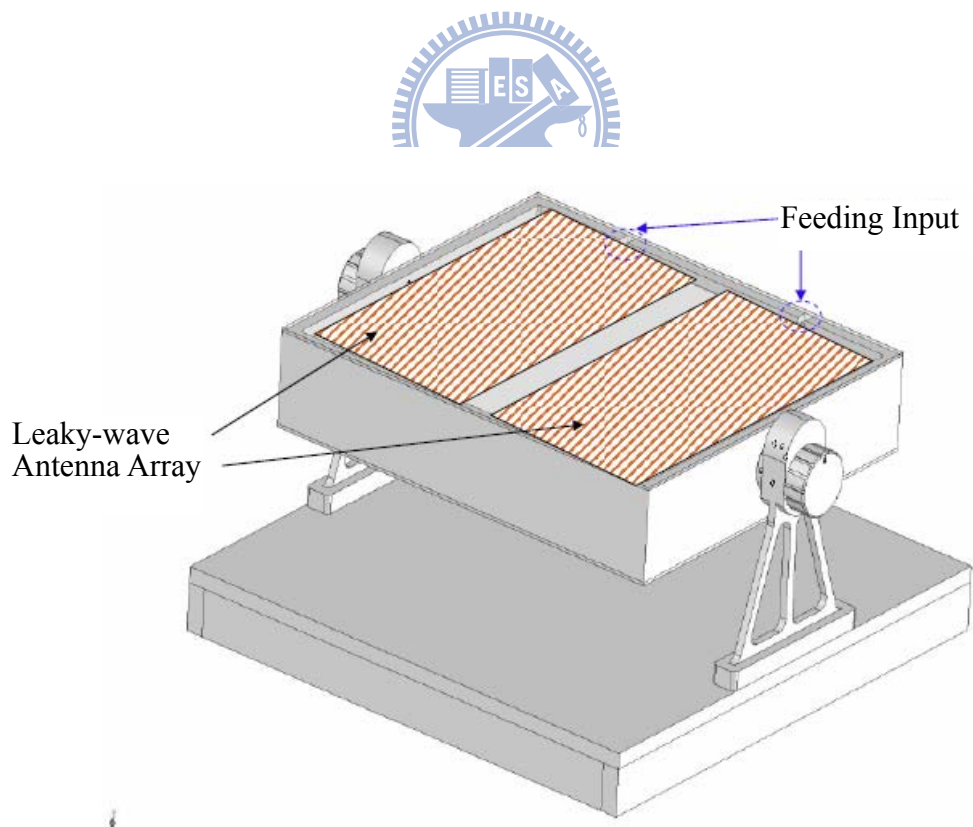
Fig. 4.28 Mechanical drawing of the fixture with a CMOS transceiver and antenna arrays
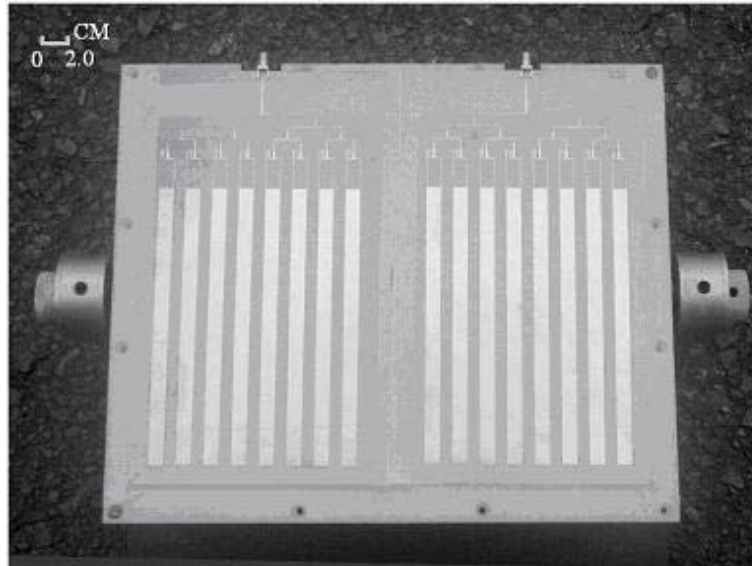
Fig. 4.29 Photograph of the leaky-wave antenna array system.
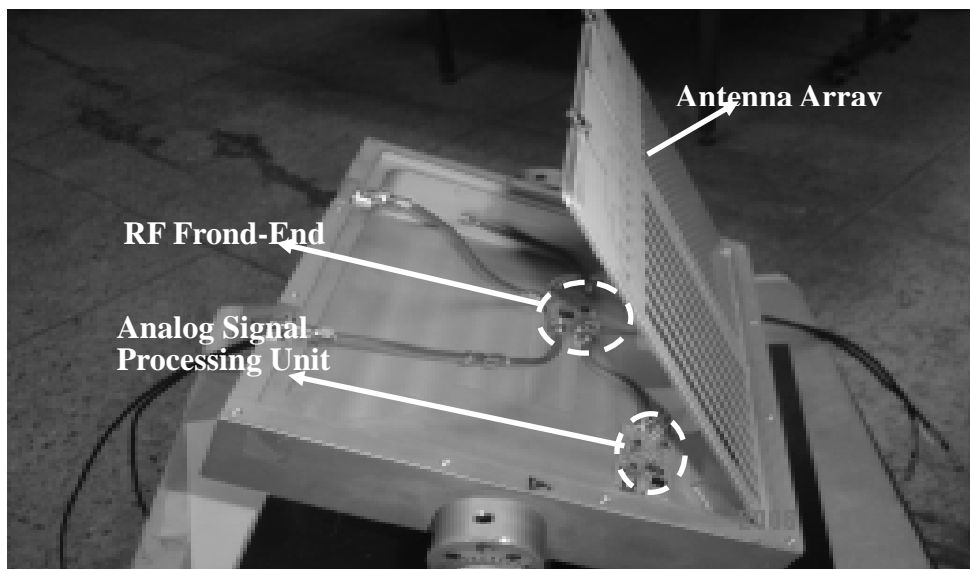
Fig. 4.30 Hardware integration of the FMCW sensor system.

Figure 4.30 show that the signal processor was followed the RF transceiver is analog circuits.

The building blocks of the new version FMCW sensor system shown in Fig. 4.31, which has an RF transceiver, a digital signal processing unit and two antenna arrays, were integrated within a metallic enclosure prior to experiments

were performed. The width, length and height of the enclosure were 20cm, 22cm and 12cm, respectively (Fig. 4.32). Two antenna arrays were installed on top of the enclosure, and covered by a radome, which is 2.0mm-thick a Teflon sheet.
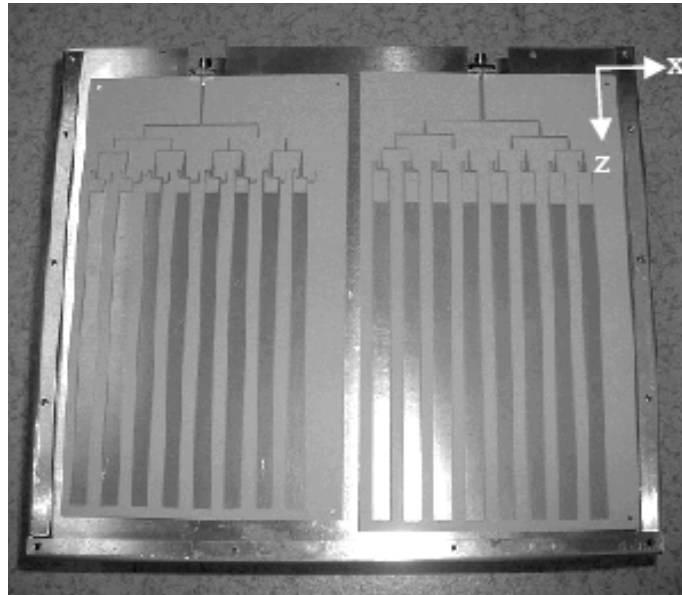
Fig.4.31 Prototype of the leaky-mode antenna arrays.
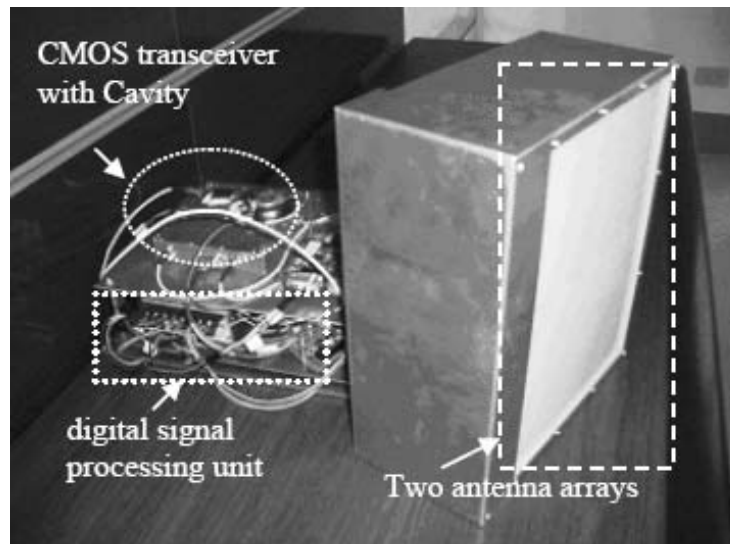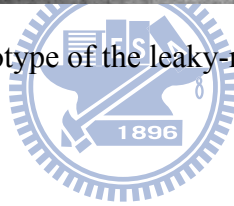
Fig. 4.32 Mechanical installation of the FMCW sensor for TMS.

CHAPTER 5

Design of the Accessory Circuits: the External IF Circuits and

Digital Signal Processing Unit

The major contribution of the paper is to integrate a 0.18μm CMOS transceiver and antenna arrays into a FMCW RF-frond, then adopt a triangle-wave generator, an IF amplifier and a digital signal processor to prove the nearly uniform SNR concept. Hence, the paper focuses on the design and integration of RF system. However, the function blocks and response figures of the external IF and DSP modules are provided an additional remark. The main structure of external IF circuits include a linear modulated circuit and an IF active filter and those circuits were built by the operational amplifiers (OPA).

At FMCW system, the exception of the linearity of the voltage-controlled oscillator (VCO) in chapter 3 is a key point, and then the circuit design of modulation in the chapter is also important. The modulated circuit includes a triangle-wave generator, a telemetric control circuit, and a synchronous signal generator (Fig. 5.1). The most important circuit is the triangle-wave generator that was transferred from the integral squared-wave generator. The operating frequency of the triangle-wave generator was controlled by the capacitor C1, the amplitude was adjusted by the proportion of resistors R1 and R2 (the main adjustment of R2), and the DC bias was varied by resistor R3. By modulating of the VCO, the bias level of the triangle-wave generator set the center frequency of FMCW system, the amplitude of the triangle-wave generator decided the frequency span (bandwidth) of FMCW system, and the period of the triangle-wave generator also control the frequency resolution of FMCW system.

Another important parameter is the slope of the triangular waveform that also determined the linearity of the FMCW system, and next key factors is the good symmetry of this isosceles triangle waveform that avoided the error message of Doppler shift. Hence, a constant slope and a good symmetry of the triangular waveform are the preliminaries of a linear modulation for the FMCW system and then the system can achieve the function of the range measurement.

Fig. 5.1 Frequency modulated circuits includes a triangle-wave generator, a telemetric control circuit, and a synchronous signal generator

Figure 5.2 shown the time-domain response of the triangle-wave generator involve that the triangular waveform and the squared waveform were excited by the frequency modulated circuit in Fig. 5.1. Especially, the telemetric signal was triggered by the digital signal processor or other circuits, and then the action would turn off the triangular and squared signals. In other words, the duration of the telemetric signal was excited and then the frequency modulated continuous wave system was converted into the pure continuous wave system. The primary function of the telemetry is used to suppress the interference from another source with same radio frequency.

Fig. 5.2 Time-domain response of the triangle-wave generator in frequency modulated system.

The next circuit of the external IF circuit is IF active filter. The filter used to define the scope of the beat frequencies, that is, it also set the measurement range of the radar. The RF circuit simulation was illustrated at chapter 3, the IF output power of the mixer in the transceiver was about −125 dBm. The output impedance of IF port of the mixer is 50 Ω, it bases on this reference impedance to estimate the minimum output voltage is nearly 5 mV. Therefore, the exciting level of the IF active filter input will be set to 1 mV. In the chapter 3 of the thesis, the measured distance of FMCW sensor was defined from 5 meters to 30 meters. If the frequency of triangular wave is set to 1.42 KHz, then the corresponding frequency resolution is 2.84 kHz. The range resolution is 1 meter in accord with the RF bandwidth of 150 MHz. The beat frequency of 5 meters is 2.84 KHz × 5 = 14.2 KHz and of 30 meters is 2.84 KHz × 30 = 85.2 KHz. Hence, the bandwidth of the IF active filter is from 14.2 KHz to 85.2 KHz by initial estimation. If the 3-dB bandwidth is an actual specification and the input level of the analog-to-digital converter is less than 3 V, then the modified bandwidth of the IF active filter is from 12 KHz to 100 KHz and gain is about 68.7 dB. Ultimately, the schematic of the IF active filter was shown in (a) of Fig. 5.3 and the frequency response was also displayed in (b) of Fig. 5.3.
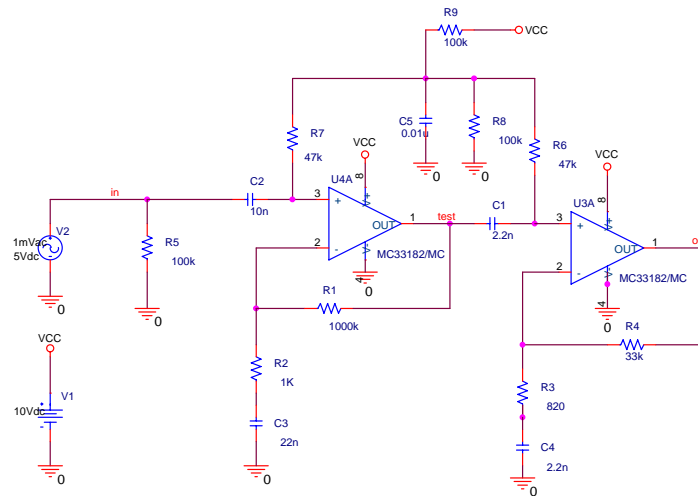
(a)
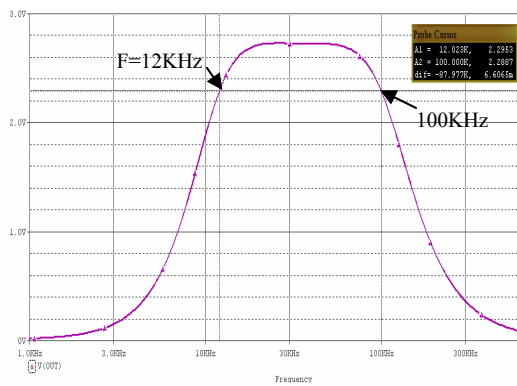
(b)

Fig. 5.3(a) schematic of external IF active filter, (b) the frequency response of external IF active filter.

Figure 5.4 displays the architecture of the digital signal processing unit of the proposed FMCW radar. The operational principle of the FMCW radar for detecting the distance from the output signal of the digital signal processor can be mathematically described as in the previous paragraph.
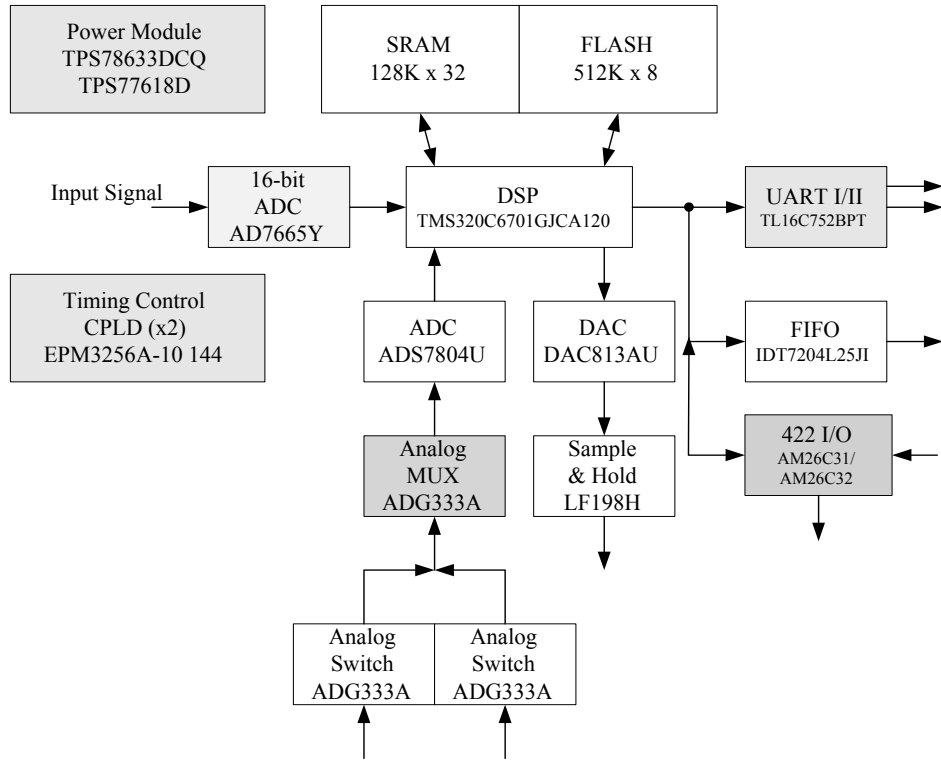
Fig.5.4 Block diagram of the digital signal processing unit.

The flowchart of fast-Fourier transformation and the target discrimination of the digital signal processing were shown in Fig. 5.5.
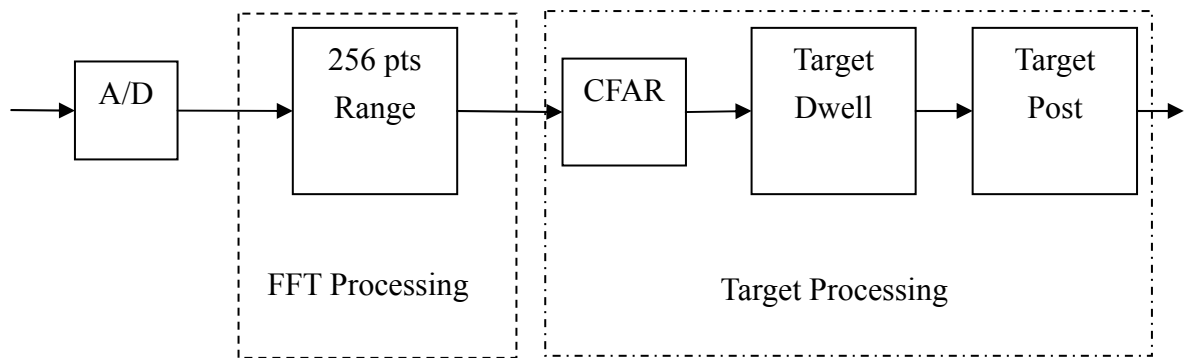
Fig.5.5 Flowchart of the digital signal processing unit.

Since the IF amplifier and the digital signal processor (TMS320C6701) is accessory circuits in the paper and these circuits assist to prove the performance of CMOS transceiver. The CMOS transceiver also integrates with antenna arrays, an IF circuit, and a DSP circuit to realize the FMCW system. If size and

cost of the DSP will be miniaturized and cost-down, then can choose the DSP of Microchip^{TM} or realize an ASIC chip.
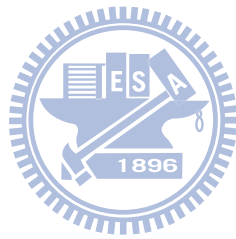
CHAPTER 6

Measurement and Verification of the FMCW System

6.1 Measurement of the First-version FMCW Radar

Figure 4.29 shows the fixture for the revolving spindle that facilitates accurate positioning the main beam of an antenna array to a desired target. The leaky-mode antenna arrays were purposely lifted to expose the RF module and analog signal-processing unit installed on the backside of antenna arrays. Figure 3.1 shows the proposed sensor system, which can detect distance and velocity of objects simultaneously. In the following section, experimental results, including those for detecting distance and velocity, demonstrate the capability the FMCW sensor.

6.1.1 Distance Measurement

The initial design employs the triangular waveform as a modulation source, and so has various applications. If the modulation source were a sawtooth waveform, then information about the speed would be lost. In other word, there is no Doppler shift in the range measurement. Since the original paper, the FMCW sensor is also designed for the speed measurement. To simplify the thesis and because of the special purpose to which is applied, the measurement of speed is omitted. In the paper, the sensors were located in the roadside are set up vertically to the multiple-lines, since the vertical direction to the target results in a zero-frequency Doppler shift whether the vehicle is moving or stationary.

The photograph of the field test (Fig. 6.1(a)) presents the setup for detecting distance between an object and sensor. A small moving vehicle carrying an

aluminum plate 80 cm×60 cm in size is applied as a reflective object for static detection of target distance. Given the parameters of ΔF =50 MHz, F_m= 100 KHz, the output spectrum of the IF-ABPF is shifted from 100 KHz to high frequency for each increase in stepping distance of 3 m. During measurements for distance detection, echo signal power spectra were monitored continuously. Part (b) in Fig. 6.1 presents the measured spectrum at the mixer output for a target 25.8 meter from the sensor. No reflected signals were observed near 200.0–400.0 KHz (Fig. 6.1(b)), indicating that isolation inside the CMOS transceiver chip and isolation between two antenna arrays are attained. Additionally, the measured distances are calculated by (2-1) with the sensor parameters already mentioned. Figure 6.2 plots the measured and theoretical beat frequency of the sensor, indicating that the error bound is consistently <3.0 % when the D is increased from 10 to 30 meters.
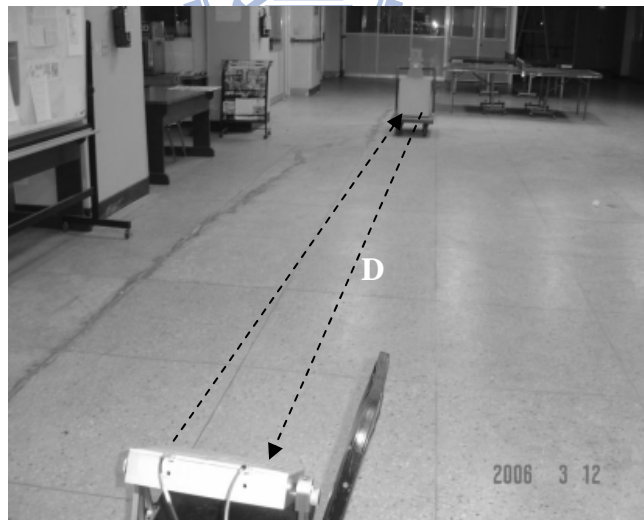
(a)
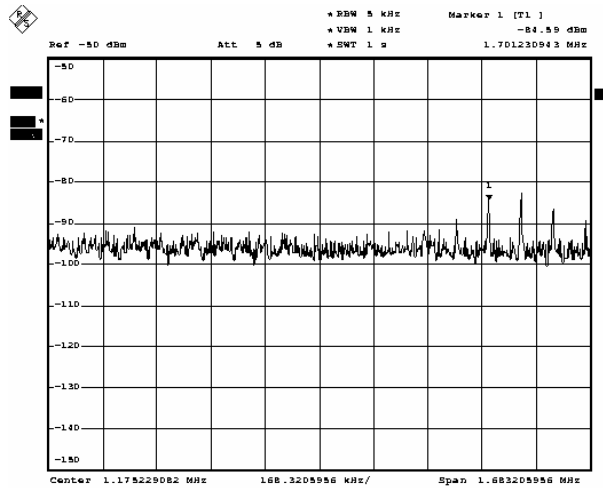
(b)

Fig. 6.1 Distance measurement using the FMCW sensor: (a) field test setup, (b) measured spectrum of the mixer output for a distance of 25.8 meters
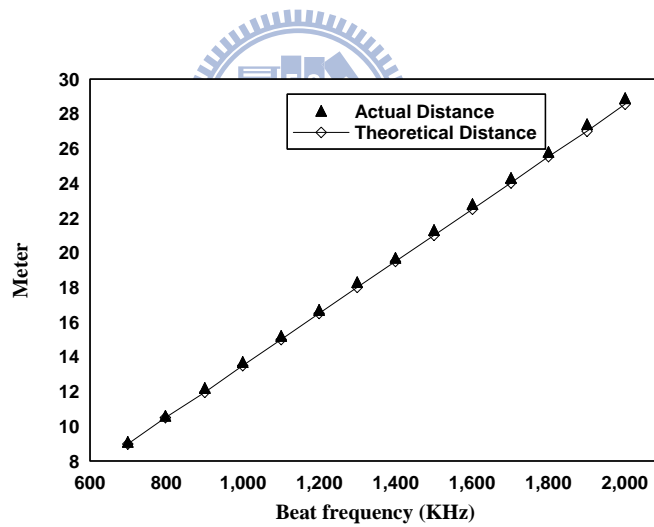
Fig 6.2 Measured and theoretical values of distance vs. beat frequency of the proposed FMCW sensor.

6.1.2 Velocity Measurement

The results of equation $f_d = f_b^- - f_b^+$ indicate that the speed is a down-converted after two beat frequencies are mixed. A traditional FM system accepts demodulated signals using an envelope-detected circuit containing diodes and a low-pass filter. In the work, the analog signal processing circuit also has an envelope-detected circuit that is substituted for a digital signal processing (DSP) unit to measure target speed. The moving target was detected by aiming the antenna at a vehicle traveling at 60 km/hr at an angle (θ) of 30° from the forward direction (Fig. 6.3). Actual speed was read from the automobile speedometer. The beat frequency (f_b) was increased from 100.0 KHz to 1.0 MHz. Such an increase reduces response time of the FMCW radar when detecting moving targets.

Fig.6.3 The outdoor test area for distance and velocity detection

Figures 6.4 (a) and (b) were present measurement results at the output of the envelope detector in frequency and time domains, respectively. When the Doppler frequency shift is estimated at 1.01 KHz, the automobile speed is 59.976 km/hr (Fig. 6.4(b)), as given by Eq. (2-6) in chapter 2:

$$v = \frac{(f_b^- - f_b^+) \times C}{2 \times f_c \times \cos\theta} = \frac{f_d \times C}{2 \times f_c \times \cos\theta} = \frac{1.01 \times 10^3 \times 3 \times 10^8}{2 \times 10.5 \times 10^9 \times \cos(30°)},$$

Therefore, $v = 16.66$ *(m/sec) = 59.976(km/hr)*, validating the receiver chain when processing to echo signals from the target, and yields the performance of the velocity measurement using the proposed FMCW sensor.
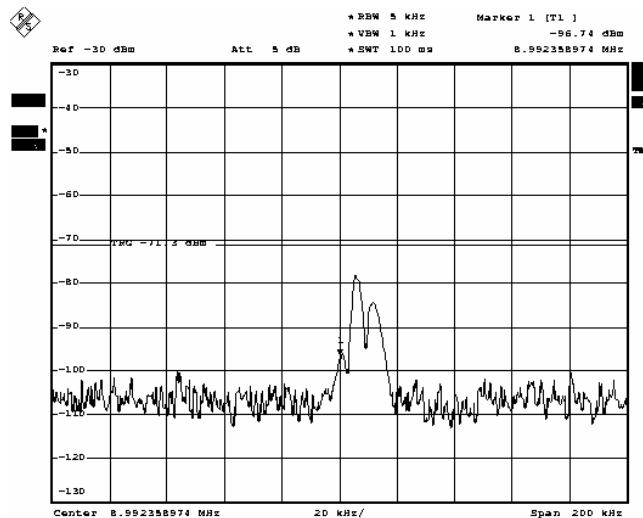
(a)
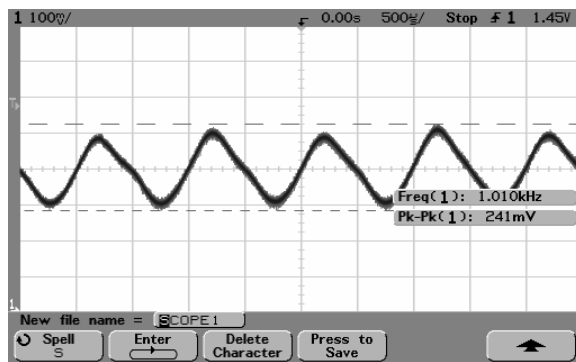
(b)

Fig. 6.4 Velocity detection using the proposed FMCW sensor: (a) input spectrum of the envelope detector; (b) time-domain waveform at the output of the envelope detector

6.1.3 Field Test of the Azimuth Resolution of Antenna Arrays

Since the azimuth resolution (E-plane) haven't discussed in the dissertation. Nevertheless, the experiment is applied the leaky-wave antenna arrays of the paper integrate with the RF transceiver using by Institute of Traffic and Transportation of National Chiao-Tung University to do field test.

Main purpose of the experiment is that estimated the performance of the E-Plane radiation pattern application of leaky-wave antenna arrays for the vehicle classification of the transportation management system. Hence, the comparison of the E-Plane radiation pattern in the actual measurement was made, such as the leaky-wave antenna arrays and the original dual-horn antennas.

The experiment is carried out and tested dynamically in the balcony of second floor of Center of Transportation Studies of National Chiao-Tung University; the product's idea of its experiment is as follows. In antenna parts: First, the dual leaky-wave planar antennas were designed by the Graduate Institute of Communication Engineering of NTU. Second, the pairs of horn antennas were designed by UUEI Engineering INC. In transceiver parts: the design of microwave circuits is only UUEI Engineering INC. In the digital circuit: First, the computer base development of the NI Labview^{TM} signal processing system is designed by Institute of Traffic and Transportation of National Chiao Tung University, second, the development of the DSP Chipset signal processing circuit is developed by UUEI Engineering INC.

Experimental approaches were defined the distance between two lanes and the movement of two cars for measuring the beat frequencies of range measurement without speed and the azimuth resolutions (E-plane) of antenna

arrays.

1) The range measurement was made. If the development of the digital signal processing circuit (TI DSP Chipset) is designed by the UUEI Engineering INC., two types of antennas can be satisfied with the high-quantity signal analysis of the beat frequencies, but the computer base development of NI Labview^{TM} signal processing system is designed by Institute of Traffic and Transportation of National Chiao-Tung University, the lack of signal quantity was occurred in both antennas system. The reason may be due to operating speed of NI DSP or the impact of the time-division multiplexing (TDM) with the computer system.

2) For the azimuth resolutions (E-plane) measurement: the balcony of ground height is ranging over 4.7M and the measured instruments located in the edge of the balcony near the first lane. Then the nearest measuring distance from the body of the car at the first lane to the measured instruments was 6.7M and the body of the car at the second lane to the measured instruments was about 9－10M. The effectively azimuth angles in the scope of two types of antennas such as Fig. 6.5 were detected. The detection range of the leaky-wave antenna arrays is a parallel region in the experiment and the width of the region less than the length of a car, rather than is along the direction of the fan-shaped extension of the dual horn antennas.
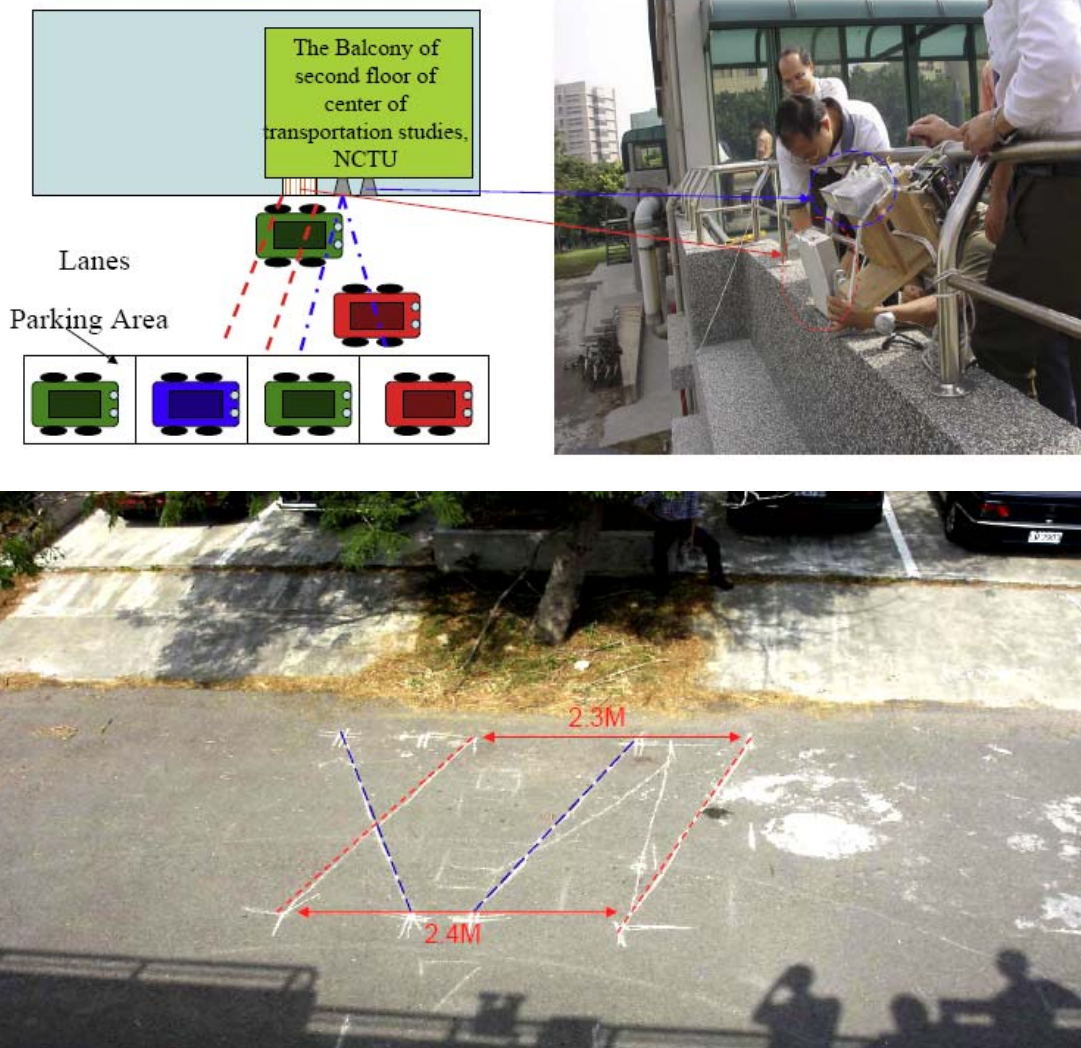
Fig. 6.5 The region was enclosed by the red dotted line is a detected range by the leaky-wave antenna arrays. On the one hand, the region was enclosed by the blue dotted line is by the dual horn antennas.

6.2 Measurement of the New-version FMCW Radar

6.2.1 Signal-to-Noise Ratio of CMOS-Based FMCW Sensor System

The SNR of the proposed FMCW sensor system was characterized theoretically before performing additional measurements. Additionally, the calculated data were confirmed by the experimental results of a field test. Figure 6.6 presents the setup for vehicle detection using the proposed sensor system. The sensor, which is a road-side unit, was installed above the ground at the height h. The vehicle occupancy in multiple lanes was detected by performing a range measurement with the FMCW sensor system. The total width of the multiple-lanes is denoted by D in Fig. 6.6, and represents the maximum coverage of the FMCW sensor. The values of h and D were set to 3.0m and 30m, respectively, in the field test. The building blocks of the FMCW sensor system, which had a CMOS transceiver, a digital signal processing unit and two antenna arrays, were integrated within a metallic enclosure before experiments. The width, length and height of the enclosure were 20cm, 22cm and 12cm, respectively, according to Fig. 4.31. Two antenna arrays were installed on top of the enclosure, and covered by a radome, which is a Teflon sheet with a thickness of 2.0mm. The H-plane of the antenna array was orthogonal to the traffic lane, and slanted at an angle of 35° by mechanical rotation, as indicated in Fig. 6.6. The configuration helped the FMCW sensor to suppress the Doppler effect of the moving vehicle.

The $csc^2\theta$ type radar was constructed from the present antenna array with the H-plane pattern, and the appropriate sensor height and mechanical rotated. The major capability of a $csc^2\theta$ type antenna pattern is performing the multiple-lanes measurement. The antenna pattern thus has a similar function to

the sensitivity time control (STC) of the IF filter, of providing a spatially uniform SNR within the range measurement. The proposed antenna arrays not only realized the nearly spatially uniform SNR to compensate the power level at farther section, but also achieved high isolation, thus suppressing heavy interference in the near field.
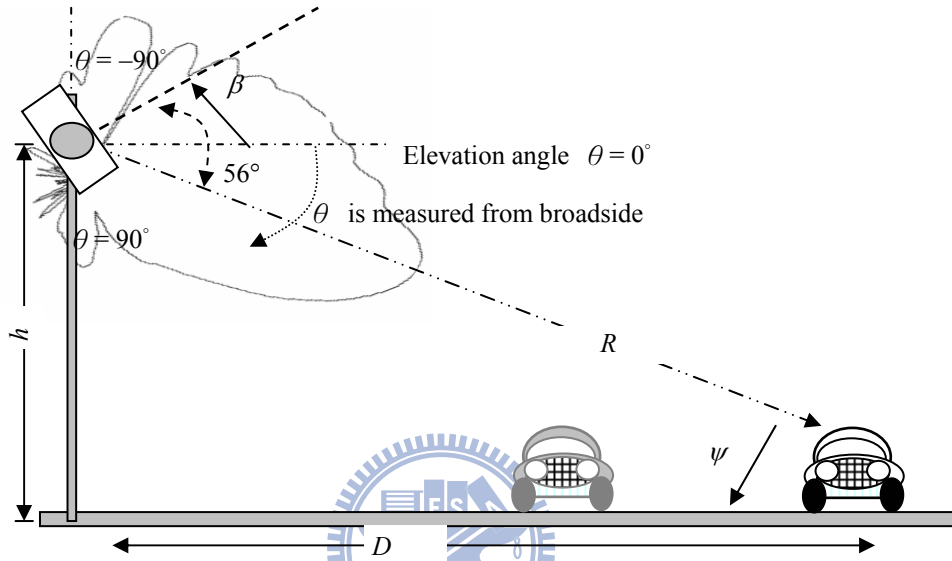
Fig. 6.6 The FMCW sensor adopted the multiple-lane vehicle detection of TMS. The H-plane antenna radiation is orthogonal to the moving vehicle

The power of the electromagnetic waves that propagate between the sensor and the single vehicle was estimated from the range measurement presented in Fig. 6.6 by the following well-documented equation: [49]

$$S = \frac{P_{TX} G_T G_R \lambda^2 \sigma}{(4\pi)^3 R^4} \qquad (6\text{-}1)$$

where S denotes the receiving power at the output of the receiving antenna; P_{TX} represents the transmitting power at the input of the transmitting antenna; G_T and G_R indicate the transmitting and receiving antenna gains, respectively; λ is the wavelength corresponding to the operating frequency; σ denotes the radar

cross section (RCS) of the vehicle at the operating frequency, and R represents the effective distance between the sensor and the vehicle [49].

According to stated electrical characteristics of the proposed CMOS transceiver and antenna arrays in chapter 3 and 4, the operating frequency was 10.5 GHz, and the corresponding wavelength in the air was 2.86cm. Since the H-plane main-beam of an antenna array was aimed at the vehicle by making mechanical adjustments, the antenna gains for both transmitting and receiving paths were calculated from the curves plotted in Fig. 4.25. Additionally, an irregular metallic body was applied as the reflected target with an effective RCS (σ) of about 0dBsm at 10.5 GHz by the user manual and the RCS of the irregular metallic body be equivalent to a spherical object with a radius of 1.0m [49]. The output power of the CMOS FMCW transceiver in Fig. 3.6 was −18.2dBm at 10.5GHz, rising to 0dBm at the input of the transmitting antenna through an external PA. Therefore, the reflecting power of single target at the input of the CMOS transceiver was about −87dBm at D=30m. The conversion gain from LNA input to the mixer output at the IF output port in the receiver path was 0.2dB. The 49dB IF amplifier was found to be adequate for enabling the DSP unit to carry on signal processing in the presented sensor system.

Significantly, the leaky-mode antenna array eliminates the R^4 equalizer, thus compensating for the R^4-dependence of returned signal power. The property is similar to the csc^2 type antenna of the surveillance radar by military application. The most important contribution of this study is to present a sensor system that supports the almost equal to echo power for range measurement of multiple lanes, using the H-plane antenna pattern in Fig. 4.25. The gain factors G_T and G_R in (6-1) can be extended to a cross-section of the H-plane pattern in Fig. 4.25 as

$G_T(\theta)$ and $G_R(\theta)$. The gain of G_{IF} is sum of a mixer and an amplifier was added to radar equation in order to compare the measured data directly. A new radar equation was derived from (6-1) with reference to Fig. 6.6, which shows the antenna arrays.

$$S(h, \beta, \theta) = \frac{P_{TX} G_T(\theta + \beta) G_R(\theta + \beta) \lambda^2 \sigma G_{IF}}{(4\pi)^3 (h \cdot \csc \theta)^4} \tag{6-2}$$

where θ denotes the elevation angle that measured from the broadside; β represents the elevation angle set by mechanical rotation, and $G_T(\theta+\beta)$ and $G_T(\theta+\beta)$ indicate the transmitting and receiving antenna patterns, and are functions of θ and β. Restated, the antenna pattern functions are shifted through an angle of β. The parameter h is the height of the sensor box containing the antenna arrays, the radio frequency module and other circuits. The function $h \cdot \csc \theta$ was substituted for R in (6-1) using the trigonometric relationship in Fig. 6.6. The term R is a function of h and β, and is given by

$$R = \sqrt{h^2 + D^2}, \text{ and } D = R \cdot \cos \theta, \ h = R \cdot \sin \theta,$$

then
$$R = \frac{h}{\sin \theta} = h \cdot \csc \theta \tag{6-3}$$

and
$$D = h \frac{\cos \theta}{\sin \theta} = h \cdot \cot \theta \tag{6-4}$$

Equation (6-3) and new parameters in (6-1) yield the modified radar equation, (6-2). The receiving power S is a function of θ, β and h. Equation (6-2) indicates that the modified radar equation is related to the height of the sensor system and the gain of the all-antenna pattern.

Since the angle of maximum gain of the H-Plane in Fig. 6.6 is 56°, and the H-plane pattern has a special envelope region at about 60°−70°, the echo power decay $1/R^4$ can be compensated. The study presents a simple approach for maintaining a near-constant echo power in the range measurements of the FMCW system, by tuning the angle (β) by mechanical rotation to the envelope region of the antenna pattern, thus projecting it exactly onto the multiple-lanes. Equation (6-2) was employed to estimate the optimal angle of mechanical rotation, yielding a uniform reflected power response for range measurement. In Fig. 6.7(a), the power distribution of the beat frequency was varied, and the mechanically rotated angle was varied from −5° to −55° in steps of 10°. The antenna arrays were 3m above ground. The most uniform power responses were between −45° and −55°. The region of highly uniform power distribution was expanded as in Fig. 6.7(b), where the angular interval was 2°. Accordingly, the envelope curves of the H-plane pattern between −45° and −55° were adopted to measure the distance, compensating for the loss, which is given by the inverse of the fourth power of the distance. However, the near-uniform power response was associated with greater power decay at shorter ranges, as indicated in Figs. 6.7 (a) and (b).   The near-field interference of most transceivers resulted from leakage from the LO port, or coupling of the transmitter and the receiver, which always occurred at the short range.

The shorter range power decay can be cancelled by the near field interference. If a system requires uniform spatial power at the short range, then the height of the sensor can be reduced to meet the requirement.   Figure 6.7 (c) shows the variation of the power distribution of the beat frequency with the height of the sensor from 1m to 5m in steps of 1m, at an angle of mechanical

rotation of 50°. Figure 6.7 (c) reveals that a higher sensor was associated with more power decay at the short range, but a more uniform power response at a longer range. A lower sensor yielded a better power distribution at the short range, but a non-uniform power response at the long range.

(a)

(b)
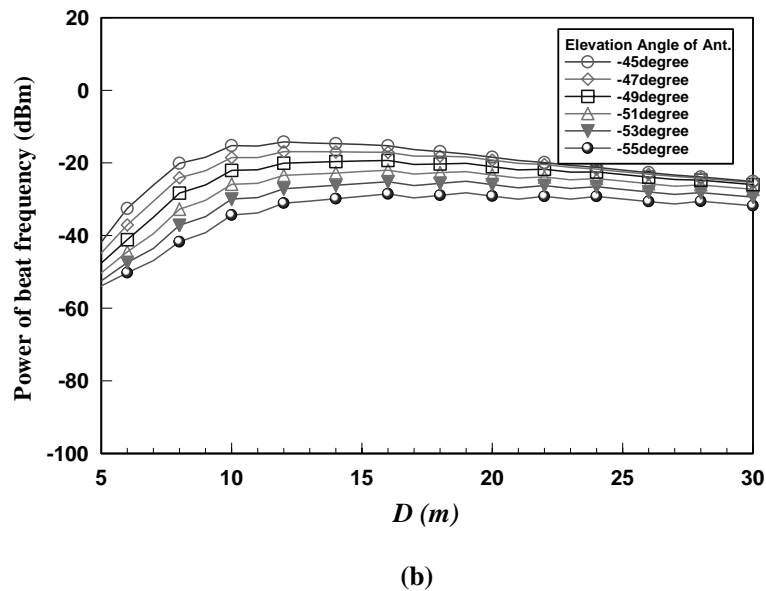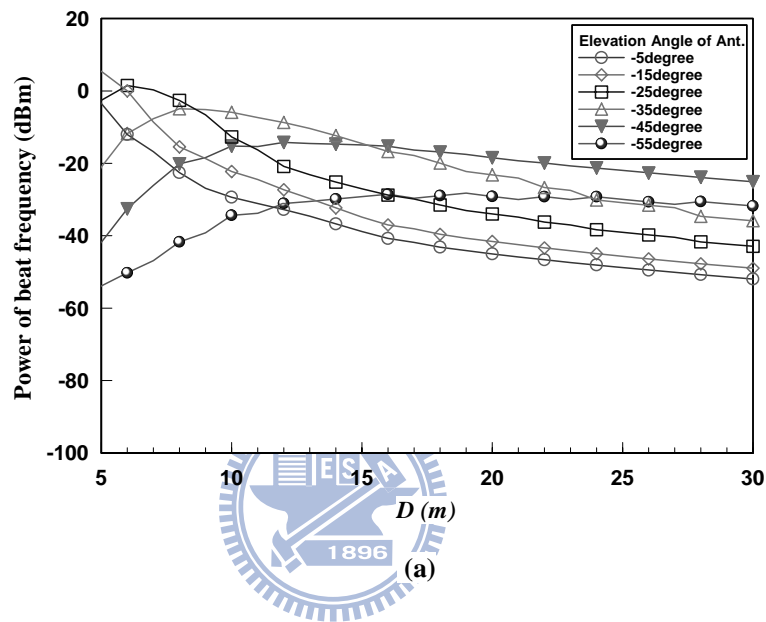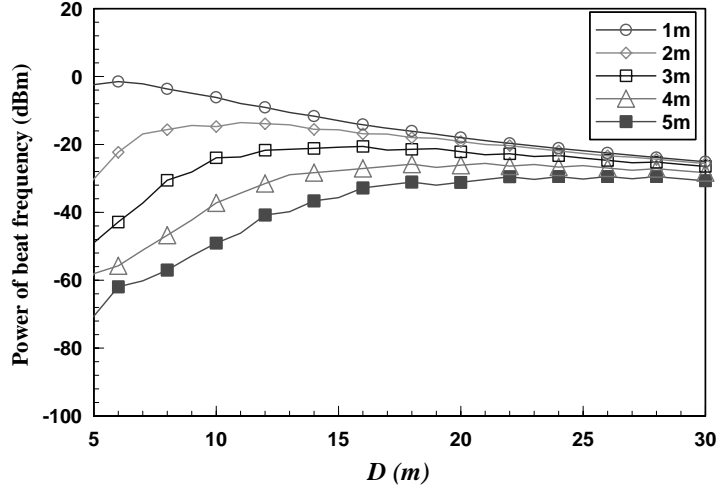
(c)

Fig.6.7 (a) Estimation of echo power distribution with fixed sensor height fixed at 3m, and angles of rotation from −5° to −55°. (b) Magnified figure (a) from −45° to −55°.   (c) Fixed angle −50° and variation of height of sensor from 1m to 5m.

The noise of the completed sensor system of the proposed X-band CMOS chip was characterized by performing time-domain system simulations by a commercial software package, ADS2006A. The system simulations represent the building blocks shown in Fig. 1.1 as behavior models. The parameters of each model were carefully set up based on the measured results of the corresponding device.

Fast-Fourier transformation was performed on system simulation results. The noise value of the CMOS transceiver after FFT was 9.2 dB, which is 0.8dB less than that obtained from the measurements in Table 3.1. Therefore, the noise power of the completed radar system is given by

$$P_N = kTB_d N_F \qquad (6\text{-}5)$$

where k denotes the Bolzmann constant, and T represents the ambient temperature (K) [49]. B_d denotes the bandwidth of the range filter. The temperature was set to room temperature, and B_d=3.9 KHz, which approaches

90

the bandwidth of frequency resolution. The noise figure N_F in the presented CMOS transceiver was 10dB. Therefore, the total noise power of the sensor system was −128dBm.

For convenience of range measurement and uniform spatial power distribution, the angle producing the largest gain of the H-plane pattern in the farthest lane was used, enabling the optimal uniform power response to be obtained easily. The trigonometric relationship of Fig. 6.6 was also employed to derive the angle ψ of maximum gain at a particular distance, which is given by

$$\psi = \tan^{-1}(\frac{D}{h})$$

The rotation angle is given by

$$\beta = \psi - 56°$$
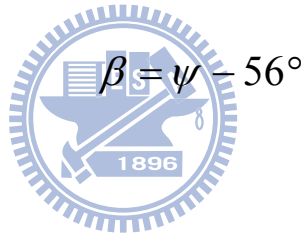
then

$$\beta = \tan^{-1}(\frac{D}{h}) - 56° \tag{6-6}$$

Table 6.1 lists estimated optimal angles of mechanical rotation for between 10m and 60m, as determined from (6-6). If the sensor height is fixed at 3m, then Table 6.1 yields the distance of the farthest lane that corresponds to the angle of mechanical rotation. Table 6.1 covers distances of the farthest lane from 20 m to 60 m, corresponding to angles of mechanical rotation of between −47° and −54°. These angles are also associated with the best uniform spatial power distribution. Therefore, uniform SNR measurement can easily be achieved by aiming the main beam at the farthest lane

Table 6.1 Farthest lanes corresponding to given angles of rotation

D	10m	15m	20m	30m	40m	50m	60m
β	-39°	-44°	-47°	-50°	-52°	-53°	-54°

The general definition of SNR was measured on the receiving port and calibrated the gain of LNA, mixer and IF AMP. The SNR equation (6-7) was formed by combining (6-2) and (6-5). The SNR parameters are defined in the preceding paragraph

$$SNR = \frac{P_{TX}G_T(\theta+\beta)G_R(\theta+\beta)\lambda^2\sigma}{(4\pi)^3(h\cdot\csc\theta)^4kTB_dN_F} \tag{6-7}$$

The theoretical SNR was converted to dB form by subtracting the power of the receiving signal from the total noise power.

$$SNR\ (dB) = 0\ dBm + dB(G_T(\theta+\beta)) + dB(G_R(\theta+\beta)) - 30\ dB + 0\ dB - 33\ dB - 40\ log\ (3\cdot\csc\theta) + 128\ dB \tag{6-8}$$

The SNR of the proposed sensor system was experimentally characterized by performing extensive field tests. The results were then compared with the theoretical data using (6-8). Figure 6.8 illustrates composite plots of SNR versus distance to the comparisons angles (β) of mechanical rotation of $-35°$ and $-50°$. The two groups of curves indicate excellent agreement for distances of 10–30m. Near-field interference was prevalent at less than 10m, but was canceled by the envelope of the proposed H-plane pattern and the isolation of the presented CMOS chip. At angles of $-35°$ or $-50°$, the SNR of the CMOS-based FMCW sensor system increased from 25dB to 42dB as the distance increased from 5m to 30m. The unique characteristic results mainly from the radiation pattern of the

leaky-mode antenna arrays. The H-plane radiation pattern from 5.7° to 31° covered the multiple-lanes distances of 5–30m, based on (6-4). The antenna gain of the FMCW sensor system was inversely proportional to the square of the distance. The unique radiation pattern compensated for the signal degradation, as predicted by (6-3). At an angle of −50° , which was the angle of maximum power when the H-plane was aimed at the farthest lane, the power of the reflected signals was maintained the most constant for range measurement, yielding a nearly constant value of SNR when using the proposed FMCW sensor design. The SNR measurement result shows that the structure of the presented FMCW sensor has a good STC function for measuring the range of TMS.
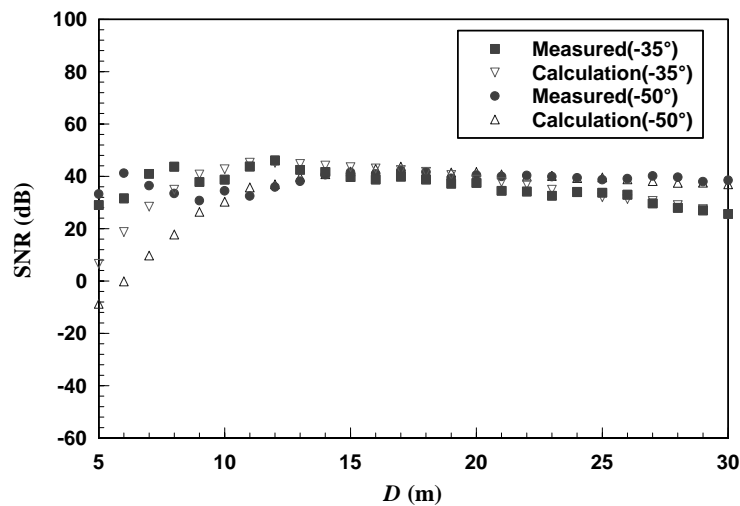
Fig. 6.8 Signal-to-noise ratio (SNR) of CMOS-based FMCW sensor in Fig. 6.6.

6.2.2 Range Measurements

In general, the road width of a freeway including the shoulder of the road is less than 30 meters, and then the maximum range of measurement is specified 30 meters. The frequency of the triangular waveform is 1000Hz to adapt the round-trip time of signal propagation and the sampling rate of DSP chip. Hence the frequency resolution is obtained 2 KHz. In other words, for each 1 meter of the range resolution is corresponding to each 2 KHz of the frequency resolution. The range of 30 meters is corresponding to the beat frequency of 60 KHz. Therefore, the bandwidth of the IF filter can set to more than 60 KHz and may extend to 100 KHz for the environmental detection.

The sensor located in the roadside was vertical to the multiple-lanes, since a vertical direction to the target results in a zero-frequency Doppler shift, whether the vehicle is stationary or moving. Range measurements were performed to detect vehicle occupancy in the field tests using the setup in Fig. 6.6. The output signal of the IF amplifier was obtained by the commercial digital signal processor TMS320C6701. The following digital processor parameters were set when performing the signal processes. The pulse-repeated-frequency (*PRF*) was set to 500.0Hz, and the period of the triangular wave (t_m) was 1ms. According to the curve in Fig. 3.8 (b), the amplitude of the triangular wave required to control the CMOS FMCW transceiver with a modulation bandwidth (*BW*) of 150.0MHz was 42.5mV. Since the maximum distance between the vehicle and sensor was 30.0m according to Fig. 6.6, the maximum round trip time (τ) was 0.2μs. Therefore, with reference to (2-3) and (2-7) in chapter 2, the maximum beat frequency (f_b) and range resolution (R_0) were 60.0KHz and 1.0 m, respectively. A digital signal processor was adopted to obtain the distance

between the vehicle and the sensor according to (2-4), after obtaining f_b from the digitized IF signal. Figure 6.9 plots both the measured and the theoretical beat frequency. The measured beat frequency is a function of the distance calculated by the digital processor: the gradient of the curve was nearly a constant. Since the sensor height was 3m, the maximum linear detection range was 8m, as calculated by trigonometric identity, and the maximum linearity was 4%, as calculated from Fig. 6.9. Therefore, the linearity of range measurement partially corresponded to the linearity of VCO. These measurements confirm that the operation of the proposed CMOS-based FMCW sensor, including the CMOS transceiver and leaky-mode antenna arrays, follows the principles described in chapter 2. An X-band FMCW sensor can thus be feasibly realized by CMOS technology for TMS applications.
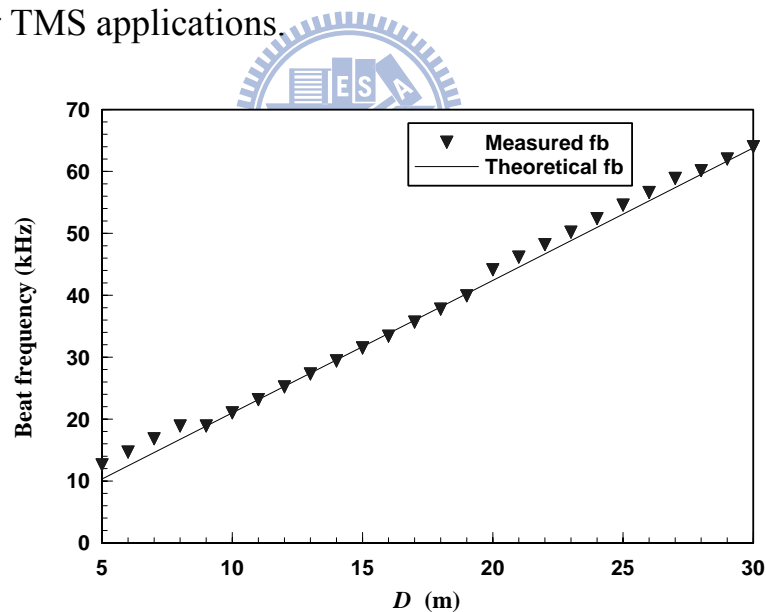
Fig. 6.9 Measured and theoretical beat frequency vs. distance calculated using digital processor.

In theory, the bandwidth of 100 KHz is still far less than the maximum signal *BW* of 500MHz, then the linearity of the beat frequency should be 3%. But the nonlinearity effects occurred in the region of less than 8 meters are

caused by the system setup. Figure 6.10 also demonstrates the beat frequencies (f_b) varied with the widths (D) of the freeway and the real distance (R) from the sensor to each lane is denoted by dashed-line. However, nonlinear effects at less than 8m were caused by the system setup. In particular, at less than 3m, the nonlinear characteristic cannot be compensated by data processing. Fortunately, a range of less than 3m includes only the shoulder of the road. In general, the width of each lane of the freeway is about 3 meters and the transverse width of most of the vehicles is less than 2.3 meters. The two cars can't occupy in the same lane at the same segment and a vehicle can't always run on white zig lines of road dividers by the rules of the road. In case of the above assumption, the range resolution of 1 meter is enough to discriminate two cars in neighboring lanes.
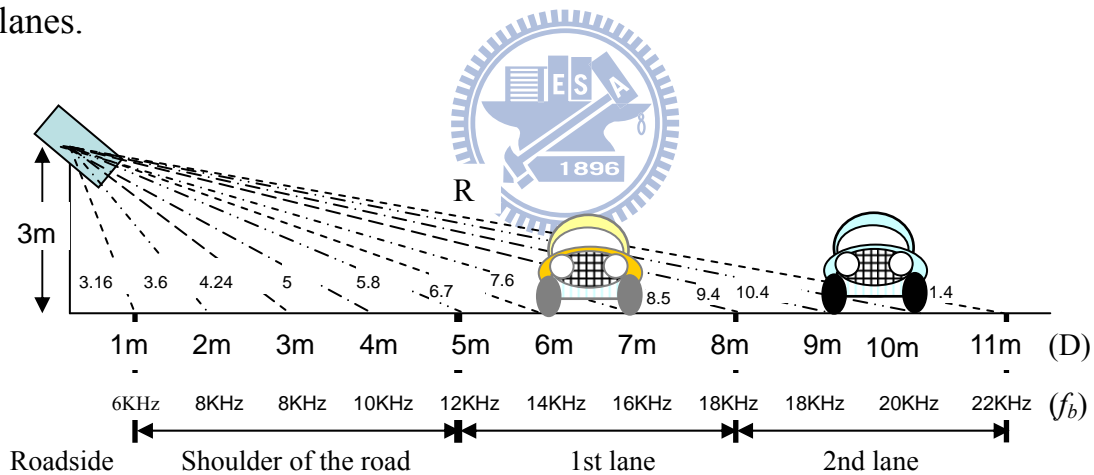
Fig. 6.10 System setup of FMCW sensor of the range is less than 11 meters.

The sensor was used to construct a range measurement of TMS, the $\csc^2\theta$ pattern is the key factor that supported a near uniform SNR for measures region. The near uniform SNR is described that the difference of maximum and minimum echo power was less than 30 dB in the measured region. Since the vary vehicles drive on the different lanes of the highway that include trucks, bus, cars, and so on. The sensor is applied to TMS include the traffic flow analysis

and the vehicle classification. The range measurement of this sensor is used to analyze the traffic flow from the nearest lane to the farthest lane and the spatial power of range measurement is frequency domain that has no relationship with the amplitude of the echo signal. But the sensor is also applied to vehicle classification that requires a near uniform echo power at the measured region. For example it can distinguish trucks from cars in same lane with the intensity of echo power. Another focal point is improvement of the dynamic range from IF circuit to digital signal processor unit. In one word, the $csc^2\theta$ pattern of the leaky-wave antenna just provides a near uniform SNR and compensates some loss of spatial power of $1/R^4$ distribution.
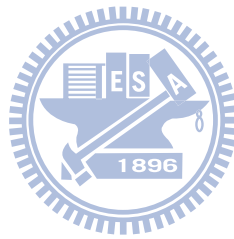
CHAPTER 7

Conclusion

The study presents a CMOS-based FMCW sensor system for the vehicle detection in TMS. The sensor comprises a CMOS transceiver, two planar leaky-mode antenna arrays and the signal-processing unit. The transceiver is fabricated by standard 0.18μm CMOS 1P6M technology with a size of 1.68 mm×1.6 mm.

The electrical performance of both individual blocks and transceiver is experimentally characterized and reported, revealing two significant issues in FMCW sensor design. First, the on-chip VCO achieves a linearity of 3.0% with the modulated bandwidth against the triangular wave amplitude for a frequency modulation of 500MHz at 10.5GHz. The linearity dominates the accuracy of the range measurements in vehicle detections. Second, the on-chip isolation between the transmitting and receiving paths is 55dB. The isolation directly influences the SNR of the sensor system. Additionally, the antenna array in the sensor system operates in leaky mode. Base on measurement results, the antenna gain and the isolation between two adjacent leaky-mode antenna arrays with a spacing of 5.0mm are 18.0dB and 42dB, respectively, at 10.5 GHz. The reported performance measurements indicate that the proposed system has a better isolation than a sensor system with a single antenna and a circulator.

For multiple lanes measurement of TMS, the function of the roadside unit is similar to the csc^2 type radar, which has been nearly uniform spatial echoes power between detection ranges. The csc^2 type antenna pattern generally applies to surveillance radar of military application. Such antennas are always

large-scale, high-power and long-distance, and are designed with reflected antenna technology. However, the antenna arrays presented to herein adopt short-range detection and planar antenna. The special pattern of antenna arrays is specific to leaky mode, and conditionally compensates for the space loss of $1/R^4$. In other words, the function of the presented antenna pattern is similar to the sensitivity time control (STC) of the IF filter, which provides the spatially uniform SNR of range measurement.

The future works of the thesis will use the CMOS integrated circuit technology to miniaturize and integrate all the circuits of all parts, such as radio frequency circuits, analog circuits and digital circuit and so on. The miniaturized radar system integrates with RFIC, AIC, and DIC into a system on chip (SOC).

Reference

1   **From Wikipedia, the free encyclopedia,** "History of Radar." [Online]. Available: http://en.wikipedia.org/wiki/Radar

2   Charles E. Cook and Marvin Bernfeld, "Radar Signals - An Introduction to Theory and Application," Aretech House, Inc., Norwood, MA, 1993.

3   H. J. Siweris, A. Werthof, H. Tischer, U. Schaper, A. Schäfer, L. Verweyen, T. Grave, G. Böck, M. Sclechtweg, and W. Kellner, "Low-Cost GaAs pHEMT MMIC's for Millimeter-Wave Sensor Applications," *IEEE Trans. on Microwave Theory and Techniques*, vol. 46, no. 12, pp. 2560-2567, Dec. 1998.

4   D. C. W. Lo, K. W. Chang, R. Lin, E. W. Lin, H. Wang, M. Biedenbender, G. S. Dow, and B. R. Allen, "A Single-chip W-band Transceiver with Front-end Switching Receiver for FMCW Radar Applications," in *IEEE Microwave and Millimeter-Wave Monolithic Circuits Symposium*, Orlando, FL, May 1995, pp. 225-228.

5   W. H. Haydl, M. Neumann, L. Verweyen, A. Bangert, S. Kuddazus, M. Schlectweg, A. Hülsmann, A. Tessmann, W. Reinert, and T. Krems, "Single-Chip Coplanar 94-GHz FMCW Radar Sensors", *IEEE Microwave and Guided wave Letters*, vol. 9, no. 2, pp. 73-75, Feb. 1999.

6   D. Chouvaev, A. Dalerå, and U. Stein, "Application of a Substrate-Lens Antenna Concept and SiGe Component Development for Cost-Efficient Automotive Radar," in *European Radar Conference 2004. EuRAD. First European*, Manchester, UK, Oct. 2004, pp. 81-54.

7   Y. Watanabe and N. Okubo, "HEMT Millimeter-wave Monolithic IC Technology for 76-GHz Automotive Radar," *FUJITSU Sci. Tech*. J., vol. 34, no. 2, pp.153-161, Dec. 1998.

8   M. Camiade, D. Domnesque, Z. Quarch, and A. Sion, "Fully MMIC-Based Front End for FMCW Automotive Radar at 77GHz," *European Microwave Conference. Week, GaAs 2000 Proceedings*, Paris, France, Oct. 2000, pp.1-4.

9   S. T. Nicolson, K A. Tang, K. H.K. Yau, P. Chevalier, B. Sautreuil, and S. P. Voinigescu, "A Low-Voltage 77-GHz Automotive Radar Chipset," in *IEEE MTT-S Int. Microwave Symp. Dig.,* Honolulu, Hawaii, Jun. 2007*,* pp.487-490.

10 R. Reuter, H. Li, I. To, Y. Yin, A. Ghazinour, D. Jahn, D. Morgan, J. Feige, P. Welch, S. Braithwaite, B. Knappenberger, D. Scheitlin, J. John, M. Huang, P. Wennekers, M. Tutt, C. Trigas, and J. Kirchgessner, "Fully Integrated SiGe-BiCMOS Receiver(RX) and Transmitter(TX) Chips for 76.5 GHz FMCW Automotive Radar Systems Including

Demonstrator Board Design, " in *IEEE MTT-S Int. Microwave Symp. Dig.,* Honolulu, Hawaii, Jun. 2007*, pp.*1307-1310.

11 G. S. Woods, D. L. Maskell, and M. V. Mahoney, "A High Accuracy Microwave Ranging System for Industrial Applications," *IEEE Trans. on Instrumentation and Measurement*, vol. 42, no. 4, pp. 812-815, Aug. 1993.

12 D. Brumbi, "Low Power FMCW Radar System for Level Gaging," in *IEEE MTT-S Int. Microwave Symp. Dig.*, Boston, MA, Jun. 2000, pp. 1559-1562.

13 J C. Clifton, A W Dearn, P. R. Bestwick, L. M. Devlin, and M. W. Geen, *"GaAs* Power MMIC for X-Band Radar Applications," in *Modelling, Design and Application of MMIC's*, *IEE Colloquium on*, London, UK, Jun. 1994, pp. 12/1-12/6.

14 Wavetronix SmartSensor TM Model 105, Wavetronix LLC, UT84042 USA. [Online]. Available: http:// www.wavetronix.com

15 T. N. Trinh, E. Benko, and W. S. Wong, "KA-Band Microstrip Integrated Circuit FMCW Transceiver," in *IEEE MTT-S Int. Microwave Symp. Dig.*, Baltimore, MD, Jun. 1986, pp. 639-642.

16 L. Reynolds and Y. Ayasli, "Single Chip FMCW Radar for Target Velocity and Range Sensing Applications," in *GaAs IC Symposium, 1989. Technical Digest 1989, 11th Annual,* San Diego, CA, Oct. 1989, pp**.** 243-246.

17 A. Tessmann, S. Kudszus, T. Feltgen, M. Riessle, C. Sklarczyk, and W. H. Haydl, "Compact Single-Chip W-Band FMCW Radar Modules for Commercial High-Resolution Sensor Applications," *IEEE Trans. on Microwave Theory and Techniques*, vol. 50, no. 12, pp.   2995-3001, Dec. 2002.

18 A. Tessmann, S. Kudszus, T. Feltgen, M. Riessle, C. Sklarczyk, W. H. Haydl, "A 94 GHz Single-Chip FMCW Radar Module for Commercial Sensor Applications," in *IEEE MTT-S Int. Microwave Symp. Dig.*, Seattle, WA, Jun. 2002, pp. 1851-1854.

19 K. Sasaki, J. Utsu, K. Matsugatani, K. Hoshino, T. Taguchi, and Y. Ueno, "InP MMICs FOR V-BAND FMCW RADAR," in *IEEE MTT-S Int. Microwave Symp. Dig.*, Denver, CO, Jun. 1997, pp. 937-940.

20 D. C. Chang and Y. C. Cheng, "Development of Eight Meters Inverse Cosecant Square Reflector Antenna," in *IEEE Antennas and Propagation Society International Symp.,* vol. 2, Orlando, FL, July 1999, pp.1160 – 1163.

21 Terma A/S SCANTER 2001 Radar System, Terma A/S Hovmarken 4 DK - 8520 Lystrup Denmark. [Online]. Available: http://www.terma.com/radar.

22 AN/GSS-7 Search Radar, Radio Research Instrument Co., Inc. 584 N. Main Street Waterbury, CT. 06704-3506 USA. [Online]. Available: http://www.radiores.com/

23 T. L. Foreman, "A Model to Quantify the Effects of Sensitivity Time Control on Radar-to-radar Interference," *IEEE Trans. on Electromagnetic Compatibility*, vol. 37, no. 2, pp. 299 – 301, May 1995.

24 T. Moriyama, H. Kasahara, Y. Yamaguchi, and H. Yamada, "Advanced Polarimetric Subsurface FM-CW Radar," *IEEE Transactions on Geoscience and Remote Sensing*, vol. 36, no. 3, pp.725 – 731, May 1998.

25 C. E. Livingstone, A. L. Gray, R. K. Hawkins, and R. B. Olsen, "CCRS C/X Airborne Synthetic Aperture Radar: An R and D Tool for the ERS-1 Time Frame," *in Proc. 1988 IEEE National Radar Conference*, Ann Arbor, MI, Apr. 1988, pp.15 – 21.

26 A. M. Madni, P. T. McDonald, R. K. Hansen, and L. A. Wan, "High Dynamic Range Airborne Tracking and Fire Control Radar Subsystem," *IEEE Trans. on Microwave Theory and Techniques*, vol. 37, no. 12, pp.1942 – 1948, Dec. 1989.

27 C. S. Miller, "Signal Processor Retrofit for Air Search Radar," *in Proc. 1992 IEEE Aerospace Applications Conference, Dig.*, Snowmass, CO, Feb. 1992, pp.77 – 85.

28 S. A. Hovanessian, "Radar Detection & Tracking Systems," Aretech House, Inc., Dedham, MA, 1982.

29 J. A. Scheer and J. L. Kurtz, "Coherent Radar Performance Estimation," Artech House, 1993, Chapter 12, pp.289-313.

30 **EESA Earthnet Online, European Space Agency, "The Radar Equation."** [Online]. Available: http://earth.esa.int/applications/data_util/SARDOCS/spaceborne

31 C. K. C. Tzuang, C. C. Chen, and W. Y. Chien, "LC-free CMOS Oscillator Employing Two-dimensional Transmission Line," *in Proc. 2003 IEEE Int. Frequency Control Symp. and PDA Exhibition and the 17th European Frequency and Time Forum,* pp. 487-489, May 2003.

32 C. C. Chen and C. K, C. Tzuang, "Synthetic Quasi-TEM Meandered Transmission Lines for Compacted Microwave Integrated Circuits," *IEEE Trans. on Microwave Theory and Techniques*, vol 52, no 6, pp. 1637-1647, June 2004.

33 M. J. Chiang, H. S. Wu, and C. K. C. Tzuang, "Design of CMOS Spiral Inductors for Effective Broadband Shielding," *Proc. 36th European Microwave Conference Digest,* Manchester, UK, Sept. 2006, pp. 48-51.

34 C. K. C. Tzuang, C. H. Chang, H. S. Wu, S. Wang, S. X. Lee, C. C. Chen, C. Y. Hsu, K. H. Tsai, and J. Chen, "An X-Band CMOS Multifunction-Chip FMCW Radar," *Proc. of the 2006 IEEE MTT-S Int. Microwave Symp. Dig.,* San Francisco, CA, Jun. 2006, pp. 2011~2014.

35 Ali F., Podell, A., "A Wide-Band Push-Pull GaAs Monolithic Active Isolator," *IEEE Microwave and Guided Wave Lett.,* vol. 1, no. 2, pp. 26-27, 1991.

36 S. Wang, H. S. Wu, C. H. Chang, and C. K. C. Tzuang, "Modeling and Suppressing Substrate Coupling of RF CMOS FMCW Sensor Incorporating Synthetic Quasi-TEM Transmission Lines," in *IEEE MTT-S Int. Microwave Symp. Dig.,* Honolulu, Hawaii, Jun. 2007, pp.1939-1942.

37 K. Lin, Y. E. Wang, C. K. Pao, Y. C. Shih, "A Ka-Band FMCW Radar Front-End With Adaptive Leakage Cancellation," *IEEE Trans. on Microwave Theory and Techniques*, vol. 54, no. 12, pp. 4041-4048, Dec. 2006.

38 A. H and T. H. Lee, "The design of low noise oscillators," Kluwer Academic, 1999.

39 S. Wang, H. S. Wu, and C. K. C. Tzuang, "An X-band Transmission Line Based CMOS VCO with FM Modulation", in *2007 Topical Meeting on Silicon Monolithic Integrated Circuits in RF Systems (SiRF07),* Long Beach, CA,.Jan. 2007, pp.139-141.

40 B. Gilbert, "A Highly Linear Variant of the Gilbert Mixer Using a Bisymmetric Class-AB Input Stage," *IEEE Journal of Solid-state Circuits*, vol. 32, no. 9, pp. 1412-1423, Sept. 1997.

41 H. Cooper and H. McComas, "Synthesis of $csc^2\theta$ type antenna patterns using two-dimensional surface wave arrays," in *IRE International Convention Record,* vol. 8, Part 1, Mar. 1960 pp.24 – 34.

42 I. Ohtera, "On a Forming of Cosecant Square Beam Using a Curved Leakywave Structure," *IEEE Trans. on Antennas and Propagation,* vol. 49, no. 6, pp.1004 – 1006, June 2001.

43 C. N. Hu and C. K. C. Tzuang, "Analysis and Design of Large Leaky-mode Array Employing the Coupled-mode Approach," *IEEE Trans. on Microwave Theory and Techniques*, vol. 49, no. 4, pp. 629-636, Apr. 2001.

44 K. F. S. Huang and C. K. C. Tzuang, "Characteristics and Design of Broadside-Coupled Transmission Line at a Higher Order Leaky Mode," *IEEE Trans. on Microwave Theory and Techniques*, vol. 51, no. 2, pp. 440 – 447, Feb. 2003.

45 G. J. Chou and C. K. C. Tzuang, "An Integrated Quasi-Planar Leaky-Wave Antenna," *IEEE Trans. on Antennas and Propagation,* vol. 44, no. 8, pp.1078 – 1085, Aug. 1996.

46 Y. D. Lin, J. W. Sheen, and C. K. C. Tzuang, "Analysis and Design of Feeding Structures for Microstrip Leaky-Wave Antenna," *IEEE Trans. on Microwave Theory and Techniques*, vol. 44, no. 9, pp. 1540 – 1547, Sept. 1996.

47 C. C. Lin and C. K. C. Tzuang, "A Dual-Beam Micro-CPW Leaky-Mode Antenna," *IEEE Trans. on Antennas and Propagation,* vol. 48, no. 2, pp. 310 – 316, Feb. 2000.

48 C. N. Hu and C. K. C. Tzuang, "Injection-Locked Coupled Microstrip Leaky-Mode Antenna Array**,**" IEE Proceedings -Microwaves, Antennas and Propagation, vol. 147, no. 5, pp.364 – 368, Oct. 2000.

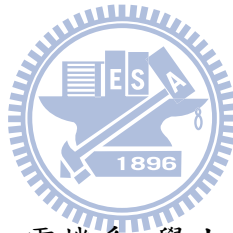49 W. L. Stutzman and G. A. Thiele, "Antenna Theory and Design," 2nd Edition, John Wiley & Sons, Inc.1998.

博士候選人資料

姓　名：張繼禾

性　別：男

出生年月日 ： 民國 52 年 6 月 15 日

籍　貫： 四川省自貢市

學　歷： 中正理工學院 電機系 學士　　　(72.07～76.07)

　　　　 中山大學 電機研究所 碩士　　　(78.09～80.06)

經　歷： 陸軍第十軍團七四通信兵群排長　(76.08～78.08)

　　　　 陸軍第一〇九機械化師通信排長　(80.07～81.03)

　　　　 陸軍通信基地勤務處通材修護官　(81.04～82.01)

　　　　 中山科學研究院 副工程師、工程師(82.01～今　　)

論文題目 ：調頻連續波感測器射頻前端設計與系統整合驗證